

ABSTRACT

Title of Document:

**ELECTROCHEMICAL OXIDATION
KINETICS OF HYDROGEN AND HIGHER
HYDROCARBON FUELS ON SOLID
OXIDE FUEL CELLS.**

Oktay Demircan, Ph.D., 2007

Dissertation Directed By:

**Professor Bryan W. Eichhorn, Department of
Chemistry and Biochemistry**

Solid oxide fuel cells (SOFCs) are promising electrochemical energy converting devices due to their ability to use not only hydrogen but also hydrocarbons as a fuel. Although conventional SOFCs with Ni/YSZ anodes and hydrocarbon fuels form carbon deposits that inhibit SOFC performance, an enhancement in performance is observed for the Cu/CeO₂/YSZ anode with carbon deposits and H₂ fuel. Structural and compositional analyses of these carbon deposits show that graphitic carbon forms on the Cu/CeO₂/YSZ. The reason of the 2 to 3 fold enhancement in performance is due to increase in anode conductivity by graphitic carbon deposits.

An important problem for fuel oxidation kinetics on SOFC anodes is determining the rate limiting step(s) for fuel oxidation. To assess the effects of YSZ surface chemistry on oxidation processes, porous and dense Au anodes on YSZ electrolytes were prepared to study H₂ oxidation. Linear Sweep Voltammetry (LSV) and Electrochemical Impedance Spectroscopy (EIS) were used to identify critical processes in the Au/YSZ anodes as a function of Au geometry. The results show that the surface diffusion on the SOFC anodes and electrolytes is believed most likely to be the rate limiting step.

To address the contribution of reduced YSZ on SOFC anode performance, porous Au anodes with different geometrical porous YSZ layers were fabricated. Studies of porous YSZ layers on Au anodes demonstrate that these layers block active sites on Au anodes for dissociative adsorption of hydrogen but help charge transfer reaction of adsorbed species on anode. Other than regular hydrogen as a fuel, isotopically-labeled D_2 fuel were used to differentiate effects of both gas phase and surface diffusion on Au anode performance. An observed ~25 % decrease in current and power densities with D_2 relative to H_2 is attributed to lower surface diffusion of adsorbed D_2 fuel species relative to H_2 fuel species.

Finally, modeling studies for these systems are used to understand more fully the mechanisms of H_2 oxidation on SOFC anodes. The interpretations of experimental results are confirmed by using the model that manipulates the effect of various fuel partial pressures on the diffusion parameters of anode surface species. The model developed is able to describe qualitatively the isotope effect on the gas and surface diffusion coefficients by the mass affect. The implementation of the surface diffusion parameters of the water species into this model is critical to manipulate the effect of the fuel partial pressure values on diffusion processes.

**ELECTROCHEMICAL OXIDATION KINETICS OF HYDROGEN AND
HIGHER HYDROCARBON FUELS ON SOLID OXIDE FUEL CELLS.**

By

Oktay Demircan

Dissertation submitted to the Faculty of the Graduate School of the
University of Maryland, College Park, in partial fulfillment
of the requirements for the degree of
Doctor of Philosophy
2007

Advisory Committee:
Professor Bryan W. Eichhorn, Chair
Professor Jeffery Davis
Associate Professor Gregory S. Jackson
Associate Professor Robert A. Walker
Assistant Professor Andrei Vedernikov

© Copyright by
Oktay Demircan
2007

Dedicated to my mother, Gülnaziye Cebeci, and to my family,
(Annem, Gülnaziye Cebeci, ve aileme ithaf edilir,)

Acknowledgements

This part of the thesis is one of the hardest to write, I have to admit. None of the words that I know can full express my gratitude to a number of people, who helped and supported me during my PhD period.

The study was conducted under the excellent supervision of Professor Bryan W. Eichhorn whom I gratefully acknowledge for his enthusiasm and many hours of helpful discussion throughout the progress of my thesis. In particular, I wish to thank him for the opportunity to present my results on international conferences.

Professor Greg S. Jackson and Professor Robert A. Walker are gratefully acknowledged for being co-advisors of the thesis.

I would also like to thank Professor Jeffery Davis and Andrei Vedernikov for being the committee members of my PhD thesis.

I wish to thank to Tim Mangel for his help on SEM images and Bindhu Varughese for her guidance and patience in XPS studies.

I am deep in debt to my colleagues whom I had a chance to work with in the Eichhorn's Group: Dr. Emren Nalbant-Esentürk, Dr. Chad Alan Stoltz, Dr. Melanie Moses, Dr. Shenghu Zhou, Selim Alayoğlu, Sanem F. Koçak, and Andre Dennis for their endless support in my PhD period.

Very special thanks go to my colleagues in Solid Oxide Fuel Cell group at UMD: Dr. Mary Sukesini, Dr. Michael Brandon Pomfret, Bahman Habibzadeh, Steven DeCaluwe, Ben Becker, Dr. Seyed Reihani, Anthony Dylla, Young Kyong Jo, Bryan Eigenbrodt, and Paul Jawlik for their valuable discussions on every aspect of SOFC.

I am very grateful to my friends: Dr. Albert Epshteyn, Dr. Okan Esentürk, and Süleyman Z. Can for their endless patience and very valuable discussions.

I would also thank to people at the Department of Chemistry, whom I worked several years in enthusiasm, for their smile in every morning.

Finally, my highest appreciation is addressed to my family: my mother, Gülnaziye Cebeci, my sister, Perihan Demircan, and my brother, Hasan Demircan, who believed in me, who shared my sorrow, and who motivated me in all circumstances.

Table of Contents

Acknowledgements.....	iii
Table of Contents.....	v
List of Tables	viii
List of Figures	ix
Chapter 1:.....	1
General Introduction	1
1.1. Overview:.....	1
1.2. Solid Oxide Fuel Cell (SOFC):.....	4
1.2.1. Principles of SOFC operation:	5
1.2.2. Electrolytes:	6
1.2.3. Cathodes:.....	7
1.2.4. Anodes:	8
1.2.5. Planar SOFC cell designs:	9
1.2.6. Performance limiting processes:	12
1.3. Fields of Research:.....	19
1.4. Scope of the thesis:	26
Chapter 2:.....	28
Formation of Carbon Deposits from Hydrocarbon Fuels in Solid Oxide Fuel Cells..	28
2.1. Introduction.....	28
2.2. Experimental Section	31
2.2.1. Preparation of Cathode:	32
2.2.2. Preparation of Anodes:	33
2.2.3. Preparation of Cell Assembly:	34
2.2.4. SOFC Operation Conditions:	34
2.2.5. Characterization Techniques:.....	34
2.3. Results and Discussions	36
2.3.1. Performance of SOFC anodes:.....	36
2.3.2 SEM images of SOFC anode surfaces:	39
2.3.3 XRD analysis of SOFC anode surfaces:	41
2.3.4. Raman studies of SOFC anode surfaces:	43
2.3.5. XPS studies of SOFC anode surfaces:	46
2.4. Conclusions.....	50
Chapter 3:.....	53
Analysis of different Au anodes with different geometry and different Porous YSZ layers in SOFC assembly	53
3.1. Introduction.....	53
3.2. Experimental Section	58
3.2.1 Preparation of porous Au paste anodes:.....	58
3.2.2 Preparation of Dense Au Film anodes:	59
3.2.3 Preparation of Porous YSZ layer:	59
3.2.4 Preparation of Porous Au anodes with α -Al ₂ O ₃ Blocking:	60
3.2.5. Characterization Techniques:.....	60

3.3. Results.....	61
3.3.1 Porous Au anodes with different Au/YSZ interface area:	61
3.3.2 Dense Au Film patterned Anodes:.....	65
3.3.3 Porous Au Anodes with YSZ over layers:.....	70
3.3.4 Porous Au Anodes with an isolated porous YSZ patch:.....	73
3.3.5 Porous Au anodes with different α -Al ₂ O ₃ sub-surface blocking between porous Au and YSZ:	76
3.4. Discussions	79
3.4.1 Porous Au anodes with different Au/YSZ interface area:	79
3.4.2 Dense Au Film patterned Anodes:.....	80
3.4.3 Porous Au Anodes with YSZ over layers:.....	81
3.4.4 Porous Au Anodes with an isolated porous YSZ patch:.....	82
3.4.5 Porous Au anodes with different α -Al ₂ O ₃ sub-surface blocking between porous Au and YSZ:	83
3.5. Conclusions.....	85
Chapter 4:.....	87
Isotopically labeled D ₂ fuel comparison with H ₂ on Au anode SOFCs by experimental and computational methods	87
4.1. Introduction.....	87
4.2. Experimental Section.....	91
4.2.1 Preparation of porous Au anodes:.....	92
4.2.2 Arrangement of partial pressure of fuel and humidifying agent content:.....	92
4.2.3 Characterization Techniques:.....	93
4.3. Results.....	94
4.3.1 The effect of dry H ₂ partial pressures on porous Au anodes with different thicknesses in SOFC:	95
4.3.2 The effect of water on Au anodes with varying partial pressures of H ₂ :.....	103
4.3.3 The comparison of isotopically labeled D ₂ fuels with H ₂ fuel on porous Au anodes with different thicknesses:	108
4.3.4 Modeling studies of four different thicknesses porous Au anodes with various fuel partial pressures of H ₂ :.....	112
4.4. Discussions	117
4.4.1 The effect of dry H ₂ partial pressures on porous Au anodes with different thicknesses in SOFC:	117
4.4.2 The effect of water on Au anodes with varying partial pressures of H ₂ :.....	121
4.4.3 The comparison of isotopically labeled D ₂ fuels with H ₂ fuel on porous Au anodes with different thicknesses:	124
4.4.4 Modeling studies of four different thicknesses porous Au anodes with various fuel partial pressures of H ₂ :.....	130
4.5. Conclusions.....	131
Chapter 5:.....	135
Conclusions.....	135
5.1. Introduction.....	135
5.2. Evaluation of the results:	135
5.2. Future works and recommendations:	138
Appendix.....	139

References.....	142
-----------------	-----

List of Tables

Table 1.1: Different types of fuel cells.....	2
Table 2.1: Raman Data of SOFC anode surfaces.....	46
Table 2.2: C and O atomic percentages from XPS Spectra.....	49
Table 3.1: EIS data for porous Au anodes with different interface areas.....	65
Table 3.2: EIS data for Au film anodes with different interface areas.....	70
Table 3.3: EIS data for porous Au anodes with porous YSZ over layers.....	72
Table 3.4: EIS data for porous Au anodes, one with isolated porous YSZ patch ..	75
Table 3.5: EIS data for porous Au anodes, with α -Al ₂ O ₃ blocking.....	79
Table 4.1: Maximum current densities of porous Au anodes with dry H ₂	97
Table 4.2: Summary of EIS spectra fitting parameters at high current region for various thickness porous Au anodes with different dry H ₂ fuel fractions.....	100
Table 4.3: Maximum current densities of porous Au anodes with wet H ₂	105
Table 4.4: Summary of EIS spectra fitting parameters at high current region for Au anodes with different wet H ₂ fuel fractions.....	106
Table 4.5: Maximum current densities of porous Au anodes with H ₂ , HD, and D ₂	110
Table 4.6: Summary of the equivalent circuit fitting parameters of EIS spectra at 1V overpotential for Au anodes with 70 sccm dry and wet H ₂ and D ₂ fuels.....	111
Table 4.7 Summary of modeling parameters used in this study.	115

List of Figures

Figure 1.1 Schematic representation of SOFC assembly operation (the anode and cathode sides are physically separated from each other by a dense electrolyte and high temperature ceramic sealing).....	5
Figure 1.2 Planar cell designs a) cathode supported cell, b) electrolyte supported cell, and c) porous anode supported cell, drawings not to scale.	10
Figure 1.3 Schematic graph of the voltage drop of SOFC as a function of withdrawn current density, a) low current regime, b) medium current regime, and c) high current regime.....	12
Figure 1.4 Schematic representation of EIS Nyquist plot.....	17
Figure 1.5 a) Oxygen reduction pathways on conventional LSM-YSZ cathodes, b) Experimental setup for alumina blocking experiments from Fleig <i>et al.</i> [92].....	22
Figure 1.6 Current collector experiments designs from Jiang on the SOFC cathodes, a) 0.032 mm ² current collector area, b) 0.012 mm ² current area of Pt and Ag from Jiang <i>et al.</i> [95].....	23
Figure 1.7 a) equivalent circuit for fitting EIS modeling studies, b) EIS simulations from modeling studies, from Zhu and Kee [105].....	26
Figure 2.1: Schematic representation of SOFC experimental set up.....	32
Figure 2.2: The SOFC power density vs. time plots for H ₂ -Butane-H ₂ cycle representing a) on Ni/YSZ b) 5 hours, and c) 100 hours of butane on Cu/CeO ₂ /YSZ anode systems (—CeO ₂ /YSZ, and --- Cu/CeO ₂ /YSZ anodes) Pictures of anode	

systems after SOFC operations are respectively shown next to the power density curves of anode systems..... 37

Figure 2.3: SEM images of a) Carbon deposits on Cu/CeO₂/YSZ anode surface b) enlargement of sample (a), c) the carbon film on YSZ disk.....40

Figure 2.4: SEM pictures of a) spherical carbon deposits b) the combination of spherical and filamentous carbon deposits on Ni/YSZ anode surfaces.....41

Figure 2.5: XRD Patterns of a) 325-mesh graphite, b) Ni/YSZ surface exposed to butane for 5 hours, c) carbon deposit isolated from CeO₂/YSZ anode surface exposed to butane for 5 hours, d) CeO₂/YSZ surface exposed to butane for 100 hours, e) CeO₂/YSZ surface exposed to butane for 5 hours (●: SiO₂ from ceramic paste, ■: YSZ, ◆: CeO₂) Inset: Graphite crystal structure.....42

Figure 2.6: Raman Spectra of a) 325-mesh graphite, b) Ni/YSZ anode (5 hours butane exposed), c) CeO₂/YSZ (5 hours butane exposed), d) CeO₂/YSZ (100 hours butane exposed), e) Cu/CeO₂/YSZ (100 hours butane exposed). Inset: Atomic motions of carbons and their symmetries in graphitic structure.....44

Figure 2.7: C1s region of X-ray photoelectron spectrum of a) 325-mesh graphite, b) typical SOFC anode surface.....47

Figure 3.1: Schematic representation of experimental setup of four different interface areas between Au and YSZ, a) Top view, b) Cross-section.....61

Figure 3.2: SEM images of porous Au anode, a) cross-section of electrode and electrolyte, b) top view of Porous Au anode.....61

Figure 3.3: Polarization curves of porous Au anodes with different interface area experiments on YSZ, a) raw performance, b) normalized performance with respect to

Au-YSZ interface area. (**Orange**: 1x8 mm, **Green**: 2x8 mm, **Blue**: 3x8 mm, **Magenta**: 4x8 mm, and **Black**: four electrodes wired together).....62

Figure 3.4: Normalization curves of Porous Au anode experiments, maximum power densities with respect to a) interface area between Porous Au and YSZ, b) triple phase boundary (TPB) length, i.e. perimeter of Porous Au anodes.....63

Figure 3.5: EIS (at OCV) curves of four different interface area experiments on YSZ, a) raw impedances, b) normalized with respect to interface area (inset: high frequency intercept as R_b) (**Orange**: 1x8 mm, **Green**: 2x8 mm, **Blue**: 3x8 mm, **Magenta**: 4x8 mm, and **Black**: all four electrodes wired together).....64

Figure 3.6: Schematic representation of experimental setup of four different interface areas between YSZ and Au film, a) Top view, b) Cross-section, c) Post Picture.....66

Figure 3.7: SEM images of Au film anode after 48 hours operation in SOFC, a) cross-section of delaminated Au film from YSZ surface b) top view of Au film on YSZ.....66

Figure 3.8: Polarization curves of Au film anodes with different interface area experiments on YSZ, a) raw performance, b) normalized performance with respect to Au-YSZ interface area. (**Orange**: 1x8 mm, **Green**: 2x8 mm, **Blue**: 3x8 mm, and **Black**: all three electrodes wired together)..... 67

Figure 3.9: Normalization curves of Au film anode experiments, maximum power densities with respect to a) interface area between Au film and YSZ, b) triple phase boundary (TPB) length, i.e. perimeter of Au film anodes..... 68

Figure 3.10: EIS curves (at OCV) of three Au film anodes with different interface areas (inset: high frequency intercept as R_b). (**Orange:** 1x8 mm, **Green:** 2x8 mm, **Blue:** 3x8 mm, and **Black:** all three electrodes wired together).....69

Figure 3.11: Schematic representation of experimental setup of two different interface areas between Au and YSZ and half covered with porous YSZ layer, a) Top view, b) Cross-section, c) Post Picture.....70

Figure 3.12: Polarization curves of porous Au anodes with and without porous YSZ over layers (normalized with respect to Au-YSZ interface area) (**Orange:** 2x8 mm, **Green:** 3x8 mm, **Blue:** 3x8 mm with porous YSZ layer, **Magenta:** 2x8 mm with porous YSZ layer).....71

Figure 3.13: EIS curves (at OCV) of four different porous Au anodes with and without porous YSZ over layers, normalized with respect to Au-YSZ interface area. (**Orange:** 2x8 mm, **Green:** 3x8 mm, **Blue:** 3x8 mm with porous YSZ over layer, **Magenta:** 2x8 mm with porous YSZ over layer).....72

Figure 3.14: Experimental setup of two different interface areas between Au and YSZ and one with porous YSZ layer patch, a) Schematic representation from top, b) Cross-section, c) Post-experiment Picture..... 73

Figure 3.15: Performance curves of porous Au anodes with different interface area and one with porous YSZ island on top (**Orange:** 2x8 mm Porous Au, **Green:** 3x8 mm Porous Au, **Magenta:** 3x8 mm Porous Au with 1x6 mm porous YSZ layer on top)..... 74

Figure 3.16: EIS curves (at OCV) of porous Au anodes with different interface area and one with porous YSZ island on top, normalized with respect to the interface

area between porous Au and YSZ electrolyte. (**Orange**: 2x8 mm Porous Au, **Green**: 3x8 mm Porous Au, **Magenta**: 3x8 mm Porous Au with 1x6 mm porous YSZ layer on top).....75

Figure 3.17: Experimental setup of four different interface areas between porous Au and YSZ by using α -Al₂O₃ blocking, a) Top view, b) Cross-section (right: 5x5mm Porous Au with 2x2mm α -Al₂O₃ blocking and left: 5x5mm Porous Au with 3x3mm α -Al₂O₃ blocking).....76

Figure 3.18: Polarization curves of Porous Au anodes with α -Al₂O₃ blocking a) Raw performance data, b) performance data normalized with respect to Au area, c) performance data normalized with respect to Au-YSZ contact area (α -Al₂O₃ blocking area subtracted) (**Orange**: 5x5mm porous Au, **Green**: 5x5mm porous Au with 1 mm² α -Al₂O₃, **Blue**: 5x5mm porous Au with 4 mm² α -Al₂O₃, **Magenta**: 5x5mm porous Au with 9 mm² α -Al₂O₃).....77

Figure 3.19: EIS curves (at OCV) of porous Au anodes with α -Al₂O₃ blocking, a) Raw data, b) normalized with respect to contact area between porous Au and YSZ electrolyte (inset: high frequency intercept as R_b) (**Orange**: 5x5mm Porous Au only, **Green**: 5x5mm Porous Au with 1x1mm α -Al₂O₃ blocking 3, **Blue**: 5x5mm Porous Au with 2x2mm α -Al₂O₃ blocking, **Magenta**: 5x5mm Porous Au with 3x3mm α -Al₂O₃ blocking).....78

Figure 4.1: Experimental setup of porous Au anodes with four different thicknesses a) Top view, b) Cross-section of the SOFC assembly.....94

Figure 4.2 SEM images of porous Au anodes with various thicknesses after 72 hours operation in SOFC.....95

Figure 4.3 Polarization curves (normalized with respect to Au-YSZ interface area, 16 mm^2 for all four electrodes) of four different thicknesses porous Au anodes with various fuel fractions of **dry** H_2 **Left:** whole range of polarization curves, **Right:** details in maximum current density regions (**Orange:** $30 \text{ }\mu\text{m}$, **Green:** $60 \text{ }\mu\text{m}$, **Blue:** $90 \text{ }\mu\text{m}$, and **Magenta:** $120 \text{ }\mu\text{m}$).....96

Figure 4.4 Equivalent circuit used to fit the electrochemical impedances.....98

Figure 4.5 Impedance curves at 1V overpotential (normalized with respect to Au-YSZ interface area, 16 mm^2 for all four electrodes) of four different thicknesses porous Au anodes with various fuel fractions of **dry** H_2 (**Orange:** $30 \text{ }\mu\text{m}$, **Green:** $60 \text{ }\mu\text{m}$, **Blue:** $90 \text{ }\mu\text{m}$, and **Magenta:** $120 \text{ }\mu\text{m}$) Symbols are experimental data and lines are data from equivalent circuit fits.....100

Figure 4.6 The plot of Au anode thicknesses vs. $R_{\text{an, Diff}}$ values at 1V overpotential from equivalent circuit fits with various dry H_2 fuel fractions.....102

Figure 4.7 The plot of $p(\text{H}_2)$ vs. $R_{\text{an, Diff}}$, H_2 partial pressure dependence of $R_{\text{an, Diff}}$ at 1 V overpotential from equivalent circuit fits with various dry H_2 fuel fractions (**Orange:** $30 \text{ }\mu\text{m}$, **Green:** $60 \text{ }\mu\text{m}$, **Blue:** $90 \text{ }\mu\text{m}$, and **Magenta:** $120 \text{ }\mu\text{m}$).....103

Figure 4.8 Polarization curves (normalized with respect to Au-YSZ interface area, 16 mm^2 for all four electrodes) of four Au anodes with various fuel fractions of **wet** H_2 **Left:** whole range of polarization curves, **Right:** details in maximum current density regions (**Orange:** $30 \text{ }\mu\text{m}$, **Green:** $60 \text{ }\mu\text{m}$, **Blue:** $90 \text{ }\mu\text{m}$, and **Magenta:** $120 \text{ }\mu\text{m}$).....104

Figure 4.9 Impedance curves at the 1V overpotential (normalized with respect to Au-YSZ interface area, 16 mm^2 for all four electrodes) of four Au anodes with

various fuel fractions of **wet H₂** (**Orange**: 30 μm , **Green**: 60 μm , **Blue**: 90 μm , and **Magenta**: 120 μm) Symbols are experimental data and lines are data from equivalent circuit fits.....106

Figure 4.10 The plot of Au anode thicknesses vs. $R_{\text{an, Diff}}$ at 1V overpotential from equivalent circuit fits with various wet H₂ fuel fractions.....107

Figure 4.11 The plot of $p(\text{H}_2)$ vs. $R_{\text{an, Diff}}$, H₂ partial pressure dependence of $R_{\text{an, Diff}}$ at 1 V overpotential from equivalent circuit fits with various wet H₂ fuel fractions (**Orange**: 30 μm , **Green**: 60 μm , **Blue**: 90 μm , and **Magenta**: 120 μm).....108

Figure 4.12 Polarization curves (normalized with respect to Au-YSZ interface area, 16 mm² for each) of four different thicknesses porous Au anodes with dry and wet H₂, isotopically labeled HD and D₂ (**Orange**: 30 μm , **Green**: 60 μm , **Blue**: 90 μm , and **Magenta**: 120 μm).....109

Figure 4.13 Impedance curves at 1V overpotential (normalized with respect to Au-YSZ interface area, 16 mm² for all four electrodes) of four different thicknesses porous Au anodes with dry/wet H₂ and D₂ at 70 sccm fuel fraction (**Orange**: 30 μm , **Green**: 60 μm , **Blue**: 90 μm , and **Magenta**: 120 μm) Symbols are experimental data and lines are data from equivalent circuit fits. (Note: the graph depicting the wet D₂ impedance is shown with different scales for aesthetic purposes).....110

Figure 4.14 Porous Au anode thicknesses vs. $R_{\text{an, Diff}}$ values from equivalent circuit fits with 70 sccm dry/wet H₂-D₂ flows.....111

Figure 4.15 Schematic representation of SOFC assembly employed in modeling studies.....114

Figure 4.16 Comparison of experimental and simulated data from different thickness porous Au anodes with various dry H₂ fuel fractions (**Orange**: 30 μm and **Magenta**: 120 μm).....116

Figure 4.17 Comparison of experimental and simulated data from different thickness porous Au anodes at 70 sccm dry H₂ and D₂ fuel fractions (**Orange**: 30 μm and **Magenta**: 120 μm).....117

Chapter 1:

General Introduction

1.1. Overview:

Energy is as essential as food and water for humankind. Developing clean, economical, and sustainable energy sources is a major goal of much research. Fuel cells are clean and efficient energy conversion devices that convert chemical energy directly to electrical energy by electrochemical combination of a fuel and an oxidant. Conventional production of electrical energy is by combustion in combination with a generator or using a combustion engine, where the Carnot-cycle sets a limit to 35 % efficiency for an regular combustion engine [1, 2]. However, fuel cells are not limited by the Carnot efficiency because they rely on electrochemical processes. A fuel cell working as a type of continuously replenished battery offers an alternative. Products of the fuel cell are in principle only water, heat and CO₂. Fuel cells offer the higher efficiency and the low pollution than other energy producing technologies. Fuel cells could be a part of power plants to enable the development of electricity generation with ~60 % efficiency [3, 4] and the energy production can be adjusted to meet the actual demand. This is a main research aspect for a power source in a scientific and industrial society.

The idea of fuel cell was first elaborated by Sir William Grove [5], who demonstrated the reversibility of electrolytic water splitting in 1839. In 1899 Nernst [6] contributed by presenting that certain oxides achieved remarkably high electrical

conductivity by doping with other oxides. However, it was not until the 1950's that fuel cells became a commercial product. They were developed in 1960's when the American space program began using fuel cells in the Apollo Program. In the beginning of 1980s, due to the focus on environmental priorities and the demand for higher efficiency in energy conversion by realizing the scarcity of fossil resources, fuel cell research was initiated as a growing and an attractive research area. Several types of fuel cells were developed in last five decades. Currently, many types of fuel cells are approaching the market within a limited number of years. The primary challenges for fuel cells commercialization are the storing fuel, material cost and material stability to be solved by the researchers. There are also other issues to address for fuel cell materials such as catalytical activity of anodes and cathodes, compatibility to each other, and purity.

There are five different fuel cells commonly known, and all are named after their electrolyte materials. Each type of fuel cell [7, 8] has different characteristics, such as operation temperature, efficiency, charge carrier ion, and demand for fuel composition, and these are listed in Table 1.1.

Table 1.1: Different types of fuel cells

Name	Abb.	Electrolyte	Charge Carrier	Fuel	Operation Temperature	Efficiency
Alkaline Fuel Cell	AFC	KOH	OH ⁻	Pure H ₂	50-200 °C	35-40 %
Polymer Electrolyte Membrane Fuel Cell	PEMFC	Polymer (Nafion)	H ⁺	Pure H ₂ and ethanol	50-100 °C	35-40 %
Phosphoric Acid Fuel Cell	PAFC	H ₃ PO ₄	H ⁺	CO free H ₂	200-220 °C	30-40 %
Molten Carbonate Fuel Cell	MCFC	Li ₂ CO ₃ (62%) + K ₂ CO ₃ (38%)	CO ₃ ²⁻	H ₂ , and hydrocarbons	600-650 °C	60-70 %
Solid Oxide Fuel Cell	SOFC	ZrO ₂ + Y ₂ O ₃ (YSZ)	O ²⁻	H ₂ , and hydrocarbons	650-1000 °C	60-75 %

The first three types of cells in Table 1.1 require relatively pure hydrogen fuels. Accordingly, the use of hydrocarbon or alcohol fuels requires an external fuel reforming step to separate hydrogen from hydrocarbon sources. This not only increases the complexity and the costs of the system, but also decreases the overall efficiency [8]. The efficiency is calculated by current output of the device divided by theoretical current of fuel put into the device. For MCFCs and SOFCs, it is expected that hydrocarbon fuels can also be utilized directly, without reforming, since they operate at higher temperatures. These higher temperatures provide higher hydrocarbon fuel utilization efficiencies, and enhanced efficiency. For example, the thermodynamic efficiency of the SOFC for methane conversion is calculated as 100 % at SOFC operating temperatures [9] and the chemical-to-electrical efficiency of methane exceeds to 45 % in SOFC systems. Therefore, the overall SOFC efficiency observed for methane fuels is 60-65 % [9]. However, the high operating temperatures can cause the shorter life times for fuel cell components. In addition, high temperature gas seals in these types of fuel cells impose another technical problem that has still not been overcome.

The objectives of this thesis are classified into two categories: i) the structural and morphological characterization of carbon deposits accumulated on Ni/YSZ and Cu/CeO₂/YSZ anode systems when butane is employed as the fuel (see in Chapter 2); ii) the addressing the questions about the role of YSZ in fuel oxidation catalysis and the role of Au, used as a current collector in conventional SOFC systems, on anodic H₂ oxidation kinetics in SOFC (Chapters 3 and 4).

Since carbon deposition on SOFC anode surfaces reduces the integrity and the performance of SOFCs [10, 11], the understanding of the structure of carbon deposits formed on SOFC anodes systems provides a basis for understanding the mechanism of electrochemical oxidation of hydrocarbons in a SOFC so that improved SOFC anode materials and architectures can be explored.

The simplest fuel for SOFCs is hydrogen and its unknown oxidation mechanism precludes the determination between current collection and electro-catalytic properties of SOFC anode and electrolyte materials. The understanding the YSZ and Au contribution on hydrogen oxidation mechanism provides the basis for understanding H_2 oxidation on more complex systems (i.e. Ni, or Cu/CeO₂). In addition, the Au-anode/ YSZ-electrolyte architecture is the simplest system to develop quantitative mechanism for surface diffusion, charge transfer, and chemical processes.

1.2. Solid Oxide Fuel Cell (SOFC):

The first SOFC was developed in 1937 by Baur and Preis [12]. Due to many improvements in material science and process engineering, much progress has been made after the first SOFC. The most significant advantage of the SOFC is its fuel flexibility and potential to be a clean and efficient energy conversion device. Since SOFCs can hopefully utilize conventional hydrocarbon fuels, it can be the transition energy conversion device from fossil fuels to hydrogen. However, due to high temperature needed for operation, the main components of SOFCs currently have

insufficient long-term stability [13]. Also, the high cost and handling difficulties of SOFC ceramic components have prevented commercialization.

1.2.1. Principles of SOFC operation:

The operating scheme of the SOFC is presented in Figure 1.1. SOFCs consist of three main components: (i) an electrolyte that conducts only O^{2-} ions and is impermeable to gaseous species, (ii) a cathode that catalytically reduces oxygen, and (iii) an anode that catalytically oxidizes fuel. The driving force for O^{2-} ion transport is the production of water and/or CO_2 at the anode. This provides the difference in oxygen activity of two gases, namely oxygen and hydrogen. The primary reaction site on the anode is called the triple phase boundary (TPB), where the anode material, electrolyte, and fuel gas phase meet. The O^{2-} ions are produced by catalytic dissociation of oxygen at the cathode under current load, and then transfer through the electrolyte to the anode TPB where they react with dissociatively adsorbed fuel species to form products. Adsorbed fuel species are formed by consecutive charge-transfer reactions, and then, electrons are discharged to current collector on anodes. The released electrons on the anode pass through external current load, and then they are again used for oxygen reduction to complete the circuit.

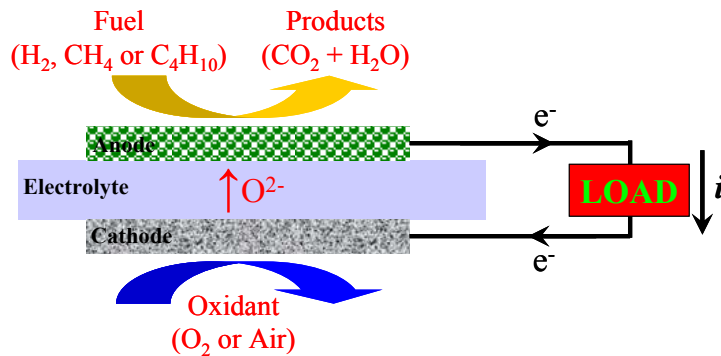


Figure 1.1 Schematic representation of SOFC assembly operation (the anode and cathode sides are physically separated from each other by a dense electrolyte and high temperature ceramic sealing).

1.2.2. Electrolytes:

SOFC electrolytes are ionic conductors that transport O^{2-} ions through vacant oxygen lattice sites available in the crystal structure [14-17]. This process is accomplished by doping of one oxide material into other one to create oxide lattice site defects. For conventional SOFCs, yttria (Y_2O_3) doped zirconia (ZrO_2), which is called yttria stabilized zirconia (YSZ), exhibits not only high ionic conductivity but also extraordinary mechanical properties at SOFC operation temperatures. The monoclinic crystal structure of ZrO_2 is favored at temperatures up to 1150 °C, and thermodynamically stable fluorite-type crystal structure of cubic ZrO_2 exists only at temperatures above 2400 °C. However, when ZrO_2 doped with Y_2O_3 , the fluorite-type crystal structure becomes stable at room temperature [18] [19]. Doping ZrO_2 with Y_2O_3 creates oxygen vacancies in the fluorite-type crystal lattice. These oxygen vacancies are responsible for O^{2-} conductivity. The optimized doping percentage of yttria, 8 mol % ($Zr_{0.92}Y_{0.8}O_{1.92}$), provides maximum oxide conductivity and is the electrolyte choice for SOFCs [19]. Other than YSZ, a number of alternative materials have been examined in the literature and applied by other companies. Recently, gadolinium doped ceria, $Ce_{0.9}Gd_{0.1}O_{1.95}$ (GDC or CGO) electrolytes have been studied for SOFCs operating at intermediate temperatures (600-800 °C), due to their high ionic conductivity [20, 21]. However, GDC causes performance losses by short circuiting current from the anode to the cathode due to its mixed conducting (ionic and electronic) properties [22]. The highest ionic conductivity was found for $La_{0.9}Sr_{0.1}Ga_{0.9}Mg_{0.1}O_3$ (LSGM) [23-25]. However, the cost of LSGM prohibits it from being exploited as a conventional electrolyte in SOFC.

1.2.3. Cathodes:

SOFC cathodes need to have high ionic-electronic conductivity, good O₂ reduction catalytic activity, and stability at SOFC operation conditions. The traditional cathode material for SOFCs is a perovskite-type strontium doped lanthanum manganite, La_{0.8}Sr_{0.2}MnO_{3-δ} (LSM). This material shows high electro-catalytic activity for oxygen reduction and mixed ionic-electronic conductivity [26]. However, LSM reacts with the YSZ electrolyte at higher temperatures to give a non-conducting lanthanum zirconate, La₂Zr₂O₇ (LZO) interlayer is formed [27, 28]. LZO formation at the cathode is detrimental because it decreases the cathode electronic conductivity and prevents the charge-transfer reaction in oxygen reduction. Therefore, the sintering temperature of LSM materials must be optimized to maximize adhesion to YSZ, but avoid LZO formation. At intermediate temperatures, 600-800°C, strontium and cobalt doped lanthanum ferrate, La_{0.8}Sr_{0.2}Cr_{0.2}Fe_{0.8}O_{3-δ} (LSCF), is an advantageous alternative for the SOFC cathodes due to its higher mixed electronic-ionic conductivity [24, 29, 30]. However, the long-term stability of LSCF under SOFC conditions is not good. Another choice as a cathode material for SOFC is samarium strontium cobaltate, Sm_{0.5}Sr_{0.5}CoO_{3-δ} (SSC), which can be used at even lower temperatures (500°C), but SSC is not compatible with YSZ due to their different thermal expansion coefficients at this temperature range [31, 32]. Strontium doped lanthanum cobaltate, La_{0.8}Sr_{0.2}CoO_{3-δ} (LSCo) has higher electronic conductivity. However, its thermal expansion coefficient also deviates from that of YSZ, and its reactivity toward YSZ also leads to the formation of non-conducting zirconates [33, 34]. This difference in thermal expansion is mitigated by thin functional layers.

1.2.4. Anodes:

SOFC anodes need to have high ionic-electronic conductivity, good fuel oxidation catalytic activity, and stability at SOFC operation conditions. The conventional anode material is a highly porous Ni/ceramic composite (50-50 % Ni/YSZ systems, particle size of Ni $\sim 1\ \mu\text{m}$) [35-37]. Ni/YSZ systems is extensively used due to its excellent catalytic properties for hydrogen oxidation, its low reactivity toward other SOFC components and its low cost [36]. The Ni/YSZ composite anode is usually fabricated from a NiO/YSZ mixture, and then reduced to a Ni/YSZ cermet under a hydrogen atmosphere. The re-oxidation of the anode results in an expansion of about 30% in the Ni phase. This causes a separation from the anode composite and YSZ electrolyte [38]. Another drawback of Ni/YSZ cermet anodes is carbon deposit formation with hydrocarbon fuels. This causes clogging in gas channels, blocking of active Ni surface sites and physical disintegration of the porous anode structure [39]. Therefore, Ni-based anode systems are not suitable for direct operation with hydrocarbon fuels with current design architectures.

For conventional hydrocarbons, ceria, CeO_2 , is an alternative SOFC anode material due to its mixed ionic/electronic conductivity [40-42]. However, the $\text{Ce}^{3+}/\text{Ce}^{4+}$ redox couple causes also volume changes in SOFC anodes and generates structural instabilities. By doping with gadolinium, the change in volume is reduced but not eliminated completely [42]. Gadolinium doped ceria, GDC, anode systems have attained almost the same performance as Ni/YSZ systems with hydrogen, and carbon formation is not observed with methane [43-47]. However, GDC has inadequate adhesion to the YSZ electrolyte [48] and relatively high cost. In recent reports, other

anode cermet compositions, such as Ni-ceria, or Cu-ceria were used with hydrocarbon fuels, but these materials were also reported to have considerable limitations [49-53]. Ni promotes coking [54-56] and Ni-ceria was only successfully used only with methane and at relatively low temperatures ($\sim 500^{\circ}\text{C}$). Copper-ceria is better suited for larger hydrocarbons as coking has not been observed in Cu-based systems [57-60]. However, Cu is a poor electrocatalyst in comparison to Ni, and has a relatively low melting point. As such, it is not compatible with many standard high temperature SOFC fabrication techniques [61]. Recently, GDC with the addition of a better ionic conductor (lanthanum strontium chromium manganite), and with a low Ni content ($\sim 4\%$) have been used as SOFC anodes [62, 63]. This composition shows enhanced performances not only with hydrogen but also with methane, propane and butane.

Titanium doped YSZ (Ti/YSZ) systems have also drawn increased interest as SOFC anode materials [64, 65]. These systems have a thermal expansion coefficient comparable to YSZ and a better electrical conductivity. Addition of Ni to Ti/YSZ systems reduces the agglomeration tendency of Ni particles so that these anode systems improve the SOFC performance and diminish the degradation rate around 1000°C [66].

1.2.5. Planar SOFC cell designs:

The two basic structural designs for SOFCs are tubular and planar cells [41, 67-69]. The planar SOFC design is important for the commercial SOFC systems, because single SOFC cell can only deliver around 1 V. Therefore, to obtain useful voltages many planar SOFC cells are generally stacked in series, called a SOFC stack. In

addition, the planar design is easier to fabricate and more convenient for experimental access.

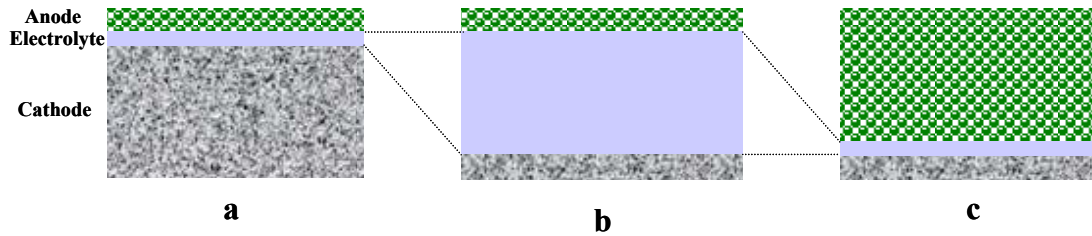


Figure 1.2 Planar cell designs a) cathode supported cell, b) electrolyte supported cell, and c) porous anode supported cell, drawings not to scale.

As shown in Figure 1.2, the planar cell can be designed in several ways. Each design has advantages and disadvantages. Cathode supported design has an advantage of low ohmic losses in the electrolyte [41, 68]. However, the cathode supported cell design is not preferred because the thick cathode (0.5-1 mm) creates an excessive concentration loss (especially if air is used) causing the decrease in oxygen reduction reaction rate. The problem for this design is caused by poor electronic conductivity of current cathode materials [68]. Therefore, a thin SOFC cathode layer draws more interest in SOFC cell designs.

Electrolyte-supported cell designs supply excellent physical strength to the SOFC with thin cathode and anode layers. Thick electrolyte (0.2-1.5 mm) support designs are employed for research purposes to address questions about the SOFC anode and cathode systems [26, 41]. The electrolyte supported design provides an experimental foundation for utilizing many different fabrication techniques and different anode and cathode materials [26]. The drawback of the electrolyte supported cell design is that the very large ohmic resistances are generated by thick electrolyte, which limits the

conventional SOFC performance. However, the electrolyte resistance can be reduced by co-doping scandia into YSZ [70, 71].

Recent advances in physical and chemical vapor deposition techniques are being employed in the fabrication of thin electrolyte layers. Electrolyte and anode deposition techniques differ in deposition rates, substrate temperature during deposition, precursor materials, necessary equipment, cost, and quality of the resulting film [41, 68, 69]. These advances drive great interests in constructing porous anode (0.5-2 mm thickness) supported cell design to make a commercial SOFC on the market. The anode supported cell design advantages are high mechanical strength, adjustable cathode size, and high performance. However, the redox couples of some of the anode materials, for example Ni/Ni^{2+} and $\text{Ce}^{3+}/\text{Ce}^{4+}$, increases stresses in anode supported SOFC assembly during oxidizing-reducing cycles [40, 72]. The vulnerability of cracking and pinholes in the thin electrolyte (10-20 μm) increases the risk of hydrogen leaks to the cathode, which will decrease the SOFC performance [73]. The wet impregnation techniques, which is the consecutive addition of the solution of nitrates or sulfates of each components into porous anode matrix, are used to include other components of the anode supported SOFCs [74, 75]. Physically strong porous anode supports are prepared from one anode component (usually YSZ electrolyte phase) with subsequent addition of components and final sintering under hydrogen atmosphere.

1.2.6. Performance limiting processes:

In practice, there are several sources of voltage loss in SOFCs from reversible cell voltage. The reversible cell voltage or Nernst potential is given by $V_{rev} = -\Delta G/nF$ where ΔG is the free energy of global oxidation reaction in SOFC. The internal voltage losses (or overpotentials) of SOFCs can be separated into two categories: ohmic and non-ohmic [76]. The ohmic losses (IR drops) are caused by the resistances of the electrolyte, anode, and cathode, in which the two latter resistances are negligible in real SOFCs. Non-ohmic losses result from physical and chemical processes taking place on cathode and anode, and also called overpotential losses [13].

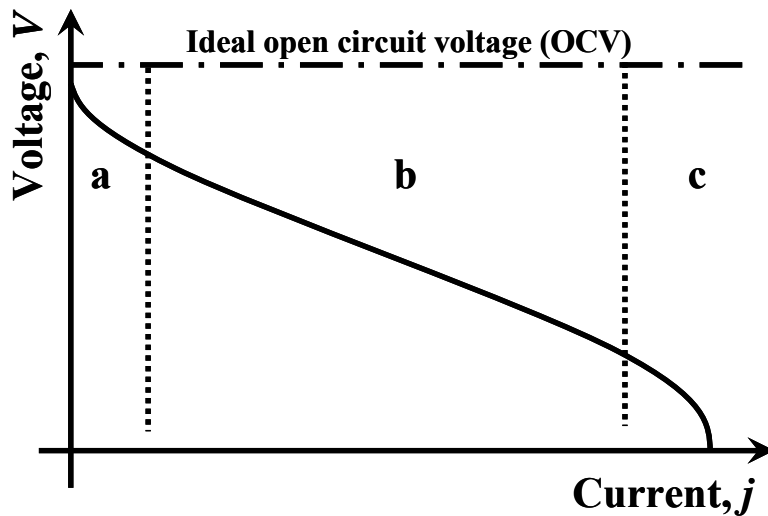
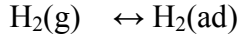


Figure 1.3 Schematic graph of the voltage drop of SOFC as a function of withdrawn current density, a) low current regime, b) medium current regime, and c) high current regime.

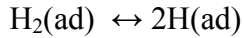
Different chemical and physical processes dominate the loss in different current or voltage ranges. Figure 1.3 shows how the cell polarization of typical SOFC changes

with the current density withdrawn. Three regions can be identified: low (Figure 1.3 part a), medium (Figure 1.3 part b) and high current (Figure 1.3 part c) output. In the low current regime it is the reactions at the electrodes that limit the electrochemical conversion in the SOFC. Charge-transfer reaction losses mostly dominate the power losses, which are referred as activation overpotential, and are shown in Figure 1.3 part a. Since the effect of the activation overpotential losses decays exponentially through medium current region, the ohmic drop (IR) begins to dominate the shape of the polarization curve. The pure ohmic drop is linear for the whole polarization curve and its effect is clearly seen in Figure 1.3 part b. The linear ohmic drop is caused by the low ionic conductivity of the electrolyte, which is constant at SOFC operation temperatures. A second loss is due to the need for concentration gradients in the porous electrode structures. This drop in concentration reduces the free-energy change in reaction 1.1 and thus causes a drop in voltage. This is modeled as overpotential due to transport. A third is due to the decrease in voltage drop at the so-called three-phase boundary to drive the charge transfer reactions. This overpotential is referred to the activation overpotential.

In every regime the types of reactions dominating current can be elucidated from polarization curves; to explain the limiting processes simplified hydrogen oxidation kinetics steps will be used as a model. The activation losses of hydrogen in an SOFC are displayed in the low current regime and believed to occur in two steps: dissociative adsorption of hydrogen (1.1 and 1.2), and charge-transfer reactions (1.3, 1.4, 1.5, and 1.6).



1.1 Adsorption

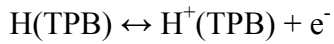


1.2 Dissociation of H_2

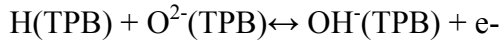
Since these two reactions (1.1 and 1.2) are consecutive, these two steps are combined and called dissociative adsorption of hydrogen. Charge transfer reactions also affect the SOFC performance in the low current regime. Although there are many possibilities for transporting electrons from adsorbed species to the electrode, four different charge transfer reactions (1.3, 1.4, 1.5, and 1.6) have been proposed:



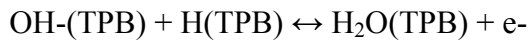
1.3 Electrochemical process on anode surface



1.4 Electrochemical process at TPB



1.5 Charge transfer at TPB



1.6 Charge transfer at TPB

The first two reactions (1.3 and 1.4) occur on the electrode. These reactions are not literally called charge transfer reactions, but are electrochemical processes on the electrode as a part of an electrochemical mechanism. These reactions are reported to be fast and not controlling the charge transfer processes reported in the literature. However, the last two reactions (1.5 and 1.6) in this group need O^{2-} ions, which are only available at the TPB. Therefore, the shape of low current regime is dominated by dissociative adsorption of hydrogen and two consecutive charge transfer reactions. The activation losses can be lowered by increasing the reaction rates.

Pure ohmic losses in the medium current regime are mostly caused by the electrolyte ionic resistance in the transport of O^{2-} ions as seen in Figure 1.3 part b. To

reduce the ohmic losses, different types of electrolyte, cathode and anode materials with higher ionic conductivities are needed.

Lastly, the high current regime is dominated by mass transport processes of reactants and products.



When the electrolyte supported design is used, the working electrode is a thin porous anode. The current density drawn from this anode is fairly low. The gas-phase diffusion of hydrogen in the anode is fast as compared to surface diffusion, and not a limiting factor in the SOFC performance. However, the surface diffusion (1.7, 1.8, and 1.9) of adsorbed fuel species and water on the SOFC anode surface can become very significant in the last regime.

$$OCV = E_{cell} = -\Delta G_{reaction}^o/nF + RT/nF \ln(P_{products}/P_{reactants}) \quad 1.11 \text{ Nernst Potential}$$

where $-\Delta G_{reaction}^o$ is Gibbs free energy; P is pressure; n is number electrons; F is Faraday constant; R is gas constant; T is temperature in Kelvin. The water desorption reaction (1.10) from the TPB affects both the activation loss (in the low current regime), and the mass transport loss (in the high current regime). In the low current regime, the open circuit voltage, OCV, (1.11 Nernst potential) of the SOFC is impacted by the amount of water at the anode. In the high current regime the water desorption reaction rate affects the number of reactive sites available for surface diffusion of adsorbed species and for the charge-transfer reaction. Therefore, the

effect of water desorption would also be seen in the high current region in Figure 1.3 part c.

Electrochemical impedance spectroscopy, EIS, is employed extensively to investigate physical and chemical processes in SOFCs. All of these reactions above and their effects can be monitored by EIS. Impedance measurements as a function of overpotential are used at different points of polarization curve (Figure 1.3), in which the certain overpotential is applied between the anode and the cathode [77]. An alternating voltage, $\Delta V(\omega)$, is imposed at constant overpotential of the cell and the response is measured in terms of an alternating current, $\Delta j(\omega)$:

$$\Delta V(\omega, t) = V_m \cdot e^{-i\omega t} \quad 1.12$$

$$\Delta j(\omega, t) = I_m \cdot e^{-i(\omega t + \phi)} \quad 1.13$$

where t is the time, V_m and I_m are the magnitudes for voltage and current respectively, ω is the angular frequency, and ϕ is the phase difference between the voltage and the current. The impedance, Z , is defined as

$$Z(\omega) = \Delta V(\omega, t) / \Delta j(\omega, t) = (V_m / I_m) \cdot e^{i\phi} \quad 1.14$$

By using the Euler equation

$$e^{i\phi} = \cos \phi + i \sin \phi \quad 1.15$$

the impedance would be

$$Z(\omega) = Z_{re}(\omega) + Z_{im}(\omega) \quad 1.16$$

in which

$$Z_{re}(\omega) = \text{real} (Z) = |Z| \cdot \cos \phi \quad 1.17$$

$$Z_{im}(\omega) = \text{imag} (Z) = |Z| \cdot \sin \phi \quad 1.18$$

$$|Z| = V_m / I_m = (Z_{re}^2 + Z_{im}^2)^{1/2} \quad 1.19$$

$$\tan \phi = Z_{im}(\omega) / Z_{re}(\omega) \quad 1.20$$

The impedance data is typically plotted in the Nyquist representation (Figure 1.4) where the negative imaginary part of impedance, Z_{im} , is plotted vs. the real part of the impedance, Z_{re} .

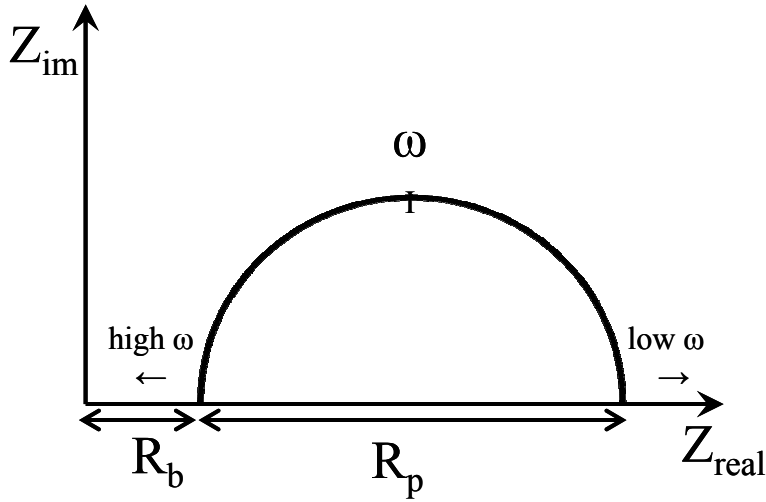


Figure 1.4 Schematic representation of EIS Nyquist plot.

The real part, Z_{real} , on the x -axis represents resistive processes of impedance curve, and the imaginary part, Z_{im} , on the y -axis represents capacitive processes of an impedance curve. The bulk resistance, R_b , is dominated by the electrolyte and interconnects. R_b can be measured from the high frequency part (left hand side on x -axis) of the Nyquist plot. Low R_b values are interpreted as the reduction of the ohmic drop in the SOFC systems and the better performance of SOFC systems. The intercept at low frequency (right hand side on x -axis) is called the total resistance, R_T ,

which is the sum of the resistances of the entire SOFC system. The difference between R_T and R_b gives the polarization resistance, R_p . All physical and chemical processes on both cathode and anode are integrated into R_p . Therefore, all reactions given above would be represented by this single arc in the EIS curve. However, multiple arcs can be observed in these systems if the processes are taking place in different frequencies (ω). R_p values are directly related with the overpotential losses in the SOFC system. Hence, by monitoring and evaluating R_p values, overpotential losses from reaction steps can be modified for the SOFC systems. The relaxation frequency, ω , is defined as the frequency at the maximum imaginary impedance value. In the case of several relaxation processes (several arcs), there exist several relaxation frequencies which can be identified as local maxima in the Nyquist plot and attributed to different processes. The relaxation frequencies are related with the rate of reactions on each reaction, where the faster reactions take place at high frequency.

EIS data [77] are generally analyzed either by fitting the data to an equivalent circuit consisting of resistances, capacitances, and inductances or by simulations written for special SOFC systems. The main difficulty with the fitting method is related to the physical and the chemical interpretation of the equivalent circuit elements. There are limited amounts of studies for simulating EIS data using detailed kinetic and transport models.

1.3. Fields of Research:

The specific energy of hydrogen is the highest of all fuels, but the lowest in the volumetric energy density. The storage and transportation of H₂ is a problem yet to be addressed for implementing the hydrogen economy. Although hydrogen is considered as an ideal fuel for many energy-conversion systems, its widespread use is dependent on technological advances in its cost and storage. Hence, it is best to assume that in the near future, SOFCs would have to utilize hydrocarbons as fuel.

Essential consumption of hydrocarbons on SOFCs has forced researchers to explore catalysts directly converting the chemical energy of hydrocarbon fuels to electrical energy without additional external chemical reactors. The process to strip electrons from a fuel molecule for clean and efficient energy production is called direct electrochemical oxidation (DECO) of fuels. Conventional Ni/YSZ anodes for SOFCs have been examined and realized having problems on DECO of hydrocarbon fuels that carbon deposit is formed at Ni anodes at high temperature and this formation causes the degradation of the anode material [39, 78]. The challenges about the DECO of hydrocarbons and the degradation of Ni/YSZ anodes have been studied mostly by Gorte, Barnett, Virkar, and Mogensen.

The performance and degradation of SOFCs under severe operation conditions have been examined by Mogensen [37, 72, 79-81]. The mixture of hydrogen-methane containing 5-50 % water on the Ni/YSZ supported SOFCs with the current densities of 0.25-1 A/cm² have been tested for about 300 hours. The analysis of results has revealed that the degradation of Ni/YSZ anode supported cell was dependent on the fuel gas composition, operation temperature and the current density. The reason of the

anode degradation has been explained by the separation of Ni and YSZ phases [79-81]. The rate of degradation of SOFC anode has been optimized to the conditions of running cell voltage at 0.7 V at 850 °C and 0.75 at 750 °C, the current density at 1 A/cm², and the steam to carbon ratio of 2:1 [80].

Dean has described the carbon formation problem and has examined whether or not gas phase reactions of higher hydrocarbons at high temperature range can cause this coke formation without electrochemistry [82]. The analysis of products of internal reforming of butane at the temperature range of 550-800 °C and the pressure of 0.8 atm, and residence time of 5 seconds has shown that the main products of butane reforming were 36.3 % methane, 39.8 % ethylene, 13.0 % propylene, less than a percent ethane and hydrogen, and the fraction of four and five carbon chains in the gas phase. These results have raised the question about the actual fuel speciation resulted from pyrolysis, but not butane itself, causing the coking at this high temperature range.

Gorte and co-workers have developed Cu/CeO₂/YSZ anodes in order to solve the coking problem because Cu has a lower activity for the cracking reaction [39, 78]. These anodes always performed worse with hydrocarbons than the conventional anodes operating with hydrogen, the reason being the low catalytic activity of Cu. However, the butane fuel supply on Cu/CeO₂/YSZ anodes resulted in superior power densities of SOFCs running hydrogen after carbon deposit formed. The reason of superior performance was proposed by Gorte *et.al.* [58, 74] that the conductivity of Cu/CeO₂/YSZ anode systems enhanced after carbon deposition. However, the chemical and physical nature of these carbon deposits remained unclear.

Recently, Hibino[83, 84] has operated SOFCs with dry methane at a fuel utilization of 50% and obtained a maximum power output of 500 mWatts/cm². The anode in this study was based on gadolinium doped ceria (GDC) containing NiO. Also, RuO₂ (3 wt %) had been added to the anode, which was proposed as the reason for the resistance of the anode to carbon deposition and the good performance [83, 85]. However, the employment of RuO₂ on SOFC anodes increases the cost of the entire SOFC assembly. The challenges of GDC anodes are establishment adequate adhesion to the electrolyte without detrimental reactions and lowering fairly high materials cost.

Octane has been used in the SOFC systems by Barnett [86-88] to explore the longer chain hydrocarbon fuels such as gasoline on Ni/YSZ anodes with RuO₂. Although the author emphasized much work required having SOFC working with gasoline, the published results have shown significant power densities (0.3-0.6 Watts/cm² from 5-9 % iso-octane) without any carbon deposit on the anode.

Virkar [89, 90] has shown the great interest to the mechanical properties of Ni/YSZ anodes at SOFC operation conditions. Recently, the reduction and re-oxidation kinetics of Ni-based SOFC anodes have been studied by this group. The effect of small amount of CaO, MgO, and TiO₂ to Ni/YSZ anodes has been evaluated for the entire SOFC anode stability. The results have shown that doping of CaO, MgO, and TiO₂ to Ni/YSZ systems suppressed both the reduction and re-oxidation kinetics of Ni-based anodes. The earlier work from Virkar has addressed the activation and concentration polarization effects for the LSM cathode in anode supported SOFCs. The principal losses in SOFCs were attributed to the activation polarization due to charge-transfer reactions and the concentration polarization due to gas phase transport

through the thick anode, when the electrolyte was a 10 μm film on a 1 mm thick anode.

The reaction mechanism of oxygen reduction on the SOFC cathode has been addressed by Fleig and co-workers [26, 91-94]. These authors have studied the possible pathways (Figure 1.5a) of oxygen reduction on dense LSM by using different thickness of LSM and by using sub-surface alumina blocking (Figure 1.5b) in between the dense LSM and the YSZ electrolyte. The authors have proposed that oxygen is reduced in the bulk LSM not in the interface between cathode and electrolyte. The catalytic properties of the cathode were found to be more significant than the conductivity.

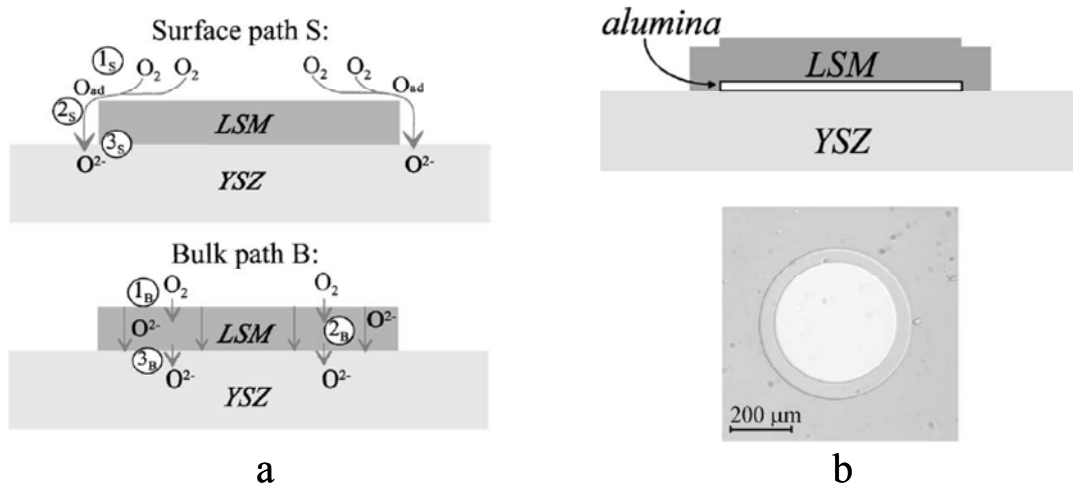


Figure. 1.5 a) Oxygen reduction pathways on conventional LSM-YSZ cathodes, b) Experimental setup for alumina blocking experiments from Fleig *et al.* [92].

The nature of the electrolyte dictates the operating temperature and the chemistry of the reactions occurring at the electrodes. For conventional SOFCs, the most common electrolyte material is YSZ. The main problem of YSZ is the high temperature (800-1000 $^{\circ}\text{C}$) requirement to enable the transport of oxide and oxygen vacancies through

the electrolyte [14-17]. Therefore, the challenges for the SOFC electrolyte need to be resolved by breakthrough materials reducing the SOFC operation temperature, and having excellent mechanical strength. Recently, doped-ceria based electrolyte materials have been tested by many different groups due to the high interest in ceria based anodes and their compatibility to ceria based electrolytes. However, ceria based electrolyte materials have the mixed type conductivity of both electronic and ionic, causing the leak in SOFC performance. The doping of gadolinium and samarium to ceria based anodes has been thought to resolve the problems about the lowering the operation temperatures and mechanical integrity at these temperatures [20-22].

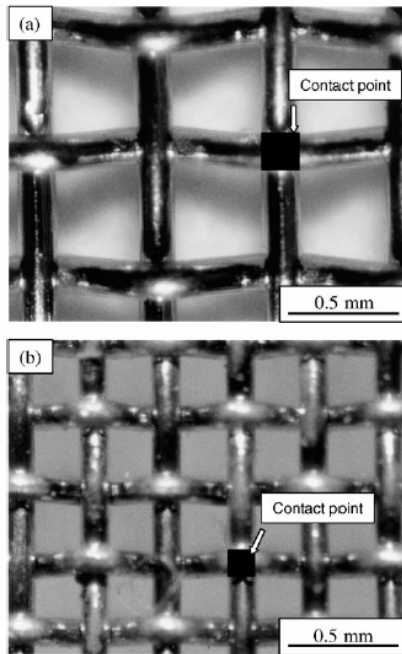


Figure 1.6 Current collector experiments designs from Jiang on the SOFC cathodes, a) 0.032 mm² current collector area, b) 0.012 mm² current area of Pt and Ag from Jiang *et al.*[95].

Current collection on anodes and cathodes of SOFCs has been discussed starting from the beginning of SOFC research, due the low electronic conductivity of the electrocatalyst cermets. It has been known that the increase in the current collection area on both Ni/YSZ anodes and LSM-YSZ cathodes causes the enhancement in the

SOFC performance [80, 90, 95-100]. The current collection experiments with different contact areas (Figure 1.6) on SOFC cathodes have been reported by Jiang [95]. Pt and Ag mesh with various waven mesh and crossover sizes have been employed as current collectors (Figure 1.6). The current collection area has been assumed to be the sum of areas of crossover points of waven mesh. By using the Ni/YSZ anode supported SOFC experimental design for the cathode current collector experiments, the authors have demonstrated that the increase in the contact area between cathodes and current collectors reduced both cell resistance (from $1.43 \Omega \cdot \text{cm}^2$ to $0.26 \Omega \cdot \text{cm}^2$) and cell overpotential losses (from 225 mV to 119 mV at the current density of $250 \text{ mA}/\text{cm}^2$).

Basic research has had much intention to tackle with the question about the length scale of current collection on the SOFC electrodes. The amount of the inert and expensive metals such as Au, Pt, and Ag used as current collectors on the conventional SOFC electrodes could be reduced. The length scale of the current collection is defined as the distance from the current collector perimeters at which electrons are carried out to the SOFC load [95, 101-103]. The distance of current collection depends on conductivities of the SOFC electrode materials. and is believed to be in nanometer scale [95, 102]. The challenge to address the length scale of current collection is the requirement of the nanometer scale patterns of current collectors on conventional SOFC electrodes.

The computational analysis of SOFC systems facilitates the better understanding of the experimental data in SOFC research and then, aids to have better choices of

designs. By employing a number of modeling approaches, the simplified SOFC systems and their behavior with different fuels have been simulated.

The polarization curve simulation of SOFC systems is the method used extensively to elucidate the parameters of electrode processes. Recently, Bessler, Warnatz, and Goodwin [104] have reported the modeling studies to address the behavior of various charge-transfer reaction pathways as a mechanism on the hydrogen oxidation kinetics of Ni/YSZ anodes. They have studied three different charge-transfer reaction pathways (oxygen spillover, hydrogen spillover, and interstitial hydrogen transfer) based on types of charge-transfer reactions, mentioned in Section 1.2.6. Their modeling studies and their comparison with experimental data suggest that the rate limiting step is charge-transfer during hydrogen spillover from Ni to a hydroxyl group on the electrolyte surface. They have revealed the challenges that a complete model is required to include the set of the surface diffusion parameters and the chemical reaction kinetics of the intermediates.

There have been few simulations of EIS data of SOFC systems. One example of modeling studies of impedance spectra on SOFC data has been reported by Zhu and Kee [105]. These authors have reviewed the modeling studies from Goodwin and Gauckler to adapt their results into EIS simulations. The authors have developed a model to analyze impedance spectra in anode supported SOFCs with internal reforming of methane. The parameters of gas phase diffusion, reforming chemistry of hydrocarbons, charge-transfer reaction, and ohmic ion transport have been included into their model. EIS simulations have been done on the circuit shown in Figure 1.7a by using kinetic and thermodynamic parameters for reforming chemistry of

hydrocarbons and porous-media transport i.e. gas phase diffusion. Their EIS simulations of various current densities on SOFC system are shown in Figure 1.7b. The EIS data have revealed that gas phase diffusion of fuels (H_2 and CH_4), reaction pathways, and individual reaction rates directly affected EIS spectra. Consequently, they have proposed that optimized EIS simulations were required for each individual SOFC systems.

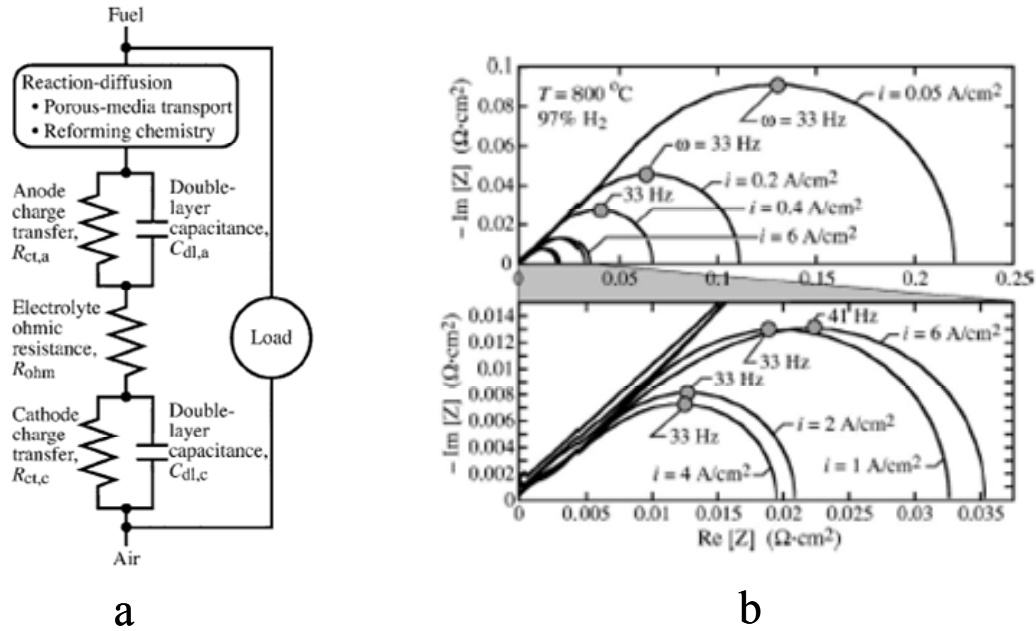


Figure 1.7 a) equivalent circuit for fitting EIS modeling studies, b) EIS simulations from modeling studies, from Zhu and Kee [105].

1.4. Scope of the thesis:

Analyses of the electrochemical oxidation kinetics of hydrogen and hydrocarbon fuels are presented in the following chapters. The performance of SOFC anodes with different materials and different experimental plan is examined by using electrochemical techniques, i.e. Linear Scan Voltammetry (LSV) and Electrochemical Impedance Spectroscopy (EIS).

The power and current densities of SOFC systems are 10-20 times lower than the contemporary SOFC systems due to thick electrolyte supported MEAs. The thickness of the YSZ electrolytes changes between 1.00 to 1.20 mm (0.020 to 0.030 mm in conventional SOFC systems). Thick electrolyte is preferred to eliminate anode transport and to minimize pre-electrochemical reactions in a support layer. The series of Ni/YSZ and Cu/CeO₂/YSZ anode systems are evaluated for the characterization of carbon deposits from butane fuel. The Au/YSZ systems are employed to examine the rate limiting step of the H₂ oxidation reaction on the SOFC anodes

A comprehensive review of hydrogen and hydrocarbon fuels used on SOFC anodes, and characterization of carbon deposits accumulating on SOFC anodes with hydrocarbon fuels is given in Chapter 2. The contribution of Au anodes and YSZ electrolyte materials on SOFC anode performance and on hydrogen oxidation reactions is discussed in Chapter 3. Also, the reactions at the interface between SOFC anodes and electrolytes are evaluated via different anode geometrical areas on SOFC electrolyte in Chapter 3. Chapter 4 discusses the hydrogen oxidation kinetics steps on the SOFC anode interface and surfaces by using different Au electrode thicknesses and different fuel composition to explore the effect of fuel partial pressure on SOFC anode performance. By using isotopically labeled D₂ fuel on SOFC anode the contribution of surface diffusion reaction on Au electrode performance is addressed by using experimental studies and computational modeling studies in Chapter 4. The summary and future remarks of thesis are given in Chapter 5 as a conclusion.

Chapter 2:

Formation of Carbon Deposits from Hydrocarbon Fuels in Solid Oxide Fuel Cells

2.1. Introduction

Solid oxide fuel cells (SOFCs) are of interest due to their high potential as stationary and portable power sources, and also due to their ability to use of hydrogen or hydrocarbons as fuels with high theoretical conversion efficiencies [3, 4, 7, 8]. SOFCs employ solid oxide electrolytes, that conduct O^{2-} ions but require high operation temperatures ($>500^{\circ}C$) [106, 107]. These high temperatures allow for the internal reforming of hydrocarbon fuels at the anode so that SOFCs can use natural gas, petroleum distillates, as well as renewable sources such as hydrogen, methanol, and ethanol.

SOFCs contain an electrocatalyst anode to oxidize the fuel, an electrocatalyst cathode to reduce oxygen, a conductive material to collect current, and an electrolyte (8 mole % yttria stabilized zirconia, YSZ, in this study). Many research groups have focused on Ni based SOFC anodes due to their low cost compared to other precious metals. Ni is a well-studied catalyst for the oxidation of hydrogen [89, 108-112]. However, Ni also catalyzes coke formation on the anode surface with hydrocarbon fuels, which inhibits cell performance and causes anode degradation [58, 113, 114]. Several research groups have considered different anode materials to avoid the coke formation, especially with higher hydrocarbons [86, 87, 115]. Cu/CeO₂/YSZ anodes have been investigated for the electrochemical oxidation of longer chain

hydrocarbons [58, 74, 116, 117]. Ceria (CeO_2) has been well established as a catalyst for methane oxidation and for hydrocarbon activation [118-121]. However, there is a distinction between Ni/YSZ and Cu/ CeO_2 /YSZ anodes. Gorte and co-workers [10, 11, 37, 39, 78, 113] have observed that Cu/ CeO_2 /YSZ anode cell performance with hydrogen fuel was enhanced by a factor of 2-3 after the formation of carbon deposits, which is in sharp contrast to Ni/YSZ behavior. It has been claimed that the reason of this enhancement was due the formation of “tar” that promotes the electrical conductivity of poorly conducting anode [10, 11, 37, 39, 78, 113].

The chemical and structural properties of these carbonaceous deposits needs to be described to address some of the questions about the carbon formation and its effects on SOFC's performance. There has been extensive research and many different approaches to this subject. Dean's research group [82] has examined the gas-phase reactions of higher hydrocarbons at high temperature range to address the effect of pyrolysis on the carbon formation. The analysis of butane pyrolysis products at the SOFC operating conditions (temperature range of 500-850 °C with the pressure of 0.8 atm and the residence time of butane 5 seconds without electrochemistry) has shown the gas phase composition (36.3 % methane, 39.8 % ethylene, 13.0 % propylene, less than a percent ethane and hydrogen, and the fraction of four and five carbon chains). Another approach from Gorte's group [78] has been the examination of exhaust species of SOFCs running with butane. Condensed speciation on the exhaust tube has been mainly defined as polyaromatic hydrocarbons (PAH) such as naphthalene, acenaphthalene, phenanthrene, anthracene, and pyrene. Barnett and his colleagues have used iso-octane [87] and propane [88] as fuel for SOFCs and they have tried to

avoid the tar formation by adding air to the fuel mixture. The catalytic formation of carbon deposits has been also studied by using different hydrocarbons on Ni metal. Toebe *et.al.* [122] has recently shown the effect of Ni particle size on the catalytic growth of carbon fibers by using CH₄, C₂H₄/H₂ mixture, or CO/H₂ mixture as a fuel system. Continuous carbon nanotubes could only be formed with small Ni particles (\leq 50 nm) in hydrocarbon atmosphere at 550 °C. Continuous supply of hydrocarbon fuel allows growing layers on carbon nanotubes, and then carbon nanotubes were called carbon fibers. There have been a number studies about single and multi wall carbon nanotubes (reviewed in Dai *et.al.* [123]), which were catalytically formed on different metals such as Ni, Fe, Co, Mo, and Ru.

Recently, Pomfret *et.al* [124] has reported that intermediates formed on Ni/YSZ anodes by using butane and CO as fuel had a graphitic nature. In situ Raman spectroscopy studies done in this work clearly showed that graphitic intermediates formed in first minute of hydrocarbon fuel exposure to Ni/YSZ anode systems. The chemical nature of these carbon deposits and/or tar on SOFC anodes operating with higher hydrocarbons was not fully defined, although these carbon intermediates were defined as graphitic.

This study focuses on the understanding of the structural and compositional characteristics of carbon deposits, which are produced on Ni/YSZ and Cu/CeO₂/YSZ anode surfaces of SOFCs using butane fuels. Polarization measurements of anodes were evaluated to observe the changes in power densities by using two different fuels such as hydrogen and butane consecutively on SOFC anodes. Power densities of the SOFC systems were correlated with carbon deposit formation with respect to time of

butane fuel flow to evaluate the effect of growth on SOFC performance. The effects of these carbon deposits on SOFC anode performance were explored to address the reason of the enhancement in SOFC power densities. The anode material dependence of these carbon deposits was investigated by employing Ni/YSZ and Cu/CeO₂/YSZ anodes in SOFC systems using butane fuel. The characterization of the carbon deposits on anode surfaces were studied by using X-ray Diffraction (XRD), Raman Spectroscopy, Scanning Electron Microscopy (SEM), and X-ray Photoelectron Spectroscopy (XPS). The chemical nature of carbon deposits forming on SOFC anodes is mostly in graphitic structure. Moreover, the combinations of disorders in the graphitic structure, edge carbon effect in the graphitic structure and morphology differences, such as spherical and filamentous, are the reason for the varieties of graphitic carbon deposits on anode materials. Besides spherical morphology of graphitic carbons with the finite grain size observed for both anode systems, filamentous carbon morphology was observed only on Ni/YSZ anode systems.

2.2. Experimental Section

The experimental setup for the SOFC assembly is shown in Figure 2.1. The single SOFC was attached to a ceramic tube by using ceramic paste. The entire assembly was placed to a furnace after preparation of SOFC assembly was completed. The preparation and operation details of SOFC assembly are explained below. Fuel flow was supplied to the anode by inlet tube, and the cathode was exposed to air by using another. The Membrane electrode assembly (MEA) for the single SOFC was prepared on a polycrystalline YSZ disk (8 mole % yttria stabilized zirconia disk) with a 25.4mm diameter and a 1.5mm thickness, which was fabricated from TOSOH Corp.

YSZ powders. YSZ powders were pressed with dye press and sintered at 1500°C for an hour.

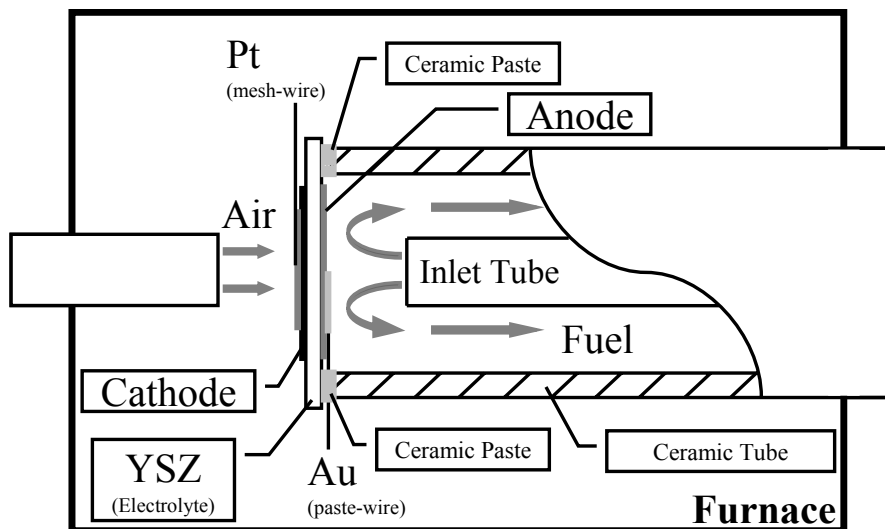


Figure 2.1: Schematic representation of SOFC experimental set up

2.2.1. Preparation of Cathode:

The porous LSM-YSZ cathode was prepared by using consecutive sintering of LSM-YSZ gel. First, 0.500 g LSM-YSZ powder (50% $\text{La}_{0.85}\text{Sr}_{0.15}\text{MnO}_3$ -50% YSZ, as purchased from NexTech Materials) and 0.0117 g KD-1 dispersant powder (Tape Casting warehouse, TCW) were ground in an amalgamator with a steel vial (2.54 cm length and 1cm diameter) with a steel cap and a rubber O-ring. The steel vial and its cap are tightly wrapped around and over the cap with Parafilm ® and then electrical tape to avoid leak. 0.2712 mL toluene solvent was added and the mixture was ground for 5 minutes. The mixture is cooled down on the bench for 15 minutes to decrease toluene evaporation. Lastly, 0.0325 mL Polyethylene Glycol plasticizer, PEG-600 (Aldrich), 0.0432 mL Dioctyl Phthalate 99% releasing agent (Aldrich), and 0.0265 g

Polyvinyl Butyral binder, PVB, (TCW) were added to the mixture and then it was ground for another 5 minutes. The mixture is again cooled down on the bench for 15 minutes to minimize the ingredient loss. The LSM-YSZ gel mixture was then coated onto the YSZ disk by using a masking tape (Kapton) to control the shape of cathode. The disk was heated at 0.3°C/min to 400°C, and fired for one hour. The sample was ramped to 1300°C at 1°C/min, sintered at 1300°C for an hour, and cooled to room temperature at 0.5°C/min. The resulting cathode was a smooth black layer on the YSZ disk.

2.2.2. Preparation of Anodes:

The Ni/YSZ anode: The NiO/YSZ paste (50% NiO-50% YSZ, Tech Materials) was applied to the cathode ready YSZ disk by using a masking tape (Kapton) to control the shape of anode, and then dried by using heat gun. The NiO was reduced *in-situ* in a 5 % H₂-95 % Ar mixture for 10 hours at 785 °C.

The YSZ anode: The porous YSZ layer (mixture of 60% YSZ powder from Aldrich-40% glycerin from Fisher Chemicals) where needed for the anode was painted on the opposite side of the cathode and then sintered 1 hour at 400°C and then 1 hour at 1300°C.

The Cu/CeO₂/YSZ anode: To prepare Cu/CeO₂/YSZ anode, 10% ceria and 5% copper, where needed, were impregnated into the porous YSZ layer by aqueous solutions of Ce(NO₃)₃·6H₂O and Cu(NO₃)₂·2.5H₂O. MEAs were then sintered at 800°C under reducing atmosphere.

2.2.3. Preparation of Cell Assembly:

Pt and Au wires were attached to cathodes and anodes by using Pt and Au paste, respectively. The MEA was then attached to a 30 cm length, 1.6 cm inside diameter, and 2.2 cm outside diameter alumina ceramic tube (AC Technologies) by using zirconia-based ceramic paste (see in Figure 1). The fuel inlet tube was a 30 cm length, 0.48cm inside diameter and 0.64cm outside diameter alumina ceramic tube (AC Technologies), which was sealed by a rubber stopper.

2.2.4. SOFC Operation Conditions:

The SOFC assembly was placed in a furnace and heated to 785°C at a rate of 1°C/min under Ar/H₂ flow. The diluent (Ar) / fuel (H₂ or butane) ratio was 2:1 with flow of 140 sccm to 70 sccm, respectively. The fuel flow adjustment regarding to H₂ and butane fuels was accomplished by using the number of electrons produced by total oxidation of these two fuels. As a result of the flow rate adjustments, the number of electrons per unit from these fuel flows was the same. Flow rates of fuel mixtures were controlled by using electronic mass flow controllers. A National Instruments SCXI data acquisition system was employed to control and record the electronic mass flow controller data. After measurements were done, the SOFC assembly was cooled to room temperature by the rate of 1°C/min under Ar.

2.2.5. Characterization Techniques:

Either An Autolab PGSTAT30 or Gamry Reference 600 with four potential channel applications at once was used for electrochemical measurements. SEM analyses were performed on an AMRAY 1820K Scanning Electron Microscope with an acceleration potential of 25kV. XRD data were recorded by using a Bruker C2 Discover X-Ray Powder Diffractometer with a CuK_α radiation and a HiStar area detector. In all samples, regions of the anode surfaces were selected randomly and three different spots for each anode system were analyzed and compared for reliability. Six frames were accumulated with an area detector and combined together to give 2-theta scan range from 4° to 90° . The MDI Jade software package was used to perform the unit cell indexing and refinements on the XRD results. Raman data were collected using a Renishaw In-Via Raman Microscope with 15mW power from an Ar^+ ion laser source (488 nm). Renishaw WIRE 2.0 software was used to calculate the integrated intensities from Raman Spectra.

XPS data were acquired by using a Kratos Axis 165 spectrometer at a base pressure of 4×10^{-10} Torr with a non-monochromatic MgK_α radiation. The X-ray power used for the measurements is 150W. All the measurements were done in hybrid mode using both electrostatic and magnetic lenses, with a step size of 0.1 eV and sweep time of 60 s. All individual region spectra were recorded in the FAT (Fixed Analyzer Transmission) mode with pass energy of 20 eV and an average of 10 scans. Data processing was done using Vision processing software. After subtraction of a linear background, all spectra were fitted using 60% Gaussian / 40% Lorentzian peaks, taking the minimum number of peaks consistent with the best fit. XPS measurements lead to calculate the relative atomic concentrations of the samples by utilizing peak

area and peak height sensitivity factors after inelastic background corrections were made.

2.3. Results and Discussions

2.3.1. Performance of SOFC anodes:

Porous Ni/YSZ and Cu/CeO₂/YSZ anode systems were employed to address the anode material effects on carbon deposits from butane fuel. As shown in Figure 2.2, a single circular anode was prepared for Ni/YSZ systems, whereas, two semi-circular anodes with and without Cu on an YSZ disk for Cu/CeO₂/YSZ systems were prepared.

These anode systems were evaluated to observe an enhancement in SOFC power densities by the consecutive fuel flow used in the order of H₂-butane-H₂ for a certain time for the butane fuel flows, which were 5 hours of butane fuel flow for Ni/YSZ anode systems and 5-100 hours for Cu/CeO₂/YSZ. These two different butane fuel flow times were chosen to explore the effect of more carbon deposits on the performance of Cu/CeO₂/YSZ anode systems.

Changes in maximum power densities of these anode systems with respect to the operation time are shown in Figure 2.2. Abrupt decrease in maximum power densities is observed for all three anodes when butane fuel is first introduced after H₂. This trend continues for an hour for each anode case, although current is being drawn on the anode systems. After four hours butane fuel flow was fed, maximum power densities are stable at certain values. This can be concluded that for the first hour of

butane exposure the maximum power densities of the anode decreases due to carbon deposit forming, and then the anode systems are saturated with carbon deposits after one hour, and enhance the performance by 30 %.

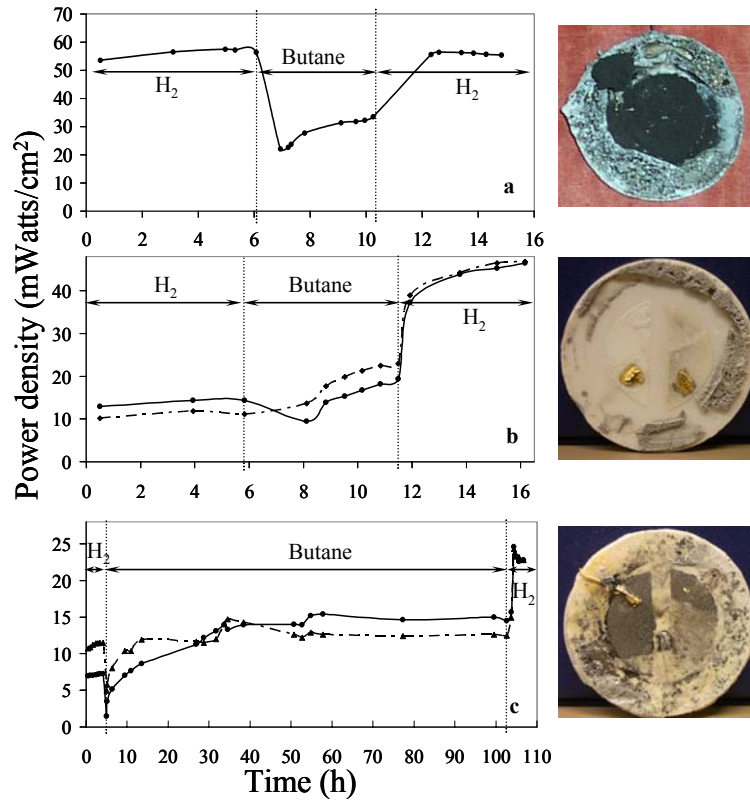


Figure 2.2: The SOFC power density vs. time plots for H₂-Butane-H₂ cycle representing a) on Ni/YSZ b) 5 hours, and c) 100 hours of butane on Cu/CeO₂/YSZ anode systems (—CeO₂/YSZ, and --- Cu/CeO₂/YSZ anodes) Pictures of anode systems after SOFC operations are respectively shown next to the power density curves of anode systems

As shown Figure 2.2a-b, the conditioning time with butane fuel flow was the same for Ni/YSZ and Cu/CeO₂/YSZ anode systems. Butane fuel flow was fed for 5 hours to both anode systems at 785°C, and then the fuel was switched to H₂ to observe the change in maximum power densities with respect to previous H₂ fuel. The maximum power density of Ni/YSZ anode with H₂ fuel is not affected after butane fuel flow is introduced for 5 hours. On the other hand, for Cu/CeO₂/YSZ anode systems there is

an increase in maximum power densities by a factor of approximately 3 with respect to initial H₂ fuel power density values. Ni content in Ni/YSZ anodes is 50 % by weight, whereas Cu and CeO₂ loadings are 5 and 10 % respectively. The enhancement in Cu/CeO₂/YSZ anode systems hydrogen fuel is due to conductivity difference of anode systems before and after carbon deposition. Therefore, 5 % Cu loading by weight is insufficient for anode conductivity, which is supplied by carbon deposits after butane fuel flow.

In Figure 2.2b, Cu/CeO₂/YSZ anode has ~25 % more performance than CeO₂/YSZ anode for first 5 hours of butane fuel flow. Because, addition of 5 % Cu increases the anode electronic conductivity and Cu/CeO₂/YSZ anode provides higher power densities with butane fuel flow. However, CeO₂/YSZ and Cu/CeO₂/YSZ anodes follow the identical enhancement trend for H₂ fuel. The addition of 5 % Cu to anode systems has no effect on H₂ fuel performance. Since carbon deposits enhance the anode conductivity with H₂ fuel, after carbon deposition shown in Figure 2.2b-c, the effect of Cu doping on Cu/CeO₂/YSZ conductivity is surpassed.

As shown Figure 2.2 b-c, the identical enhancement trend observed between 5 hours and 100 hours of butane fuel flow times reveals that the longer butane fuel flow time has the same effect as the shorter time butane exposure on the power densities CeO₂/YSZ and CeO₂/Cu/YSZ anodes. However, the anode surface is completely covered with carbon deposits for 100 hours of butane fuel flow times in Figure 2.2c. The completion of carbon deposit from short or long time butane flow on the anode surfaces is proposed as the reason for the identical enhancement between 5 hours and 100 hours of butane fuel flow times.

2.3.2 SEM images of SOFC anode surfaces:

SEM images of carbon deposits on the anode surface and carbon deposits isolated from YSZ disk surface are shown in Figure 2.3. These carbon deposit spheres have diameters of approximately 5 μ m and the thickness of carbon deposit film isolated from YSZ disk surface is also 5 μ m. These carbon deposits have no fibrous character according to these SEM images.

SEM images of identical carbon spheres have been reported in literature [125, 126]. The structural growth model for this kind of spherical carbon has been suggested by first Franklin [127] and later developed by Dresselhaus [128]. In their model, layered planes of small graphitic crystallites were joined together by cross links, and then the crystallite growth resulted from movement of layers rather than individual carbon atoms. After these graphitic crystallites formed, the spherical carbon deposits were self-organized by movement of graphitic crystallites. This model can also be applied in the growth of spherical carbons on SOFC anodes. Therefore, small crystallites of graphene layers produced on the SOFC anode surfaces organized to form carbon spheres with the size of 5 μ m, which fuse to form 5 μ m carbon films shown in Figure 2.3.

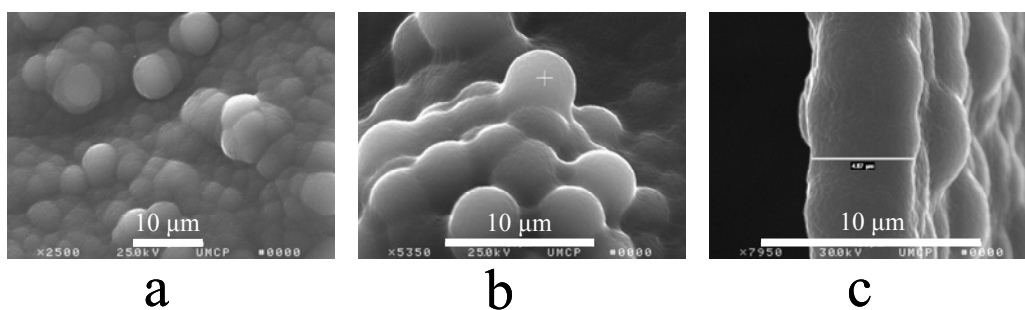


Figure 2.3: SEM images of a) Carbon deposits on Cu/CeO₂/YSZ anode surface b) enlargement of sample (a), c) the carbon film on YSZ disk.

SEM images of carbon deposits on Ni/YSZ anode surfaces are shown in Figure 2.4. Both spherical and filamentous carbon deposits were observed on Ni/YSZ anode surfaces. Spherical carbon deposits, which are dominant morphology, have roughly 1 μm diameters in Figure 2.4a and are very similar to those described above. Filamentous carbon deposits, which were observed different places on Ni/YSZ surfaces, have 1-2 μm diameter in Figure 2.4b. The filamentous carbon deposits are randomly spread on Ni/YSZ anode surfaces. The calculation of the ratio between spherical and filamentous carbon deposits is difficult to address by using SEM images.

Ni metal itself is well known for catalyzing the formation of multi-wall carbon nanotubes from various hydrocarbons [123]. Multi-wall carbon nanotubes with number of walls ≥ 10 are called filamentous or fibrous carbon [123]. As explained previously, spherical carbon deposits are found both on Cu/CeO₂/YSZ anode and on YSZ electrolyte surfaces. Therefore, the combination of spherical and filamentous carbon morphologies is anticipated for Ni/YSZ anode systems. SEM images of

carbon deposits in Figure 2.4 confirm both morphologies formed on Ni/YSZ anode systems.

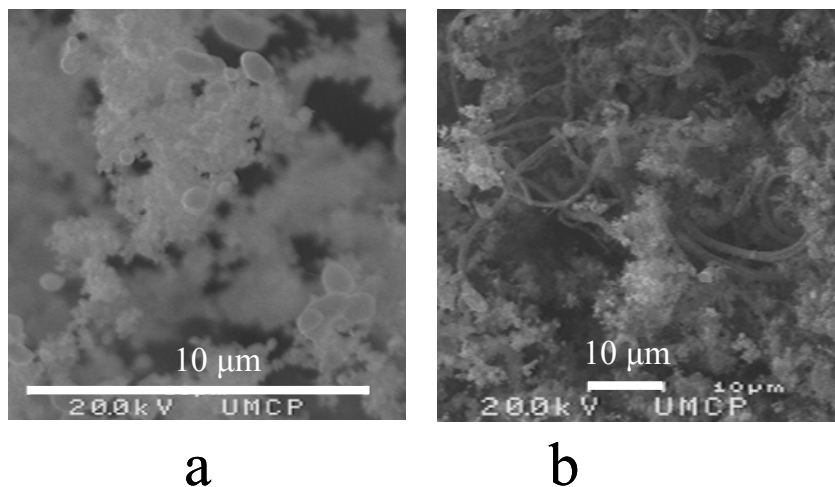


Figure 2.4: SEM pictures of a) spherical carbon deposits b) the combination of spherical and filamentous carbon deposits on Ni/YSZ anode surfaces.

2.3.3 XRD analysis of SOFC anode surfaces:

X-Ray diffraction patterns in Figure 2.5 show that the carbon deposits formed on Ni/YSZ and Cu/CeO₂/ YSZ anode surfaces have graphitic crystal structures with smaller domain grain sizes, L_a , and smaller thicknesses, L_c than those of the single crystal graphite structure. Graphite has the unique hexagonal crystal structure (Figure 2.5 inset) composed of graphene (6-membered sp^2 C rings) layers. The (002) reflection is the most intense XRD peak for graphite at 26.5° . XRD patterns of the carbon deposits isolated from the electrolyte and anode surfaces as well as 325-mesh graphite standard with an average particle size of 44µm are illustrated in Figure 2.5. The 325-mesh graphite XRD profile is shown as a standard to compare to the rest of the samples. The sharp graphite (002) reflection is observed 26.5° ($d_{002}=3.361 \text{ \AA}$). The Ni/YSZ anode sample in Figure 5b has the most intense diffraction peak at 26.4°

($d_{002}=3.376 \text{ \AA}$) as compared to 325-mesh graphite sample, and all of the other carbon deposit samples on Cu/CeO₂/YSZ anodes have one broad peak shifted to lower angle. This common broad peak suggests that both 5 hours and 100 hours of butane exposure to the SOFC anode produce graphitic carbon deposits. The peak positions of 5 and 100 hours butane fuel flow samples are 25.3 ° and 25.4°, respectively. The d-spacing difference of carbon deposit crystals on Cu/CeO₂/YSZ anode systems with different butane fuel flow times are approximately 0.015 Å. The isolated carbon film from YSZ electrolyte film between two semi-circle anodes has a peak at 25.8 ° ($d_{002}=3.460 \text{ \AA}$)

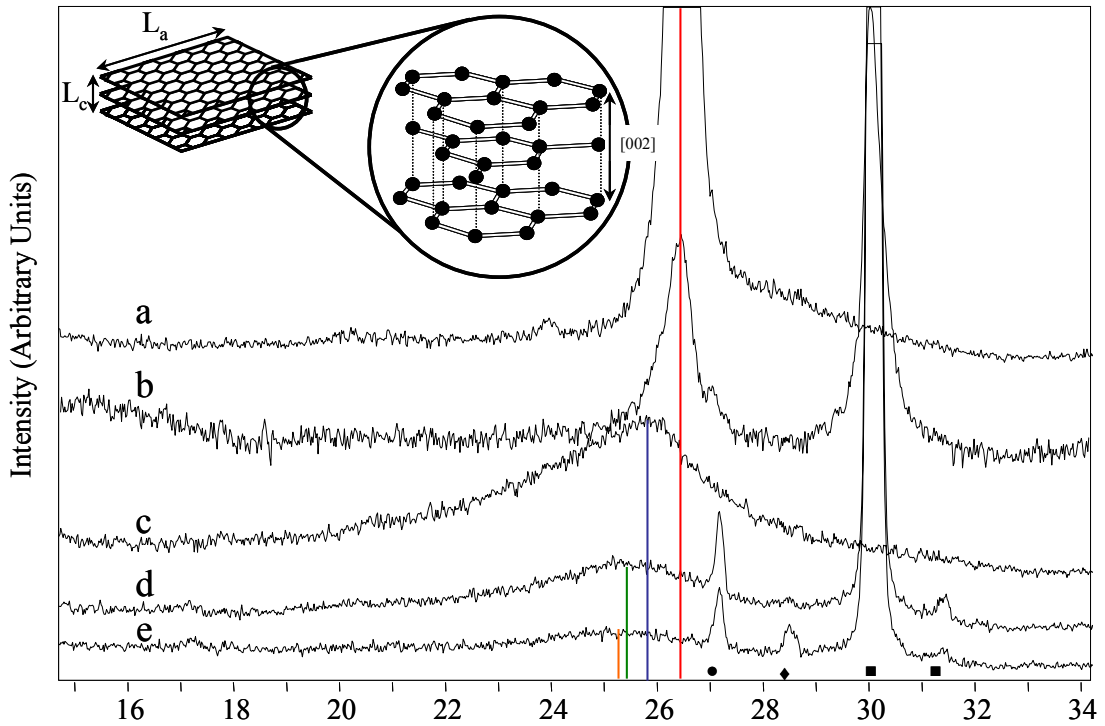


Figure 2.5: XRD Patterns of a) 325-mesh graphite, b) Ni/YSZ surface exposed to butane for 5 hours, c) carbon deposit isolated from CeO₂/YSZ anode surface exposed to butane for 5 hours, d) CeO₂/YSZ surface exposed to butane for 100 hours, e) CeO₂/YSZ surface exposed to butane for 5 hours (●: SiO₂ from ceramic paste, ■: YSZ, ♦: CeO₂) Inset: Graphite crystal structure.

The shift to a lower angle and broadening of the (002) peak has been observed in many studies of graphite [129-131] and is attributed to the thickness (L_c) and the domain size (L_a) of the graphene layers (Figure 2.5 inset). As L_c decreases, the d-spacing between graphene layers increases, which causes the shift of (002) peak to lower angle (2-Theta) with respect to the standard graphite (002) peak. The fluctuation in d-spacing causes the broadening and the shift [129, 130, 132, 133]. When the grain size, L_a , becomes smaller (in nanometer scale), the possibility of diffraction diminishes, thus the intensity of the peak also decreases. According to XRD analysis of carbon deposits from different anode surfaces show that the carbon deposits on Ni\YSZ anode have the closest structure to bulk graphite with respect to d-spacing values, L_c values. It is concluded that L_c values of carbon deposits on SOFC anode surfaces depend on materials used on SOFC anodes. Quantitative analysis of the grain size, L_a , will be extensively discussed in the Raman section.

2.3.4. Raman studies of SOFC anode surfaces:

The three different assemblies of SOFC mentioned above were evaluated by using Raman spectroscopy. Raman spectra of disordered graphite type materials [132-139] show two modes; the G (graphite) peak at 1570-1600 cm^{-1} and the D (disorder) peak at 1300-1350 cm^{-1} . The G band, fully allowed, has E_{2g} symmetry (Figure 2.6 inset) and is involved in the plane stretching motion of pairs of sp^2 C atoms. The D band has A_{1g} symmetry (Figure 2.6 inset) and is forbidden for infinite graphene layers but develops a strong Raman activity when the continuity of graphene layers is broken. This is caused by small grain sizes, structural disorders, and sp^3 C atoms [135-138].

The D band results from the 6-membered ring of sp^2 C atoms, out of graphene layers. The network of sp^3 C atoms, “diamond-like” [135], has an active Raman band with T_{2g} symmetry centered at 1332 cm^{-1} , which is in the same range of graphite G and D band.

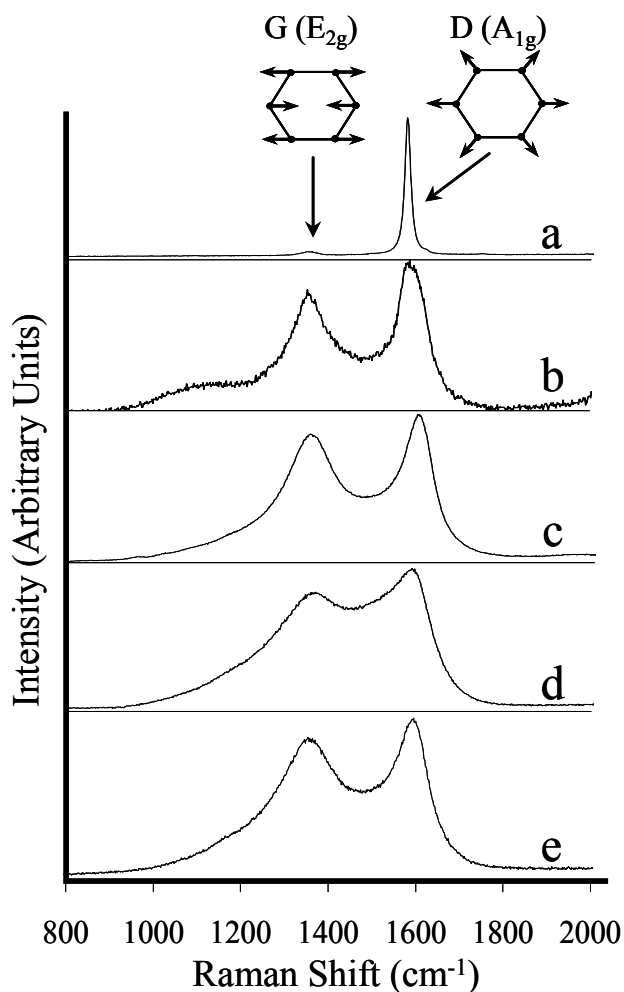


Figure 2.6: Raman Spectra of a) 325-mesh graphite, b) Ni/YSZ anode (5 hours butane exposed), c) CeO_2/YSZ (5 hours butane exposed), d) CeO_2/YSZ (100 hours butane exposed), e) $\text{Cu}/\text{CeO}_2/\text{YSZ}$ (100 hours butane exposed). Inset: Atomic motions of carbons and their symmetries in graphitic structure.

The G and D Raman peaks of the carbon deposits from the SOFC anode surfaces are shown in Figure 2.6. The shift to higher energy in the G peak shows that graphite with a small average crystallite size ($\leq 20\text{ nm}$ [135]) exists in our samples. The

decrease in crystallite size, L_a , causes the new sets of vibrational density of states in the graphene layers, therefore the G peak shifts to higher wave numbers in the Raman spectrum. The G and D peak broadening is also attributed to small L_a . When L_a decreases, carbons on edges [134-138] will increase in relative concentration and will be more disordered between crystallites. Therefore, the atomic environments of the crystallites will be different and the G and D peaks will be broader. These observations clearly show that nanocrystalline graphite is produced on the SOFC anode surfaces.

The intensity ratio of the D and G peaks, $I(D)/I(G)$ is inversely proportional to L_a and can be used to calculate the in-plane graphitic domain size, L_a . This relationship was first shown by Tuinstra and Koenig [140, 141]. Later, Knight and White [142] have shown that there is an empirical expression which explains the dependence of $I(D)/I(G)$ ratio on L_a . Also, the excitation laser energy dependence of the $I(D)/I(G)$ ratio has been extensively studied by many different groups. Lately, Cançado *et al* [143] derived an empirical formula revealing the excitation laser energy dependence on $I(D)/I(G)$ (integrated peak areas) ratio, where L_a is defined by the following equation:

$$L_a(\text{nm}) = (2.4 \times 10^{-10}) \lambda_l^4 (\text{nm}) (I(D)/I(G))^{-1}, \quad (2.1)$$

in which λ_l is the excitation laser wavelength in nanometers (nm). They showed that at any given excitation laser energy, the crystallite size, L_a , can be calculated by using Raman integrated intensity ratio of D and G peaks. In our study, calculated L_a values

for different anode surfaces were confirmed by using Raman experiments with different types of the excitation laser energy, i.e. 488nm, 514.5nm, and 633nm. Since, the Ar⁺ ion laser ($\lambda=488\text{nm}$) is readily available, only the 488nm excitation laser energy Raman data were used in this report.

Using equation 2.1, L_a of nanocrystalline graphite on SOFC anode surfaces was estimated to be from 4 to 12nm as listed in Table 2.1. L_a of nanocrystalline graphite is almost 12nm for Ni/YSZ systems and 4-6nm for Cu/CeO₂/YSZ systems after either 5 or 100 hours of butane is supplied to the anode. As mentioned on XRD section, Raman data and XRD studies clearly show the chemical nature, L_a , of carbon deposits varies with materials used in SOFC anodes.

Table 2.1: Raman Data of SOFC anode surfaces

SOFC anode materials	D peak (cm ⁻¹)	G peak (cm ⁻¹)	I(D)/I(G)	L_a (nm)
Ni/YSZ(5 h butane)	1355	1588	1.2	11.7 ± 0.4
CeO ₂ /YSZ(5 h butane)	1372	1596	2.2	6.1 ± 0.2
CeO ₂ /YSZ(100 h butane)	1386	1586	3.3	4.1 ± 0.1
Cu/CeO ₂ /YSZ(100 h butane)	1384	1596	3.5	4.9 ± 0.1

2.3.5. XPS studies of SOFC anode surfaces:

Carbon deposits from SOFC anode surfaces and the 325-mesh graphite reference were analyzed by XPS in Figure 2.7. Spectra shown in Figure 2.7 show the detailed C1s binding energy region of the 325-mesh graphite and that of representative carbon deposits from anode surfaces. Similar fitting features and carbon atomic ratios from different anode surfaces and 325-mesh graphite standard suggest the same type of

carbon exists in all samples. A detailed examination of the C1s region of these carbon deposits on SOFC anode contains a number of overlapping features associated with different functionalities. The typical C1s region spectra (after linear inelastic scattering background subtraction) are shown in Figure 2.7 demonstrating how the C1s regions can be fitted to a number of component peaks. To remove the surface impurities, samples are etched by argon ion etching. Typically, this process cleans the surface uniformly with no implantation or compound decomposition, so that a depth profile can be obtained from the surface sample.

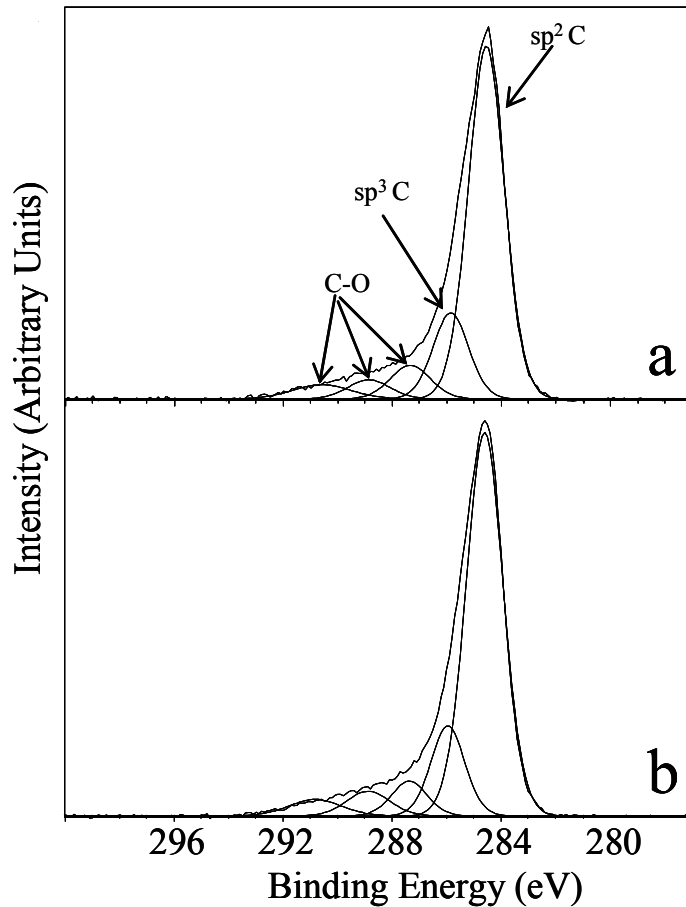


Figure 2.7: C1s region of X-ray photoelectron spectrum of a) 325-mesh graphite, b) typical SOFC anode surface.

XPS has been widely used for surface analysis of the carbon deposits [144-146]. The C1s binding energy of respective chemical states is employed to distinguish the carbon atoms with different hybridizations. Differences in the core region spectra provide substantial chemical information because the C1s region exhibits significant shifts with change in oxidation states [146] and hybridization [145]. These shifts can be accurately measured in the carbon deposits to differentiate carbon atoms with different environments [147, 148].

The lowest binding energy peak at 284.3-284.6 eV is assigned to the sp^2 hybridized (graphitic) carbon atoms and is in agreement with binding energies reported for single crystal graphite [144-150]. The second lowest binding energy peak at 285.1-285.6 eV is attributed to the sp^3 hybridized carbon atoms, which has also been reported elsewhere [144-150]. Therefore, there are many edge carbons binding to graphene layers and graphite crystallites. These sp^3 hybridized edge carbons can bind to carbon, hydrogen, and oxygen atoms.

The higher binding energy peaks are consecutively assigned with respect to their chemical environments [145, 147, 148, 151, 152]. The C-OH carbon shows a peak at 286.1 eV. The C-O-C carbon has a peak at 286.3 eV. The C=O carbon causes a peak at 287.4 eV. The O-C=O type carbon has a peak at 288.8 eV. Beyond this binding energy value, the π - π^* interactions tend to give the carbon shake-up peaks that overlap with the binding energy of sp^3 hybridized carbon atoms at higher oxidation states. The range of 288-289 eV and upper binding energy peaks become indistinguishable from each other.

As shown in Table 2.2, plasma etching removes oxygen from the surface of carbon deposits. After etching, the total oxygen % of each sample decreases to less than 5 %. This amount is a negligible amount for oxygen concentration in XPS studies and the total carbon content approaches 100 %. This analysis reveals that the carbon deposits consist of only carbon. The SOFC anode surface carbon and oxygen concentrations are similar to that of the 325-mesh graphite. These similarities in XPS analysis between 325-mesh graphite and the SOFC carbon deposits suggest that both have the same type of graphitic structure. The sp^2/sp^3 ratio of carbon materials gives information about the ordering level of graphene layers in the sample [145, 147-150]. Based on the sp^2/sp^3 ratio from XPS data, the SOFC carbon deposits have the same relative ordering level of graphene layers with respect to the 325-mesh graphite sample.

Table 2.2: C and O atomic percentages from XPS Spectra

		Total C %	Total O %	sp^2 C %	sp^3 C %	C-O %	sp^2/sp^3 C
325-mesh Graphite	Before Etching	96.42	3.57	61.58	12.77	25.65	4.8
	After Etching	97.07	3.03	65.95	14.05	20.00	4.7
Ni/YSZ (5 h Butane)	No Etching	98.38	1.62	69.30	13.96	16.74	5.0
CeO₂/YSZ (100 h Butane)	Before Etching	78.58	21.41	59.40	16.19	24.41	3.6
	After Etching	95.62	4.38	67.93	14.82	17.26	4.6
Cu/CeO₂/YSZ (100 h Butane)	Before Etching	82.33	17.66	50.82	25.24	23.94	2.0
	After Etching	98.20	2.80	66.98	15.04	17.98	4.5

2.4. Conclusions

The carbon deposits forming on Ni/YSZ and Cu/CeO₂/YSZ anode systems in SOFC with butane fuel were investigated in this study. The structural characterization and chemical composition analysis of the carbon deposits on the SOFC anode surfaces show that graphitic carbon is formed from butane fuel with an average grain size of 4 to 12 nm. All analytical techniques employed in this study agree that the nano graphitic carbon deposits are formed on SOFC anode surfaces.

The SOFC anode material dependence of carbon deposits is evaluated by using Ni/YSZ and Cu/CeO₂/YSZ anode systems in SOFC feeding with butane fuel. These carbon deposits are likely to be generated by poor electrocatalysis of hydrocarbon fuels. In both anode systems, the nanocrystalline graphite with spherical morphology is observed, the formation mechanism of which has been well studied elsewhere [86, 87, 122, 123]. However, the filamentous carbon morphology is only formed on Ni/YSZ anode surfaces. The calculated average crystallite size, L_a , of carbon deposits formed on anode surfaces is compared by using Raman data. The carbon deposits on Ni/YSZ anode surface have the largest L_a value, 11.7 nm, and the carbon deposits on Cu/CeO₂/YSZ anodes have the L_a range in 4-6.1 nm. The disorder in the graphitic crystal structure, sp^3 hybridized carbon atoms causes this close range of average crystallite size of graphitic carbon deposits. The reason of the difference in L_a range of carbon deposits from anode surfaces is caused by the morphology of filamentous carbon formed on Ni/YSZ anode surfaces. Consequently, the combinations of three

parameters, such as disorder in the crystal structure, sp^3 carbon atoms, and morphology of carbon deposits, are three significant factors that affect the carbon deposit characteristic.

XRD pattern (Figure 2.5) of anode surfaces coated with carbon deposits and isolated carbon deposit film show that the increase in the amount of carbon deposits results the superior order level, which is observed by the intensity and the shift of graphitic peak. The spherical and filamentous carbons on Ni/YSZ have higher L_a and L_c values and the diffraction peak of nanocrystalline graphite on Ni/YSZ anode is closer to that of graphite. The formation of filamentous carbon is observed only on the Ni/YSZ anodes due to Ni particles providing nucleation sites for the formation of filamentous morphology. However, spherical carbon morphology is observed not only on Ni/YSZ but also on Cu/CeO₂/YSZ, CeO₂/YSZ, and YSZ electrolyte surfaces because none of these components in Cu/CeO₂/YSZ anode systems catalyzes the formation of filamentous carbon morphology. The role of each anode components is proposed as YSZ, source for O²⁻ ions and catalyst for fuel oxidation when reduced; Cu, supplying conductivity on Cu/CeO₂/YSZ anodes; CeO₂, the catalyst for fuel oxidation; Ni, the catalyst for fuel oxidation and supplying conductivity Ni/YSZ.

These results are consistent with other reports [10, 11, 37, 39, 78, 113]. Nanocrystalline graphite formation gives short term enhancement in conductivity and performance with poorly conductive anodes such as Cu/CeO₂/YSZ anode systems but not with Ni/YSZ anode systems. The enhancement Cu/CeO₂/YSZ anode performance is not dependent upon a longer feeding of butane fuel flow such as 100 hours of butane, because graphitic carbon deposits saturate the anode surface less than an hour.

These findings suggest that the nanocrystalline graphite formation likely contributes to anode conductivity, which was previously believed to be provided by “tar” formation [10]. It is proposed that these carbon deposits are likely to help the catalytic H₂ fuel oxidation on Cu/CeO₂/YSZ anodes.

These results may help to address some of questions about the oxidation mechanism of longer hydrocarbons at SOFC operating conditions. Future studies on the nanocrystalline graphite formation on various SOFC anode surfaces may provide a basis for understanding the mechanism of direct electrochemical oxidation of hydrocarbons in a SOFC.

Chapter 3:

Analysis of different Au anodes with different geometry and different Porous YSZ layers in SOFC assembly

3.1. Introduction

In Solid Oxide Fuel Cell (SOFC) systems, Ni is the anode electrocatalyst most studied due to its low cost and high catalytic activity [35-37]. Specifically a Ni/YSZ cermet is the standard electrochemical anode system in SOFCs. Metallic Ni anodes with different microstructures, such as porous Ni paste, Ni gauze anodes, and dense Ni patterns, are extensively studied as both anodes and current collectors [33, 110]. Experimental studies generally agree that two main processes limit Ni based anode performance: (i) the activation of H₂, including charge transfer reactions and (ii) the desorption of H₂O from the Triple Phase Boundary (TPB), where the fuel gas phase, the electrochemical catalyst, and the electrolyte meet [16, 33, 35, 36, 110].

Ni/YSZ anode can be chemically modified by the possible formation of NiO at the interface between electrolyte and Ni, which affects the long-term stability of these systems [35, 116]. In this respect, the stability and contribution of current collection on SOFC performance become more significant. Thus, determining the impact of current collection on SOFC performance is an understudied feature for the fuel oxidation kinetics in SOFC anodes.

The distinction between the current collection and the electrochemical catalysis on SOFC electrodes is under discussion for a long time. This distinction is applicable to both anodes and the cathodes. Jiang *et al.* [95] has examined the relationship between

current collection and cathode performance on SOFCs by varying contact areas on the cathode material. It is acclaimed that increases in cathode-current collector contact reduced the cell resistance and the polarization losses to give better SOFC performance [95].

Au is commonly employed as a current collector on SOFC electrodes or as the interconnect between SOFC electrodes and measurement devices due to its low chemical activity [103, 154]. Molecular hydrogen, H_2 , is also of particular interest due its potential to be a fuel or an energy carrier gas for future energy conversion devices, such as fuel cells [8, 13, 68]. Therefore, understanding how H_2 interacts and behaves with Au anodes on YSZ electrolytes is important for understanding SOFC systems.

Traditionally, less reactive metals, such as Ag and Au, are chosen as the current collector or interconnect in SOFC systems. However, these materials, especially Au, are used also as the anode material [155]. Several experimental and computational studies are designed to address questions about H_2 oxidation kinetics in the SOFC with different anodes. For example, Kek and colleagues [102, 103] have investigated the performance of Ni, Pt, Ag, and Au as contact anodes on SOFC assembly with H_2 fuel. It is reported in these studies that Ni is the best anode material over others. Although the performances of Pt, Ag, and Au were close, the order was $Pt > Ag > Au$. The reason of this order is explained to be the catalytic activity for the dissociative adsorption of H_2 and the spillover of oxide and hydroxide ions on the metal surface. Hirabayashi *et. al.* [155] fabricated “anode free” SOFCs and showed that only Au as anode material on top of the SOFC electrolyte (120 μm thick)

material supplied a power density of 0.24 Watts/cm² at 950 °C and 0.14 Watts/cm² at 800 °C. These power densities are comparable to Ni/YSZ anode systems supplying that of 0.5-0.9 Watts/cm² with the same SOFC dimensions at this temperature range. The reason of this performance without an anode material is proposed due to the partial reduction of electrolyte surface. Pomfret *et al.* [156] has studied the effect of SOFC conditions on the reduction of YSZ surface. The depth profile studies of reduced YSZ layer propose that the thickness of reduced YSZ layer is 1-5 nanometers. If there is a current collector such as Au, the reduced YSZ electrolyte layer could be considered as an electrocatalyst and affect the SOFC performance. Since Au is a current collector, and YSZ is a conventional electrolyte on SOFC anodes, it is imperative to understand the contribution of both Au and YSZ toward SOFC anode performance. The roles of both the possibly reduced YSZ surface and the Au electrode in H₂ oxidation under SOFC conditions have not been completely clarified in the literature.

Fleig and co-workers [91, 93] have addressed the relationship between cathode architecture and oxygen reduction reaction kinetics on SOFC cathodes. In particular, they studied the importance of cathode-electrolyte contact area and cathode thickness (channel depth) in SOFC performance. A dense layer of LSM-YSZ was used as a SOFC cathode material in these studies. Since α -Al₂O₃ is not ionically conductive for O²⁻ ions [157], a dense sub-layer of α -Al₂O₃ blocking between LSM-YSZ cathode and YSZ electrolyte was employed to modulate the cathode-electrolyte contact area [91]. These experiments were designed to elucidate the oxygen reduction pathway for SOFC cathodes. The results revealed that O₂ reduction proceeds via the bulk of the

LSM-YSZ, and dictates the SOFC performance. They have also shown that the rate-limiting step for oxygen reduction on SOFC cathodes is the diffusion of oxide ions through the bulk of LSM-YSZ cathode.

Computational studies of H_2 oxidation on SOFC anodes have shown that O^{2-} ions directly participated in charge-transfer reactions [104]. These results inspired the use of O^{2-} ions occupying and blocking the interface area between porous Au and the YSZ electrode in this study. To address the effect of O^{2-} ions in SOFC anode performance in this study, porous Au anodes with different $\alpha\text{-Al}_2\text{O}_3$ blocking areas were designed in order to show where O^{2-} ions react with adsorbed species within SOFC anodes.

The determination of the rate limiting step in H_2 oxidation is the key to improvement of SOFC performance for applications with H_2 . The fundamental steps in H_2 oxidation, which were explained in Chapter 1, are the gas phase diffusion, the dissociative adsorption reaction of H_2 on active metal sites, the surface diffusion of H_2 or adsorbed species on anode surface, the charge-transfer reactions, and the desorption of H_2O from the interface between active metal anode surfaces and electrolyte. The gas phase diffusion of H_2 mainly depends on the porosity, tortuosity, and the thickness of anodes. In conventional porous anode architectures, the metallic electrocatalyst surface is presumed to catalyze the dissociative adsorption of H_2 . The surface diffusion of adsorbed species on the active metal catalyst is proposed to be the rate limiting process in transporting fuel to the interface, where the charge transfer reaction takes place [158, 159]. Desorption of H_2O from the electrolyte interface may

play a role because the concentration of H_2O in the interface affects the charge transfer reaction [160-163].

In this study, SOFC assemblies using porous and dense Au electrodes with different geometrical electrode areas and porous YSZ layers were employed to address questions about the rate limiting steps in H_2 oxidation reaction kinetics. Three or four different electrodes on an YSZ electrolyte disk are evaluated simultaneously for given experiments in this study due to the complexity of repeating the same set of material conditions due to high temperature sintering processes even between two consecutive SOFC experiments and the necessity of examining the effect of change in one parameter for each experiment. SOFC performances and SOFC resistance analysis were completed by using Linear Scan Voltammetry (LSV) and Electrochemical Impedance Spectroscopy (EIS) respectively. Scanning Electron Microscopy (SEM) pictures were used to structurally characterize the porosity of electrodes. Porous Au paste and dense Au film anodes were used as anode materials to identify the role of gas phase diffusion thorough Au electrodes. The different Au-YSZ interface area experiments were designed to address the questions about H_2 oxidation reaction steps at the interface, such as surface diffusion, charge-transfer, and desorption of water. To specify the contribution of YSZ to overall SOFC anode performance, layers of porous YSZ were prepared and applied on top of Au electrodes. Lastly, to block the transport of O^{2-} ions to the SOFC anode, dense $\alpha\text{-Al}_2\text{O}_3$ squares with different sub-interface areas were placed under porous Au anodes with the corresponding geometric area. By blocking O^{2-} ions it was aimed to evaluate the effect of O^{2-} ion movement on SOFC anode performance.

3.2. Experimental Section

The experimental setup and operating conditions of SOFC were explained in Figure 2.1 of Chapter 2. Briefly, the membrane electrode assembly (MEA) for the SOFC was prepared on a polycrystalline YSZ disk (8 mole % yttria stabilized zirconia disk) with a 25.4 mm diameter and a 1.10-1.20 mm thickness. The YSZ disk itself was prepared in the laboratory by dye pressing and sintering at 1500°C for an hour. LSM-YSZ was the cathode material, was prepared as a viscous solution, and applied by using a mask. The cathode was sintered by heating to 400 °C with the rate of 0.3 °C/min, holding at 400 °C for an hour, heating to 1300 °C with the rate of 1 °C/min, and sintering at 1300 °C for an hour. The supported cathode was cooled down to room temperature with the rate of 1 °C/min). Measurements in this study were conducted at 785 ± 10 °C.

3.2.1 Preparation of porous Au paste anodes:

Viscous Au paste (Engelhard) was applied to prepare porous Au anodes by using masking tapes. Four Au anodes with the specific Au-YSZ interface areas (i.e. 8, 16, 24 and 32 mm²) with known thickness were fabricated by using Kapton tape as a masking tape. Kapton tape masks were carved by hand and applied to the surface of a “cathode ready” YSZ electrolyte disk (see Chapter 2). Au paste was applied to the masked YSZ disk and the mask was subsequently removed. The disk and Au patches were dried for 2 hours by using a heat gun. Au wires (0.25mm and 99.99% pure,

AlfaAesar) were attached to each pattern by using small amount of Au paste. Subsequently, the whole assembly was glued to a ceramic tube by using ceramic paste and further sintered overnight at SOFC working conditions, i.e. at 785°C and under Ar-H₂ flow.

3.2.2 Preparation of Dense Au Film anodes:

To prepare dense Au film anodes, a similar Kapton tape mask with a pattern of four 5x5 mm squares was prepared and applied to a cathode ready YSZ disk. Then, a dense 1 µm Au layer was deposited via thermal evaporation to the YSZ disk with the pattern mask. The mask was then removed and the 5x5 mm Au squares were wired by Au leads.

3.2.3 Preparation of Porous YSZ layer:

To prepare porous YSZ layer, the mixture of nano-powdered YSZ with a particle size of 80-90 nm (from Aldrich), and glycerol (from Fisher Scientific) were mixed with the ratio of 60% YSZ to 40% glycerol by weight to get a viscous mixture. Stoichiometric amounts of each were weighed in the same plastic vial with a plastic ball, and then the mixture was ground by using an amalgamator for 10 minutes to give a paste-like viscous solution. This paste was deposited on electrolyte disk in patterned arrays by using a Kapton tape masks. The paste was subsequently dried by using heat gun for two hours and the assembly was *in-situ* sintered overnight at 785 °C under 5 % H₂-95 % Ar atmosphere.

3.2.4 Preparation of Porous Au anodes with α -Al₂O₃ Blocking:

Patterned α -Al₂O₃ blocking layers were deposited on the YSZ disks by way of e-beam deposition and Kapton tape masks to give 100 nm thick features. Then, the masks were removed and Au anodes were applied on top of α -Al₂O₃ patches.

3.2.5. Characterization Techniques:

A Gamry Instruments four-channel Frequency Response Analyzer (FRA) was employed for the performance measurements and for electrochemical impedance spectroscopy in potentiostatic mode at open circuit over a frequency range from 100 kHz down to 50 mHz. For the impedance measurements, the excitation voltage was reserved constant at 10mV. For the performance measurements, linear scan voltammetry was utilized with a step size of 5 mV and a scan rate of 5 mV/s. For all SOFC operations, electrochemical measurements were made at 785 ± 10 °C. SEM analyses were performed with an AMRAY 1820K Scanning Electron Microscope with an acceleration potential of 25kV.

3.3. Results

3.3.1 Porous Au anodes with different Au/YSZ interface area:

Four different porous Au anodes with different interface areas were prepared to evaluate the effect of interface contact area between Au and YSZ on SOFC current and power densities. Four typical Au patches with 1x8, 2x8, 3x8 and 4x8 mm dimensions are shown Figure 3.1.

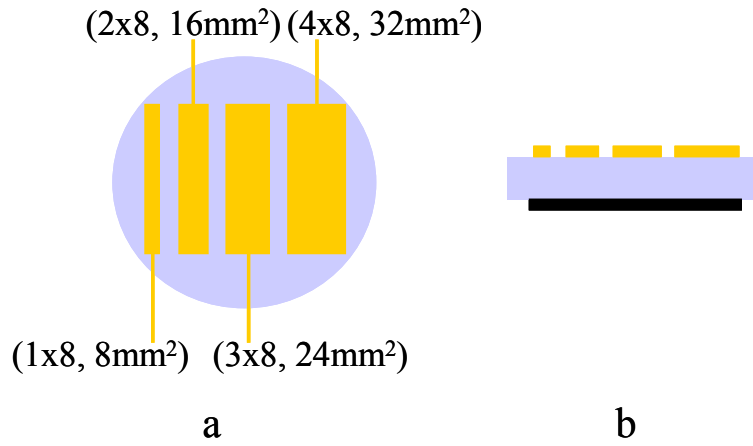


Figure 3.1: Schematic representation of experimental setup of four different interface areas between Au and YSZ, a) Top view, b) Cross-section.

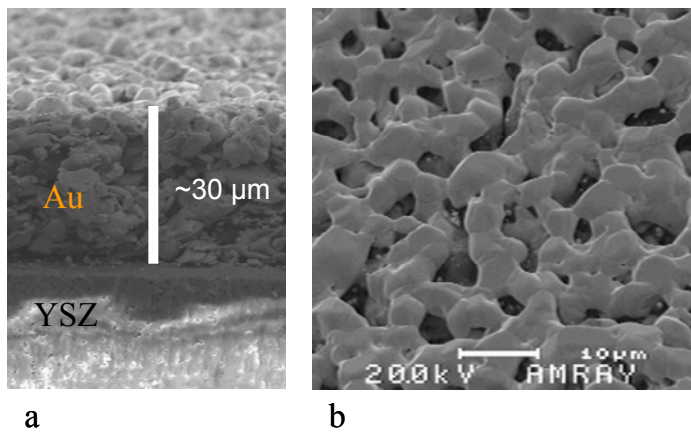


Figure 3.2: SEM images of porous Au anode, a) cross-section of electrode and electrolyte, b) top view of Porous Au anode.

SEM images of the porous Au anodes after 10 hours of H₂ fuel run under SOFC conditions are given in Figure 3.2. The images reveal that porous Au anode thickness is approximately 30 μ m with pore sizes of \sim 3-4 μ m.

Au wires were attached to each Au pattern by using Au paste. The performance of each electrode was monitored simultaneously by using a four channel potentiostat. To check the validity of the experiment, the four Au electrodes were wired together and additional polarization data were collected.

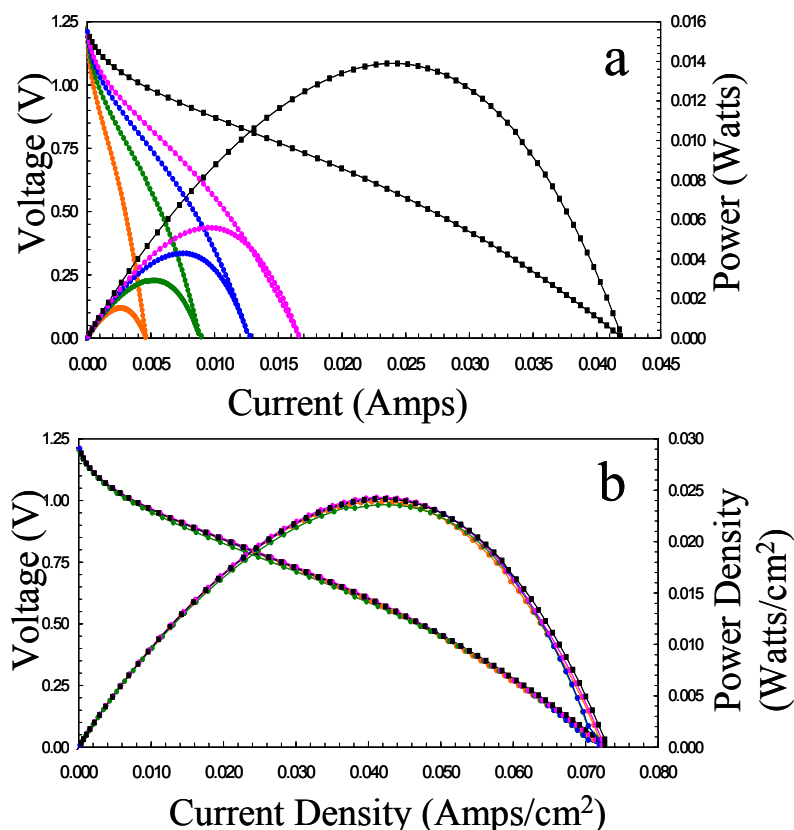


Figure 3.3: Polarization curves of porous Au anodes with different interface area experiments on YSZ, a) raw performance, b) normalized performance with respect to Au-YSZ interface area. (Orange: 1x8 mm (8 mm²), Green: 2x8 mm (16 mm²), Blue: 3x8 mm (24 mm²), Magenta: 4x8 mm (32 mm²) and Black: all four electrodes wired together).

Figure 3.3 shows the polarization curves of four separate Au electrodes with different interface areas in addition to the measurement in which all four electrodes

were wired together. Figure 3.3a demonstrates the raw polarization curves. However, when the current and power densities are normalized with respect to interface area between Au and YSZ, one can see from Figure 3.3b that all the electrode current and power densities are identical within experimental error. The maximum current and power densities of the four Au electrodes were ~ 0.072 Amps/cm² and ~ 0.0240 Watts/cm², respectively.

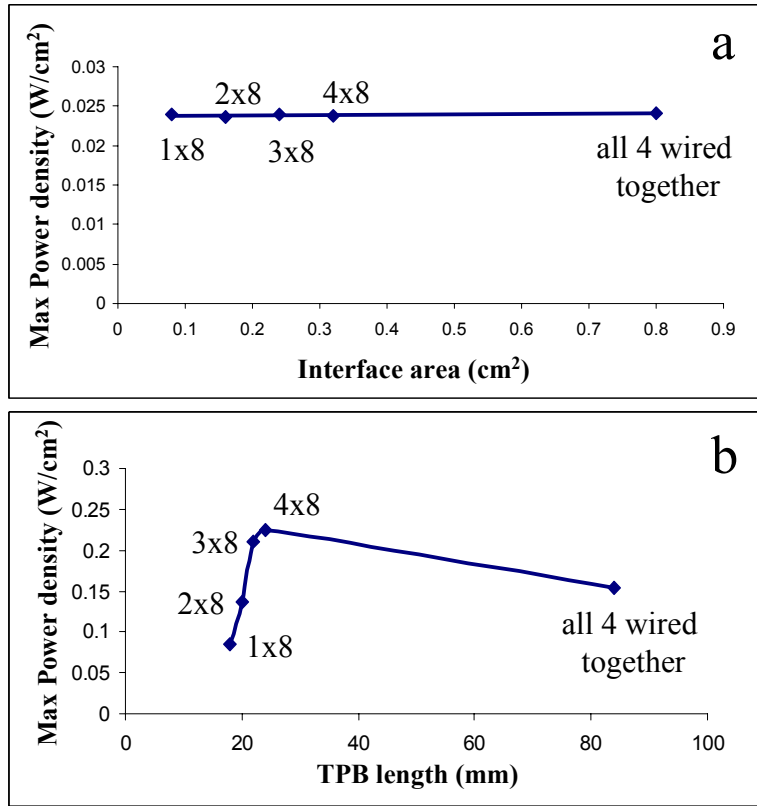


Figure 3.4: Normalization curves of Porous Au anode experiments, maximum power densities with respect to a) interface area between Porous Au and YSZ, b) triple phase boundary (TPB) length, i.e. perimeter of Porous Au anodes.

Porous Au anode power density normalization curves are given in Figure 3.4a (with respect to interface areas), and in Figure 3.4b (with respect to TPB lengths). The linear line in Figure 3.4a proves that SOFC power density values scale only with

interface area. The non-linearity in Figure 3.4b shows that the perimeter of the porous Au anode would not be accepted as a TPB length.

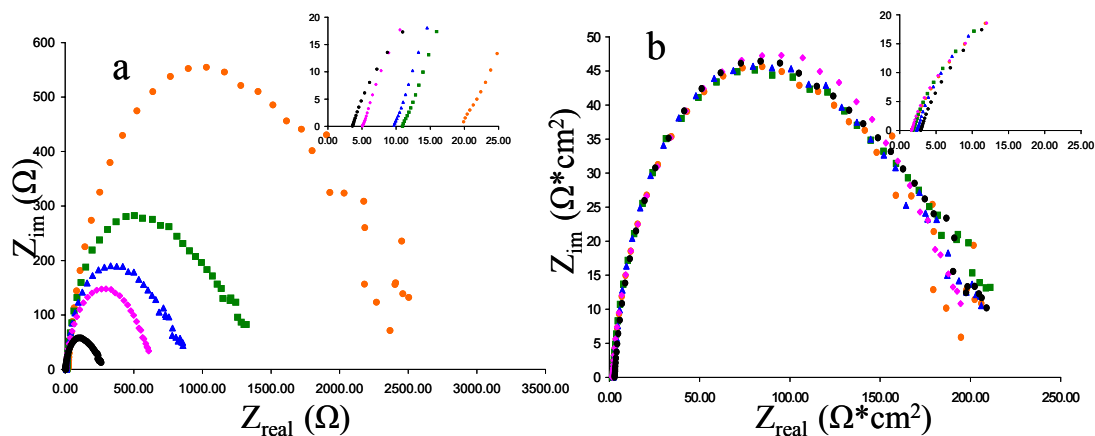


Figure 3.5: EIS (at OCV) curves of four different interface area experiments on YSZ, a) raw impedances, b) normalized with respect to interface area (inset: high frequency intercept as R_b) (Orange: 1x8 mm, Green: 2x8 mm, Blue: 3x8 mm, Magenta: 4x8 mm, and Black: all four electrodes wired together).

Another way to compare performances of different electrodes is Electrochemical Impedance Spectroscopy (EIS). An overview of the EIS method and the relevant parameters are given on Chapter 1. The bulk resistance, R_b , high frequency intercept, the polarization resistance, R_p , difference between two intercepts on the x -axis, and relaxation frequency of each arc, ω , frequency of arc highest point on the y -axis are the parameters on EIS curves. Figure 3.5 shows the EIS curves of four electrodes shown in Figure 3.1. The raw impedance data range from 250 Ω to 2500 Ω . However, when normalized, the impedance curves are virtually superimposable with R_p intercepts of 200-240 $\Omega \cdot cm^2$.

Table 3.1 summarizes the quantitative analysis of impedance curves seen in Figure 3.5a and 3.5b. The relaxation frequency, ω , of physical and chemical processes is at the maximum imaginary impedance value on the y -axis, and is related to the rate of physical or chemical process on SOFC systems [76, 77]. The measured relaxation

frequency, 318 Hz, is the same for every porous Au electrode. The R_b values are in the range 1.59-2.33 $\Omega \cdot \text{cm}^2$ and the R_p values are in the range 188-207 $\Omega \cdot \text{cm}^2$. These resistance values are two orders of magnitude higher than the state-of-art SOFC Ni/YSZ anode resistance values [36, 99], which confirms the same trend seen in the polarization curves. As explained previously, this is due to the poor catalytic properties of Au anode and the electrolyte thickness in these experiments.

Table 3.1: EIS data for porous Au anodes with different interface area experiments

Porous Au Electrodes	Frequency, ω	Raw R_b (Ω)	Raw R_p (Ω)	R_b ($\Omega \cdot \text{cm}^2$) Normalized WRT interface area	R_p ($\Omega \cdot \text{cm}^2$) Normalized WRT interface area
1x8 (8 mm²)	318 Hz	19.88	2346	1.59	188
2x8 (16 mm²)	318 Hz	10.93	1299	1.75	207
3x8 (24 mm²)	318 Hz	9.69	847	2.33	203
3x8 (32 mm²)	318 Hz	5.09	602	1.62	193
All (80 mm²)	318 Hz	3.66	257	2.93	206

3.3.2 Dense Au Film patterned Anodes:

The comparison of performances of porous and non-porous Au anodes with H_2 fuel provides a basis for evaluating the surface diffusion of adsorbed species, such as hydrogen and H^+ . The gas phase diffusion of H_2 through dense Au film is $5.9 \times 10^{-9} \text{ cm}^2/\text{s}$ and through dense Pd film is $3.6 \times 10^{-7} \text{ cm}^2/\text{s}$ [164, 165]. The gas diffusion of H_2 through dense Au film will be limited by the 2-D anode surface. This explains that only activation reactions take place on Au surface and H_2 molecules does not penetrate through Au film. The gas phase diffusion of H_2 will be eliminated from the list of limiting steps on H_2 oxidation reactions of SOFC anodes.

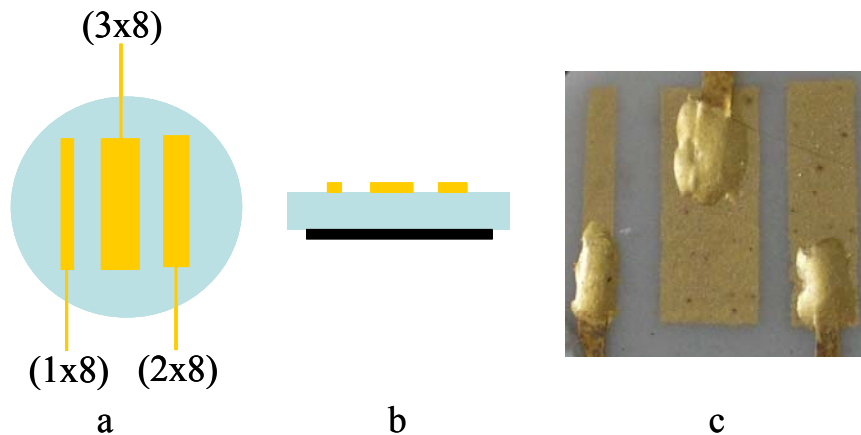


Figure 3.6: Schematic representation of experimental setup of four different interface areas between YSZ and Au film, a) Top view, b) Cross-section, c) Post Picture.

One micron thick Au film anodes with three different YSZ-Au interface areas were prepared by thermal evaporating of Au onto masked YSZ electrolytes and are shown in Figure 3.6. The picture in Figure 3.6c shows Au paste wire connections on Au films. Since the Au paste is porous after sintering, it is assumed that these Au paste connections would not effect the gas phase diffusion and thus Au film performance.

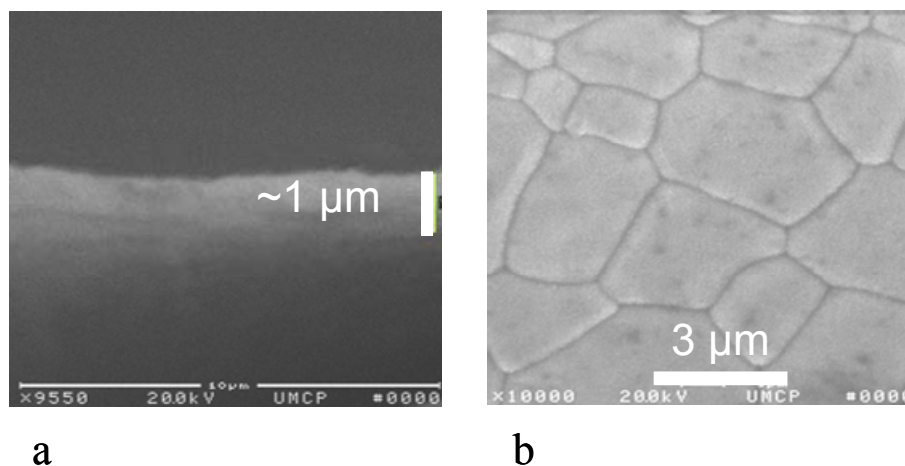


Figure 3.7: SEM images of Au film anode after 48 hours operation in SOFC, a) cross-section of delaminated Au film from YSZ surface b) top view of Au film on YSZ.

The SEM images of Au film anodes after 48 hours operation in SOFC are displayed in Figure 3.7. When the SEM images of dense Au film are compared with porous Au

anode SEM images (Figure 3.2b), it can be concluded that unlike the porous Au anodes, the Au film anodes are dense and possess no micron level porosity. Only grain boundaries of the Au film can be seen in SEM images of the Au film top view (Figure 3.7b).

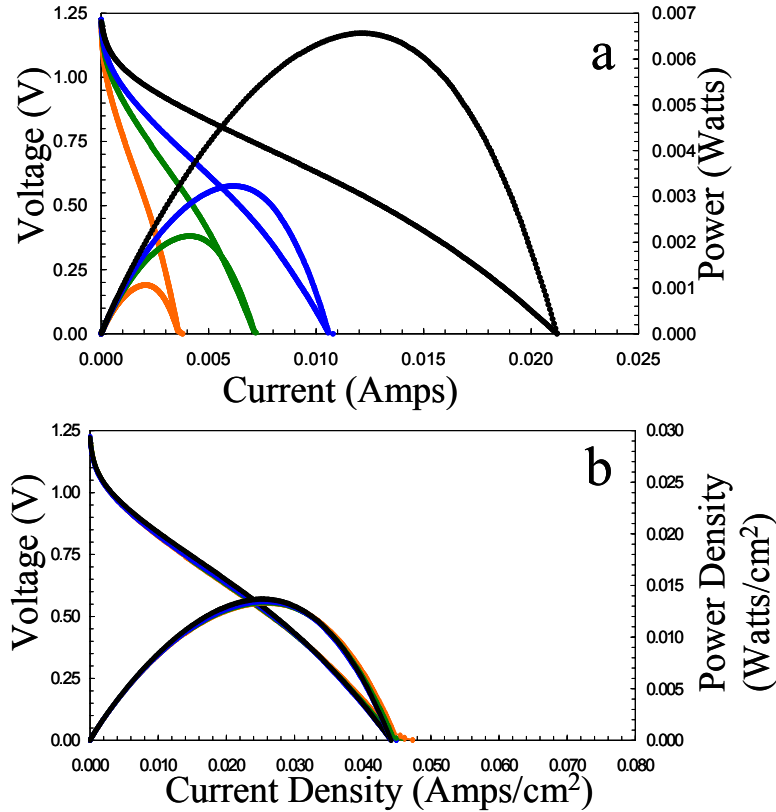


Figure 3.8: Polarization curves of Au film anodes with different interface area experiments on YSZ, a) raw performance, b) normalized performance with respect to Au-YSZ interface area. (**Orange**: 1x8 mm, **Green**: 2x8 mm, **Blue**: 3x8 mm, and **Black**: all three electrodes wired together).

The raw and the normalized polarization curves for these electrodes are shown in Figure 3.8a and in Figure 3.8b, respectively. Power density and current density values were calculated by using the Au-YSZ interface area between the Au film and the YSZ electrolyte. The Au film and paste anodes follow the same performance scaling with respect the Au-YSZ interface area. However, the Au film anodes have approximately

40 % less current and power density, i.e. 0.024 Watts/cm² for the porous Au and 0.014 Watts/cm² for the Au film.

Figure 3.9 shows two different normalization curves of maximum power densities for SOFC Au film anodes with respect to interface area and TPB length. Figure 3.9a has a linear correlation of the power density at 0.014 Watts/cm² with respect to the interface area of the Au film anodes, whereas Figure 3.9b has no correlation with respect to the TPB length of the Au film anodes.

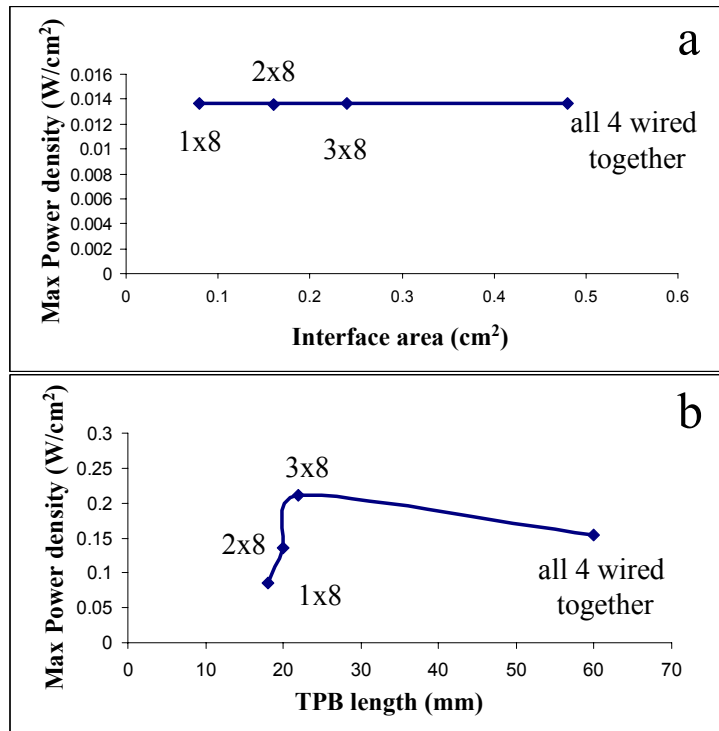


Figure 3.9: Normalization curves of Au film anode experiments, maximum power densities with respect to a) interface area between Au film and YSZ, b) triple phase boundary (TPB) length, i.e. perimeter of Au film anodes.

Figure 3.10 shows the raw and the normalized EIS curves for the Au film anodes. In Figure 3.10b, the impedances of the Au film anodes are normalized with respect to the Au film-YSZ interface area. A single arc is observed for all measurements in

Figure 3.10b, which is similar to that observed for the Au porous anodes suggesting that the same types of physical and chemical processes take place on both the dense and porous Au anodes. However, the Au film anode has higher R_p values relative to the porous electrode. The comparison of polarization curves in Figures 3.3 and 3.8 show that the porous Au anodes perform better than the Au film, which is supported by the comparison of the impedance curves in Figures 3.5 and 3.10.

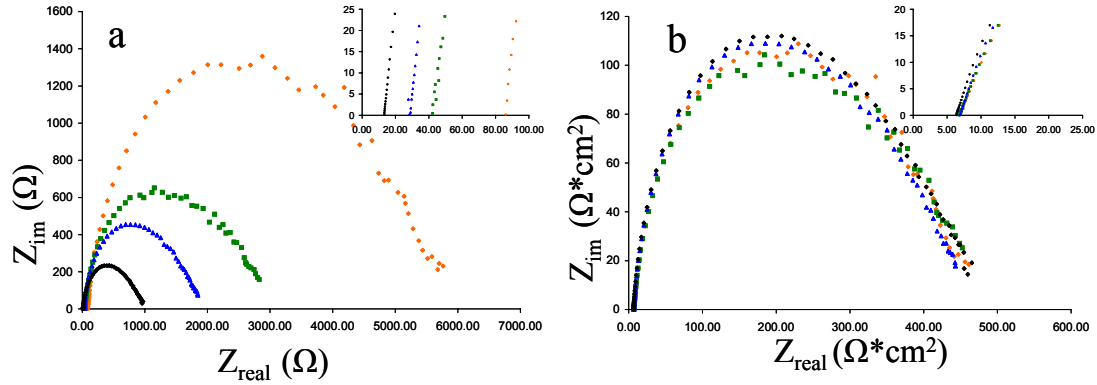


Figure 3.10: EIS curves (at OCV) of three Au film anodes with different interface areas a) raw impedances, b) normalized with respect to interface area (inset: high frequency intercept as R_b). (Orange: 1x8 mm, Green: 2x8 mm, Blue: 3x8 mm, and Black: all three electrodes wired together).

Table 3.2 is the quantitative analysis of impedance curves shown in Figure 3.10a and 3.10b. The relaxation frequency, 794 Hz, is the same for all Au film anodes. This relaxation frequency would be the average-combined frequency for both the physical and the chemical processes in the SOFC system. The average-combined relaxation frequency for Au film impedance arc is higher than that of porous Au anodes. This suggests a faster rate of the composite physical and chemical processes on Au film than on porous Au. The understanding of the process responsible for this is difficult to address with a single arc of the impedance curve. The normalized R_b and R_p values are in the range of 6.39-6.97 $\Omega \cdot cm^2$ and 436-454 $\Omega \cdot cm^2$, respectively. These resistance values are approximately doubled as compared to porous Au anode

resistance values, which support the trend observed in the polarization curves. As explained previously, this is because of the Au anode and the thick electrolyte used in these experiments.

Table 3.2: EIS data for Au film anodes with different interface area experiments

Au film Electrodes	Frequency, ω	Raw R_b (Ω)	Raw R_p (Ω)	R_p ($\Omega \cdot \text{cm}^2$) Normalized WRT interface area	R_p ($\Omega \cdot \text{cm}^2$) Normalized WRT interface area
1x8 (8 mm²)	794 Hz	86.06	5594	6.88	447
2x8 (16 mm²)	794 Hz	42.26	2782	6.76	445
3x8 (24 mm²)	794 Hz	28.43	1815	6.97	436
All (48 mm²)	794 Hz	13.32	945	6.39	454

3.3.3 Porous Au Anodes with YSZ over layers:

The catalytic effects of both Au and YSZ on SOFC performance were examined by using different geometries of porous Au electrodes selectively covered with porous YSZ. For this investigation, four (two 2x8 and two 3x8) symmetric electrodes were fabricated (shown in Figure 3.11) and one of each electrode was covered with a porous YSZ.

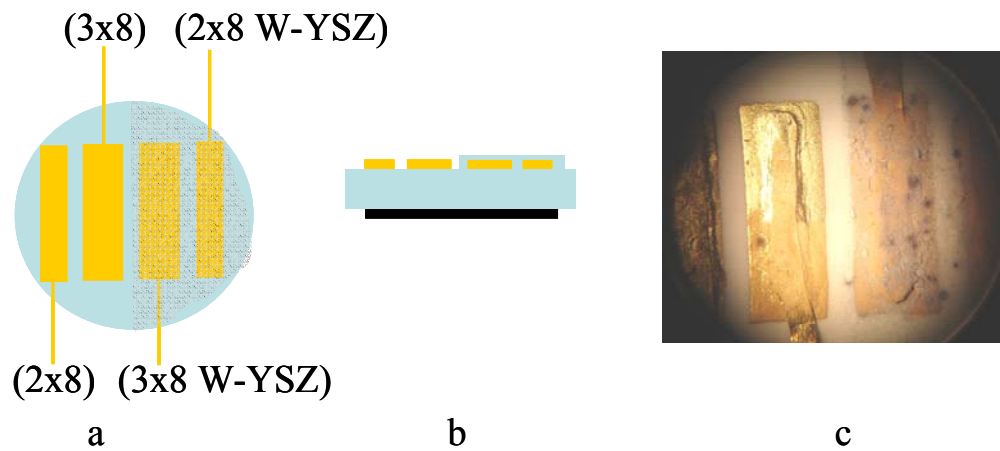


Figure 3.11: Schematic representation of experimental setup of two different interface areas between Au and YSZ and half covered with porous YSZ layer, a) Top view, b) Cross-section, c) Assembly picture after operation.

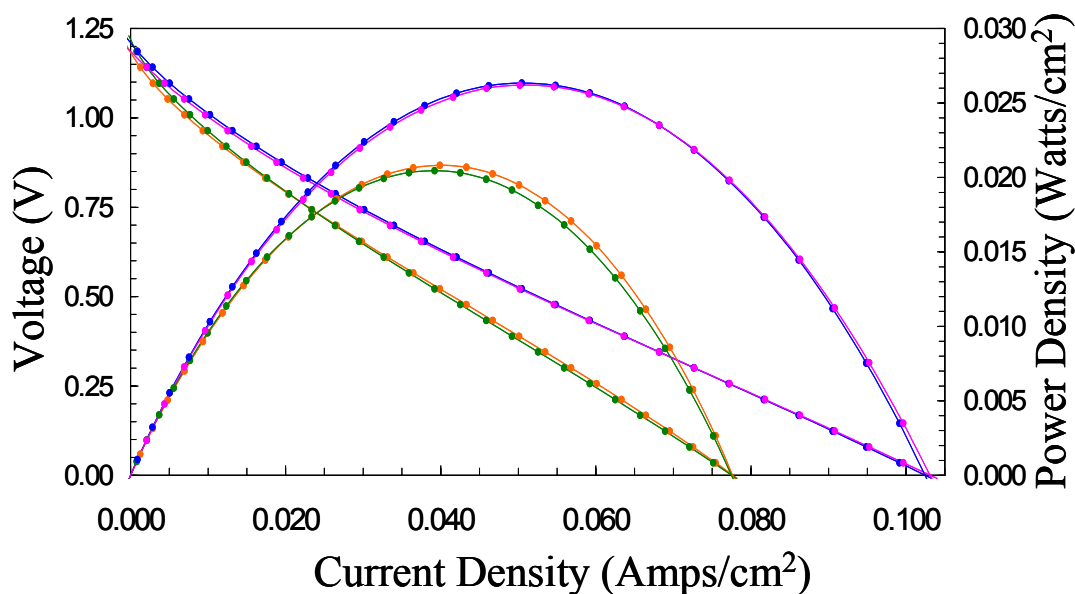


Figure 3.12: Polarization curves of porous Au anodes with and without porous YSZ over layers (normalized with respect to Au-YSZ interface area) (**Orange**: 2x8 mm, **Green**: 3x8 mm, **Blue**: 3x8 mm with porous YSZ layer, **Magenta**: 2x8 mm with porous YSZ layer).

The polarization curves of the porous Au anodes with and without YSZ layers are shown in Figure 3.12. The power and current densities were again normalized with respect to interface area between Au and YSZ electrolyte. The performance values of the uncoated electrodes are virtually identical to those of described previously (see Figure 3.3). However, the power densities of the coated anodes are ~ 0.025 Watts/cm², which is higher than the previous experimental configurations.

The EIS curves of the coated and uncoated Au anodes are shown in Figure 3.13. Table 3.3 summarizes the impedance data extracted from the curves in Figure 3.13. After normalization with respect to Au-YSZ interface area, the EIS curves of the coated electrodes are the same within experimental error and have lower R_b and R_p values than the uncoated electrodes. The R_b values for all porous Au anodes are in the range of 3.15-3.26 $\Omega \cdot \text{cm}^2$, and are the same within experimental error. However, the

R_p values are $197 \Omega \cdot \text{cm}^2$ and $146\text{-}151 \Omega \cdot \text{cm}^2$ for the coated and the uncoated electrodes, respectively.

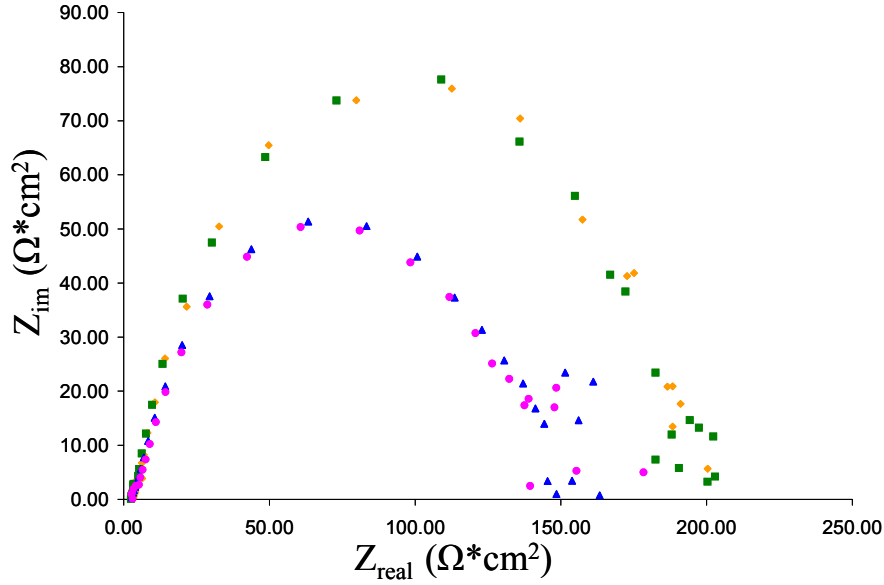


Figure 3.13: EIS curves (at OCV) of four different porous Au anodes with and without porous YSZ over layers, normalized with respect to Au-YSZ interface area. (Orange: 2x8 mm, Green: 3x8 mm, Blue: 3x8 mm with porous YSZ over layer, Magenta: 2x8 mm with porous YSZ over layer).

Table 3.3: EIS data for porous Au anodes with and without porous YSZ over layers.

Porous Au Electrodes (Au-YSZ interface area)	Frequency, ω	R_p ($\Omega \cdot \text{cm}^2$) Normalized WRT interface area	R_p ($\Omega \cdot \text{cm}^2$) Normalized WRT interface area
2x8 (16 mm ²)	682 Hz	3.22	197
3x8 (24 mm ²)	682 Hz	3.15	197
3x8 w/ YSZ layer (24 mm ²)	682 Hz	3.26	146
2x8 w/ YSZ layer (16 mm ²)	682 Hz	3.18	151

3.3.4 Porous Au Anodes with an isolated porous YSZ patch:

To evaluate the role of YSZ as the O^{2-} ion source (TPB generator) and to address the question about the catalytic role of YSZ on the H_2 fuel oxidation, an additional set of porous Au anodes with and without isolated porous YSZ patches were designed and are shown in Figure 3.14. In contrast to the previous experiments, this porous YSZ patch was not in contact with the bulk YSZ electrolyte. As discussed in the previous section, the enhanced current and power density of the coated electrode is due to the YSZ over layer as O^{2-} ion carrier to the anode surface. Three different porous Au anodes (2x8 mm, 3x8 mm, and 3x8 with 1x6 mm porous YSZ layer) were fabricated on a home-made YSZ disk.

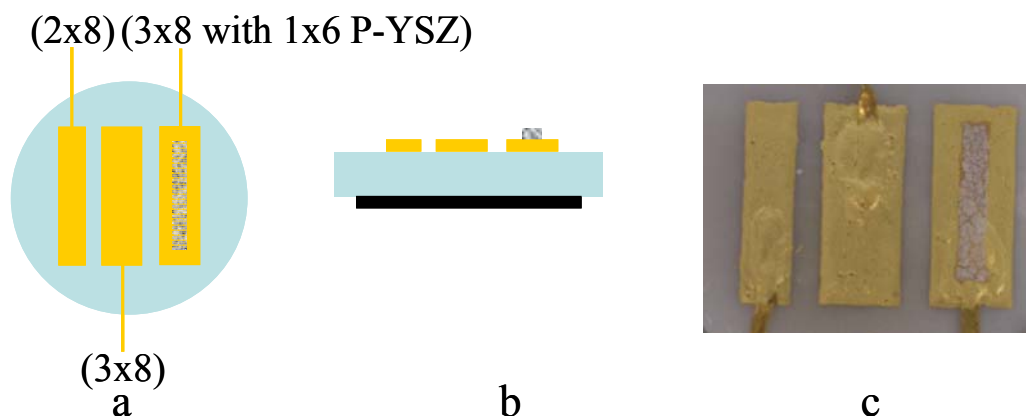


Figure 3.14: Experimental setup of two different interface areas between Au and YSZ and one with porous YSZ layer patch, a) Schematic representation from top, b) Cross-section, c) Post-experiment Picture.

The polarization curves shown in Figure 3.15 are for these three different porous Au anodes represented in Figure 3.14. The power and current density values were normalized by the interface areas between the porous Au anodes and the YSZ bulk electrolyte. At low current densities all three electrodes display identical I-V

characteristics. However, at higher current densities ($> 0.025 \text{ A/cm}^2$), the performance of the anode with the YSZ patch diminishes and results a lower maximum power density (0.016 Watts/cm^2) relative to the uncoated anodes ($\sim 0.018 \text{ Watts/cm}^2$).

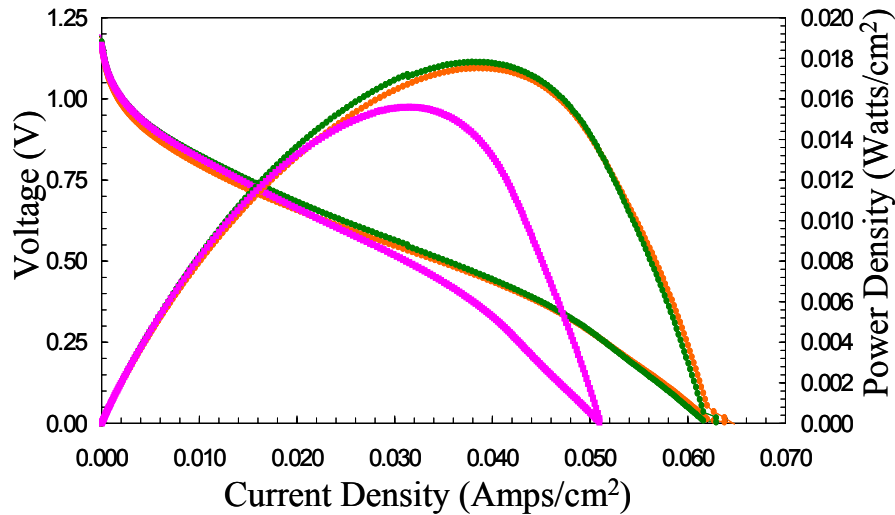


Figure 3.15: Polarization curves of porous Au anodes with different interface area and one with porous YSZ island on top (**Orange**: 2x8 mm Porous Au, **Green**: 3x8 mm Porous Au, **Magenta**: 3x8 mm Porous Au with 1x6 mm porous YSZ layer on top).

The EIS curves of these three different porous Au anodes are presented in Figure 3.16. The trend shown in these curves is the same as in the performance curves, which explains that the coated Au anode with YSZ patch on electrode surface has larger polarization resistance than the two uncoated electrodes.

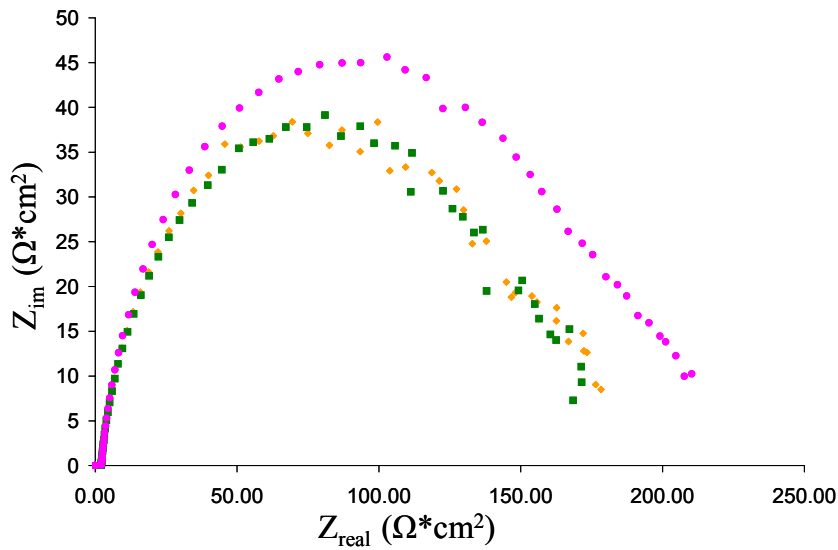


Figure 3.16: EIS curves (at OCV) of porous Au anodes with different interface area and one with porous YSZ island on top, normalized with respect to the interface area between porous Au and YSZ electrolyte. (Orange: 2x8 mm Porous Au, Green: 3x8 mm Porous Au, Magenta: 3x8 mm Porous Au with 1x6 mm porous YSZ layer on top).

Table 3.4 contains a summary of EIS data in Figure 3.16. The relaxation frequencies of all three electrodes are 794 Hz, which is comparable to other interface area experiments. The R_b values of all three electrodes are in the range of 2.03-2.17 $\Omega\cdot\text{cm}^2$, which are identical within experimental error. However, the R_p values differ between two porous Au only electrodes (175-176 $\Omega\cdot\text{cm}^2$) and one porous Au electrode with an isolated YSZ patch (204 $\Omega\cdot\text{cm}^2$).

Table 3.4 EIS data analysis for porous Au anodes, one with isolated porous YSZ patch.

Porous Au Electrodes (Au-YSZ interface area)	Frequency, ω	R_b ($\Omega\cdot\text{cm}^2$) Normalized WRT interface area	R_p ($\Omega\cdot\text{cm}^2$) Normalized WRT interface area
2x8 (16 mm²)	794 Hz	2.03	176
3x8 w/ (24 mm²)	794 Hz	2.12	175
3x8 w/ isolated 1x6 YSZ patch (24 mm²)	794 Hz	2.17	204

3.3.5 Porous Au anodes with different $\alpha\text{-Al}_2\text{O}_3$ sub-surface blocking between porous Au and YSZ:

Fleig *et al.* demonstrated that $\alpha\text{-Al}_2\text{O}_3$ blocks O^{2-} transport and can be used to regulate O^{2-} flux to the TPB region [157]. The performance of SOFC anodes can be evaluated by using the four different Au anodes with same geometric areas and thicknesses but with different sub-surface $\alpha\text{-Al}_2\text{O}_3$ blockings and different Au anode-YSZ electrolyte contact areas. To evaluate the effect of O^{2-} flux on the Au anode performance, porous Au anodes with different $\alpha\text{-Al}_2\text{O}_3$ sub-surface blocking areas were fabricated and shown in Figure 3.17. The $\alpha\text{-Al}_2\text{O}_3$ sub-surface blocking squares with the thickness of 0.1 μm were deposited on a YSZ disk by using e-beam deposition. Porous Au anodes were fabricated on top of the patterned $\alpha\text{-Al}_2\text{O}_3$ regions as shown in Figure 3.17.

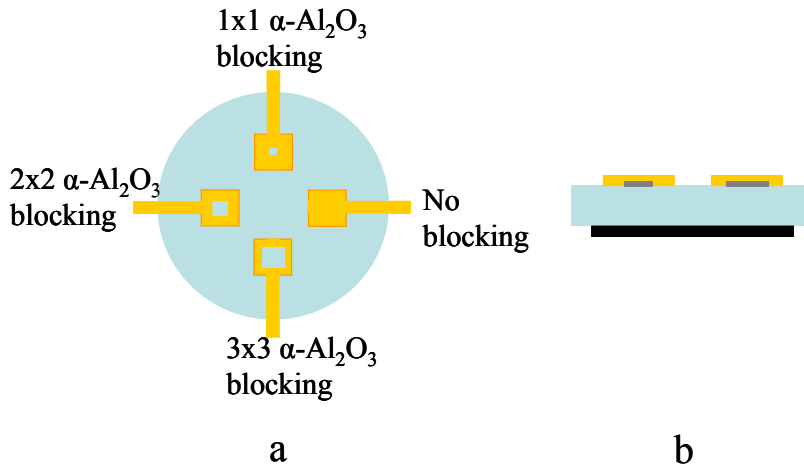


Figure 3.17: Experimental setup of four different interface areas between porous Au and YSZ by using $\alpha\text{-Al}_2\text{O}_3$ blocking, a) Top view, b) Cross-section (right: 5x5mm Porous Au with 2x2mm $\alpha\text{-Al}_2\text{O}_3$ blocking and left: 5x5mm Porous Au with 3x3mm $\alpha\text{-Al}_2\text{O}_3$ blocking).

The polarization curves of the four different $\alpha\text{-Al}_2\text{O}_3$ blocked electrodes are shown in Figure 3.18. The data were processed three different ways: the raw data are shown in (a), the same data normalized to the Au surface area are shown in (b), and finally

the raw data normalized to the Au-YSZ interfacial area (i.e. Au area- α -Al₂O₃ area) are shown in (c). The contact areas between porous Au anodes and YSZ electrolyte are 0.25, 0.24, 0.21, and 0.16 cm². Therefore, these polarization curves show the correlation of contact areas between the porous Au and YSZ electrolyte.

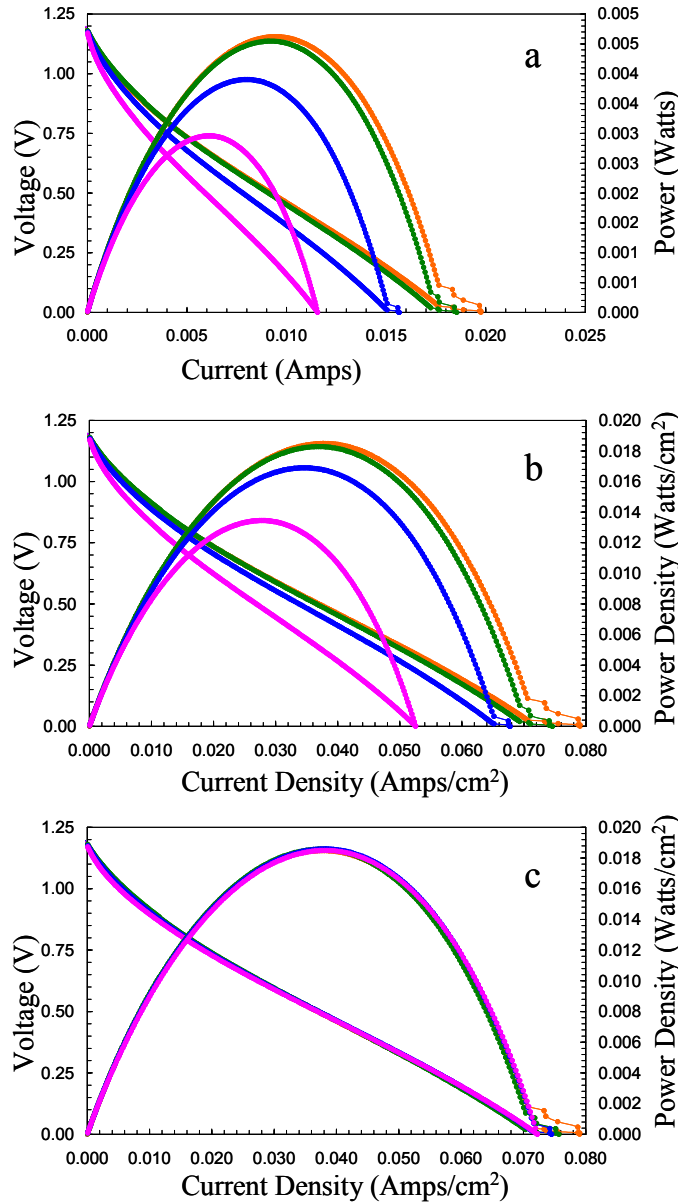


Figure 3.18: Polarization curves of Porous Au anodes with α -Al₂O₃ blocking a) Raw performance data, b) performance data normalized with respect to Au area, c) performance data normalized with respect to Au-YSZ contact area (α -Al₂O₃ blocking area subtracted) (Orange: 5x5mm porous Au, Green: 5x5mm porous Au with 1 mm² α -Al₂O₃, Blue: 5x5mm porous Au with 4 mm² α -Al₂O₃, Magenta: 5x5mm porous Au with 9 mm² α -Al₂O₃).

The EIS curves of the four different α -Al₂O₃ blocked electrodes are shown in Figure 3.19. Raw impedance data shown in Figure 3.19a varies in a large resistance range on the real part of the impedance curves. However, four porous Au anodes with and without α -Al₂O₃ blocks give identical EIS curves when normalized with respect to porous Au-YSZ electrolyte contact area. The similarities in the single composite arcs in the normalized EIS curves are consistent with the similarities in the normalized polarization curves.

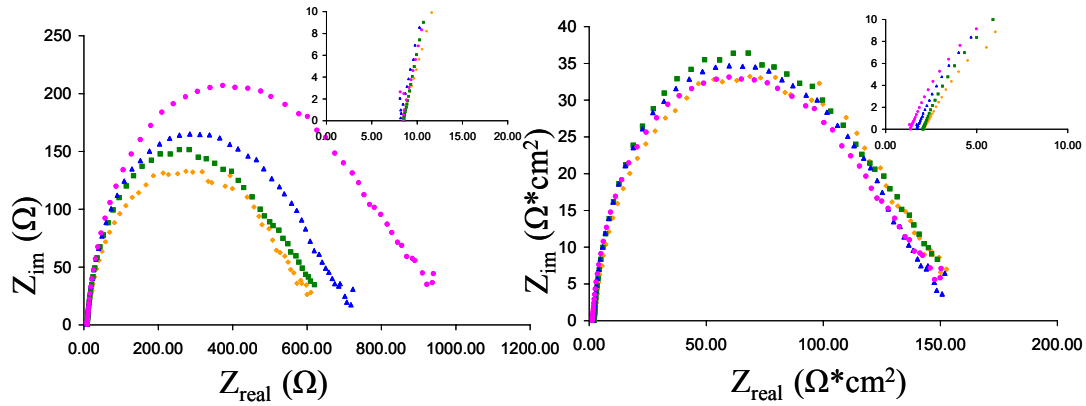


Figure 3.19: EIS curves (at OCV) of porous Au anodes with α -Al₂O₃ blocking, a) Raw data, b) normalized with respect to contact area between porous Au and YSZ electrolyte (inset: high frequency intercept as R_b) (Orange: 5x5mm Porous Au only, Green: 5x5mm Porous Au with 1x1mm α -Al₂O₃ blocking, Blue: 5x5mm Porous Au with 2x2mm α -Al₂O₃ blocking, Magenta: 5x5mm Porous Au with 3x3mm α -Al₂O₃ blocking).

A summary of the EIS data for the α -Al₂O₃ blocking experiments is given in Table 3.5. The relaxation frequency value of the composite single arc of Au anodes in these impedance experiments is equal to 794 Hz, which is close or the same relative to previous interface area experiments. The raw and normalized R_b values are shown in the inset of both Figures 3.19a and 3.19b. The raw R_b values of the porous Au anodes with and without α -Al₂O₃ blocking are in the range of 8.36-8.66 Ω*cm².

Table 3.5: EIS data for porous Au anodes, with α -Al₂O₃ blocking.

Porous Au Electrodes (Au-YSZ contact area)	Frequency, ω	Raw R_b (Ω)	Raw R_p (Ω)	R_b ($\Omega \cdot \text{cm}^2$) Normalized WRT Au-YSZ contact area	R_p ($\Omega \cdot \text{cm}^2$) Normalized WRT Au-YSZ contact area
5x5 (25 mm ²)	794 Hz	8.36	1788	2.09	447
5x5 w/ 1mm ² α -Al ₂ O ₃ blocking (24 mm ²)	794 Hz	8.53	1854	2.05	445
5x5 w/ 4mm ² α -Al ₂ O ₃ blocking (21 mm ²)	794 Hz	8.66	2076	1.82	436
5x5 w/ 9mm ² α -Al ₂ O ₃ blocking (16 mm ²)	794 Hz	8.48	2838	1.36	454

3.4. Discussions

3.4.1 Porous Au anodes with different Au/YSZ interface area:

Porous Au anodes power densities (~ 0.0240 Watts/cm² in Figure 3.3 and 3.4) are approximately 1 order of magnitude lower than 0.5-0.6 Watts/cm² output from conventional SOFCs with Ni/YSZ anode supported systems and very thin YSZ electrolytes [36]. Since porous Au, which is considered as an inert metal for H₂ oxidation, and 1.18 mm thick YSZ electrolytes are used in this study, the low power density values are anticipated.

The porous Au anode power densities correlate with respect to Au-YSZ interface areas. It is proposed that the sum of the micron size Au particle perimeters in the SEM images should be accepted as the TPB length, since the entire area of the Au anode is porous. The TPB length per interface area will be the same for porous Au anodes, because the same Au paste and sintering steps are employed to each anode.

Although the four electrodes are on the same electrolyte disk, they are not electronically connected. When the four electrodes are wired together, their

performances are additive, as shown in the identical normalized performance curves and the linearity with respect to interface areas of porous Au anodes.

Figure 3.5b shows a single arc for each electrode. This can be interpreted as the combination of all physical processes and chemical reactions (i. e. activation, diffusion, charge transfer, and desorption) are correlated with respect to the electrode interface area. The distinction between physical processes and chemical reactions is difficult to make. This can be done by using either a fitting circuit, with many possibilities to have different circuit elements for each process and chemical or physical computational modeling to analyze this composite resistive-capacitive single arc in EIS curves. The bulk resistance, R_b , the polarization resistance, R_p , and the relaxation frequencies of arcs, ω , are deduced from EIS curves.

The gas phase diffusion of H_2 through porous Au anode would not be the limiting for the SOFC performance due to the 30 μm thin porous Au anodes, high fuel concentration, low current and power densities. As a result of correlations in the polarization and impedance curves, the SOFC performance is limited to processes and chemical reactions occurring on the interface between Au and YSZ. These processes can be surface diffusion on Au or YSZ, charge-transfer reaction, and desorption of water.

3.4.2 Dense Au Film patterned Anodes:

The Au film power densities (Figure 3.8 and 3.9) show the correlation with respect to Au-YSZ interface areas. The thickness of the Au film is $\sim 1 \mu m$ as compared to the porous Au anode thickness of $\sim 30 \mu m$. However, the 40 % less power densities compared to porous Au can be attributed to the porosity difference between these two

different Au anodes. The porosity of the anode material affects the number of reactive sites due to the grain size difference between the Au film and the porous Au. The gas phase diffusion of H_2 through porous Au is 3-D diffusion. This process can be thought of as 2-D diffusion on the Au film surface, since it is not permeable to H_2 . The current and power density scaling of the Au film anode is explained by the surface diffusion of the fuel species through the Au film anode. It is known that the surface diffusion of adsorbed species on anode surface has higher resistance than gas phase diffusion. Hence, the surface diffusion is possibly the limiting step in H_2 oxidation reaction kinetics in Au film anodes.

Unlike the porous Au anodes, the Au film anodes preclude gas phase diffusion as a rate limiting step for H_2 fuel oxidation. These performance correlations of dense Au films suggest the existence of other rate limiting steps. Since H_2 gas phase diffusion through the Au film is negligible, the dense Au film anode catalyzes the dissociative adsorption of H_2 at a certain level and then the adsorbed species on the Au surface diffuse through the electrode-electrolyte interface via Au film grain boundaries shown in SEM images. Therefore, this performance and composite resistances (Figure 3.10 and Table 3.2) correlations with respect to the interface area can be attributed to surface diffusion of adsorbed species, charge transfer reactions, and desorption of water, all of which are known to take place near the electrode-electrolyte interface.

3.4.3 Porous Au Anodes with YSZ over layers:

According to data in Figure 3.12 and 3.14, it is proposed that these YSZ over layers facilitate transporting O^{2-} ions to the anode surface and provide extra interface area to surface of the porous Au anodes. The increase in interface area causes the higher

number of triple phase boundaries for charge transfer reaction. This explains the better performance for two coated Au electrodes. The two porous Au electrodes with a porous YSZ over layer generate approximately ~20 % higher current and power densities than the uncoated Au electrodes. Also, the ~20% drop in the polarization resistance for the coated Au electrodes is consistent with their higher power densities.

3.4.4 Porous Au Anodes with an isolated porous YSZ patch:

It is proposed that the YSZ patch on electrode surface precludes the fuel activation processes and surface diffusion of adsorbed species on porous Au anode surface (Figure 3.15 and 3.16). The 15 % less power density of porous Au with YSZ patch is explained by the fact that porous YSZ layer is blocking some of active sites on the porous Au anode with YSZ patch. Active sites on the porous Au electrodes are thought to be responsible for the dissociative adsorption of H_2 fuel and surface diffusion of adsorbed species on Au anode surface. The limiting process in the case of porous Au anode with a porous YSZ patch is surface diffusion of adsorbed species on Au anode surface. The effect of surface diffusion is observed in the higher current regime of polarization curve due to the limitation in mass transport of adsorbed species. The YSZ patch does not have any contact to YSZ electrolyte, which reveals that O^{2-} ions could not be transported to the top of the Au electrode. The enhanced performance in the previous experiments of porous Au anode entirely coated by the porous YSZ layer is not observed in the case of isolated YSZ patch on porous Au anodes, since there is not O^{2-} ions transport to the electrode surface.

EIS measurements also show that the R_p values between two porous Au only electrodes are the same; however, that of porous Au electrode with an isolated YSZ

patch is 15 % more relative to without YSZ. This can be explained by the porous YSZ patch blocking active sites on Au anode. Since some of the active sites for H₂ dissociative adsorption and surface diffusion of adsorbed species on Au anode surface are blocked, these would be seen on EIS curve as additional resistance on R_p.

3.4.5 Porous Au anodes with different α -Al₂O₃ sub-surface blocking between porous Au and YSZ:

The polarization curves of porous Au with blocking show the correlation of contact areas between the porous Au and YSZ electrolyte (Figure 3.18). The normalized power densities are ~ 0.0185 Watts/cm². The power and current densities are well within 0.0180-0.0240 Watts/cm² range of power densities observed for porous Au anodes in this study. The variation of power densities arises from slight differences in SOFC materials, such as electrolytes (thickness), cathodes (morphology), and porous Au anodes (Au wire on the top electrode).

In contrast to other porous Au-YSZ interface experiments, the range of R_b values diverge when normalizing with respect to Au-YSZ contact area to the range of 1.36-2.09 $\Omega \cdot \text{cm}^2$ in Figure 3.19 and Table 3.5. The reason of this narrow range of the R_b values is explained by the property of α -Al₂O₃ that is dielectrically permeable at high frequencies of impedance measurements [157]. Thus, α -Al₂O₃ does not block O²⁻ ion flux so that the entire Au electrode area participates in the physical and chemical processes at high frequencies[157]. The contact area normalized R_p values are in the range of 436-454 $\Omega \cdot \text{cm}^2$ (Table 3.5). R_p values are already correlated with respect to the geometric area of the porous Au anodes due to dielectric permeability of α -Al₂O₃ at high frequencies. The interface reactions are classified into three groups: surface

diffusion of adsorbed species through porous Au anodes, charge-transfer reactions, and H₂O desorption. Consequently, the sum of these three reactions is proposed to be responsible for these composite single arc impedance curves of porous Au anodes.

Three interface reactions play the key role as the rate limiting steps in the SOFC anode side. The losses due to gas phase diffusion of H₂ fuel are believed to be negligible and not a limiting step for these systems. However, the surface diffusion of dissociatively adsorbed fuel species on the Au 2-D surface is thought to be a hindrance for the porous Au anode performance. Because, H₂ sticking coefficient on Au is two orders of magnitude lower relative to that of Ni. It is also reported that O²⁻ ions are involved in the charge-transfer reaction. By using the sub-surface α -Al₂O₃ blocking it is concluded that the charge-transfer reactions take place only at the porous Au electrode-YSZ electrolyte interface. The gas phase diffusion and the transport of O²⁻ ions on the 3-D Au bulk is negligible relative to other anode materials such as Ni/YSZ systems. The polarization and the EIS data of these series of partially blocked electrodes exclude the O²⁻ ion transport through Au anode if the charge-transfer reaction is assumed to be occurring only in the interface.

H₂O desorption from the interface is another factor that affects the charge-transfer reactions between adsorbed species and O²⁻ ions. The production of H₂O causes the surface diffusion competition between adsorbed fuel species and H₂O on the active sites of 3-D Au bulk. In that respect, the surface diffusion of adsorbed species on both 2-D and 3-D Au is able to influence the charge-transfer reaction rate. Consequently, possible rate limiting steps are surface diffusion of adsorbed species, charge transfer reactions in the interface, and desorption of H₂O from electrode-electrolyte interface.

3.5. Conclusions

Understanding of the H_2 oxidation kinetics in SOFC materials is very complicated due to difficulties in observing possible intermediate species and in determining where the reaction steps take place at SOFC anode systems. Results presented in this work show that the possible rate limiting steps in anodic H_2 oxidation are (i) the surface diffusion of dissociatively adsorbed species such as H_2 and H on Au, (ii) the charge-transfer reactions of these adsorbed species, (iii) the desorption of H_2O from anode-electrolyte interface.

SOFC performance correlates with Au anode-YSZ electrolyte interface area, regardless of the different porosities of Au anodes and the geometries of porous YSZ coatings on the porous Au anodes. These trends are observed on the polarization curves and on the EIS curves. This correlation is ascribed to the limitations in the reaction steps taking place in this interface. The comparison of performance data of the two different types of Au anodes, such as porous Au and dense Au film anodes, confirms that the gas phase diffusion of H_2 is not a limiting step for H_2 oxidation, since the performance correlation is observed in both porous and dense film anodes. This correlation also reveals that the TPB length is the sum of the perimeters of Au particles in contact with YSZ electrolyte.

Two geometrically different porous YSZ experiments on porous Au anodes were evaluated to understand the contribution of YSZ on H_2 oxidation kinetics. A YSZ layer in contact with the electrolyte and coating the entire porous Au anodes helps to transport O^{2-} ions via contact between the YSZ electrolyte and the perimeters of porous Au anodes. This results approximately 20 % superior performance relative to

the uncoated Au anodes. However, when the effect of porous YSZ layer that is not in contact with the electrolyte (isolated porous YSZ patch) was examined, the uncoated Au anodes performed 15 % higher than porous Au anode with YSZ patch on top. Hence, an isolated porous YSZ patch on the top of porous Au anode has a diminishing effect on H_2 dissociative adsorption reaction, and this patch is not helping to transport O^{2-} ions to the top of porous Au anode. Although the YSZ layer reduces the dissociative adsorption of H_2 on 2-D Au surface, these two geometrically different porous YSZ experiments show that there are two affects of YSZ, the blocking of activation of H_2 and the helping of charge-transfer reactions on porous Au surface via O^{2-} ions. When there are O^{2-} ions on 2-D Au surface, charge-transfer reaction takes place and O^{2-} ions enhance the SOFC performance.

The $\alpha-Al_2O_3$ blocking experiments were designed to address the effect of the O^{2-} ion flux on H_2 oxidation kinetics on porous Au anodes. These experiments would explain that the electrochemical oxidation path of H_2 and dissociatively adsorbed species is through Au bulk. Since porous Au anodes are permeable to H_2 gas phase, charge-transfer reaction sites (triple phase boundaries) are distributed across the entire interface between Au electrode and YSZ electrolyte. Therefore, the surface diffusion of dissociatively adsorbed species on 3-D Au bulk is the possible rate limiting step. Water desorption from reactive interface sites would affect the SOFC anode performance. These three rate limiting steps will be discussed and analyzed in further detail in the next chapter.

Chapter 4:

Isotopically labeled D₂ fuel comparison with H₂ on Au anode SOFCs by experimental and computational methods

4.1. Introduction

The H₂ oxidation reaction mechanism appears simple at first glance. However, investigating the H₂ oxidation kinetics under SOFC conditions is complicated due to difficulties in designing an experiment to distinguish the reaction steps as well as technical difficulties to observe possible intermediates on SOFC anodes. The studies presented in Chapters 1 and 3 show three possible limiting steps in the H₂ oxidation reaction mechanism on SOFC anodes. These are the surface diffusion of dissociatively adsorbed H₂ species on Au anodes, the charge transfer reaction of these adsorbed species at the anode-electrolyte interface, and the desorption of H₂O from the anode-electrolyte interface.

Many researchers have studied H₂ oxidation mechanisms on conventional Ni/YSZ anodes [35, 36, 38, 40, 100, 110, 162, 163, 166]. Ni has been recognized as one of the most active metals for the dissociation of H₂. These studies have mainly proposed and agreed with each other about the gas phase diffusion of H₂ as well as to the formation of a hydroxyl species and the contribution of these two phenomena on Ni/YSZ anode systems. A major distinction has been found concerning where the physical and chemical processes take place, either only on the Ni surface or both on the Ni and on the YSZ surface. Mizusaki *et al.* [167] has proposed that only the Ni surface was electrochemically active and Jiang *et al.* [166, 168-170] has included the surface

processes on the YSZ surface into the mechanism. The surface diffusion of adsorbed H_2 fuel and hydroxyl species on the anode surface has been considered for the mechanism elsewhere [37, 104, 163, 170]. The effect of partial pressures of H_2 and H_2O for the H_2 oxidation mechanism has been the subject of numerous experimental and computational studies [37, 72, 104, 108, 116, 163, 166, 169, 170]. However, after all these studies, there has not yet been a clear mechanism established for H_2 oxidation on Ni/YSZ anode systems under SOFC conditions. The Ni/Ni^{2+} redox couple in Ni/YSZ anode systems near the triple phase boundaries has suggested that the fuel and steam compositions should be optimized to distinguish the different steps in the mechanism for the 600-1000 °C temperature range [104, 163, 166, 169]. Horita *et al.* [171] has reviewed the optimized fuel and steam partial pressures for the different Ni/YSZ anode geometries. The authors proposed that the surface properties of Ni/YSZ anode materials could affect the mechanism. The evidences for the intermediates were observed by using secondary ion mass spectrometry (SIMS) [171].

There has been a limited amount of published results about the surface diffusion of adsorbed H_2 or H_2O species on Ni/YSZ anode systems. Their characteristics are restricted to computational analysis [104, 158, 162, 172]. Surface characteristics of Ni and Au are compared with respect to their inertness against reducing and oxidizing environment [103]. The surface diffusion of adsorbed H_2 or H_2O species on Au anodes would be expected to be lower than that on Ni/YSZ anodes at SOFC operating temperatures [103]. The effect of partial pressure of H_2O , a degrading agent on

Ni/YSZ systems, would not be expected on Au/YSZ systems due to the stability of Au in an oxidizing environment relative to Ni.

When D_2 is substituted for H_2 under identical SOFC operating conditions, the classical isotope effect would be proportional to the factor of 1.41 (the square root of ratio of the masses of D_2/H_2 or D^+/H^+). The activation energy difference between D_2 and H_2 is related to the bond enthalpies of these two fuels. These values are very similar in the SOFC temperature range. Norby *et al.* [173] has observed the factor of 1.25 as the isotope effect in Ni/YSZ electrode impedance at OCV in the temperature range of 600-800 °C, whereas no effect has been observed at 1000 °C or above. The authors have proposed that this shift in the isotope effect indicates a change in the nature of the rate limiting process at different temperatures. For example, at lower this is attributed to the surface diffusion involving hydrogen or protons [173].

Modeling studies offer significant benefits to interpret the experimental data of SOFC systems. The modeling studies from Bessler *et al.* [104] have explained the charge-transfer processes by examining patterned Ni anodes on a single crystal YSZ electrolyte. Their model has predicted that the rate limiting step is in the charge-transfer reactions during the two step H_2 species spillover mechanism from Ni surface to O^{2-} or OH^- group on the YSZ surface. Williford *et al.* [158, 174] have modeled Ni/YSZ anode supported single SOFC cell. The authors have proposed that in the high current density region, surface diffusion to reactive sites at the triple phase boundaries was responsible for the diffusion resistance observed in their system. They have also claimed that the competitive adsorption of fuel gases at the less reactive sites near triple phase boundaries would be another possible explanation for the

diffusion resistance. Zhu and Kee [105, 172] have explored and described the gas phase diffusion model for the species through porous SOFC electrodes to the reactive site near the triple phase boundaries. A distinguishing feature of the authors' studies has been their use of the dusty gas model, which provided the basic model for our system used to interpret the experimental data of porous Au anodes.

This study mainly focuses on distinguishing the effect of the three chemical and physical processes: (i) the charge-transfer, (ii) the surface diffusion of adsorbed species, and (iii) the water desorption. Each of these processes was identified as a possible limiting step in H_2 oxidation mechanism on porous Au anodes in Chapter 3. The results presented in this work clearly show that the diffusion of adsorbed H_2 and H_2O species on porous Au anodes would be two possible reactions that possibly dominate the H_2 oxidation mechanism. By utilizing four porous Au anodes with varying thicknesses from 30 μm to 120 μm , but with the identical porous Au-YSZ interface area, the effect of charge-transfer reactions is mainly eliminated from all four porous Au anodes. The interface area between the porous Au anode and the YSZ electrolyte defines the place where the charge-transfer reactions take place via H_2 spillover mechanism. The effect of porous Au anode thicknesses on diffusion processes is correlated with the H_2 partial pressures by using various H_2 fuel fractions. The various H_2 partial pressure experiments on the porous Au anodes with different thicknesses provide the basic trend for the thickness dependence of the diffusion processes by using polarization and electrochemical impedance measurements. The effect of water desorption on porous Au anodes is isolated by evaluating the performances of the same SOFC assembly using various H_2 partial

pressures humidified at room temperature. Isotopic labeling experiments with D₂ substituted for H₂ under the identical SOFC operating conditions reveal the fact that the trends in polarization and impedance measurements of porous Au anodes could be explained by the kinetic isotope effect. Lastly, the modeling studies of the same porous Au anodes corroborate the experimental data. The surface diffusion of the adsorbed fuel species is suggested as the primary phenomenon responsible for the experimental observations.

4.2. Experimental Section

The experimental setup and operating conditions of the SOFC were explained in Figure 2.1 of Chapter 2. Briefly, the membrane electrode assembly (MEA) for the SOFC was prepared on a polycrystalline YSZ disk (8 mole % yttria stabilized zirconia disk) with a 25.4 mm diameter and a 1.10-1.20 mm thickness, which was prepared in the laboratory by dye pressing and sintering at 1500°C for an hour. The LSM-YSZ was the cathode material, which was prepared as a viscous solution, applied by using a mask and then sintered by the consecutive heating processes (heated to 400 °C with the rate of 0.3 °C/min, sintered at 400 °C for an hour, then heated to 1300 °C with the rate of 1 °C/min, sintered at 1300 °C for an hour, and lastly, cooled to room temperature with the rate of 1 °C/min). Porous Au anodes with various thicknesses from 30 µm to 120 µm explained below were the only anodes employed in this study. The entire assembly was placed into a furnace after preparation of the SOFC assembly was completed. The measurements in this study

were performed at 785 ± 10 °C. The fuel flow was supplied to the anode by an inlet tube, and the cathode was exposed to air via another tube.

4.2.1 Preparation of porous Au anodes:

Viscous Au paste (Engelhard) was used as purchased to prepare porous Au anodes with different thicknesses. Four Au anodes with the specific porous Au thicknesses (i.e. 30, 60, 90 and 120 μm) and identical electrode-electrolyte interface areas were obtained by using a Kapton tape mask with a thickness of 100 μm . One layer of Kapton tape provides a thickness of ~ 30 μm to porous Au anodes after sintering and operating in the SOFC. The Kapton tape masks were layered to give the desired thickness. Then, these layered masks were put on a YSZ electrolyte disk. After applying different thicknesses of Au paste, the masks were removed and then the disk was dried for two hours at 230°C using a heat gun. Then, Au leads (AlfaAesar) were attached to each porous Au anode to provide electrical contacts by using small amount of Au paste. Subsequently, the whole assembly was glued to a ceramic tube by using ceramic paste and further sintered over night at 785°C under a flow of Ar-H₂ gas mixture (10 % H₂). A detailed experimental setup for the SOFC assembly was given in Chapter 2.

4.2.2 Arrangement of partial pressure of fuel and humidifying agent content:

The total gas flow consisted of fuel and diluent (Ar) gas with the purity of > 99.9 %. The total flow was adjusted with two computer controlled mass flow controllers. The total gas flow (total gas pressure = 1 atm) of 210 sccm of fuel and Ar gas mixture

on the anode side was used. The different partial pressure values of fuels, such as H₂ and D₂, were adjusted by changing the fraction of fuel in the total flow. The fuel partial pressure values with respect to the fraction of fuel flow were 14 sccm H₂: 0.067 atm; 70 sccm H₂: 0.333 atm; 140 sccm H₂: 0.667 atm in total fuel flow of 210 sccm balanced with Ar diluent gas. When necessary, the fuel flow was humidified by bubbling through water at room temperature.

4.2.3 Characterization Techniques:

A Gamry Instruments four-channel Frequency Response Analyzer (FRA) was employed for the polarization and electrochemical impedance spectroscopic measurements in the potentiostatic mode at open circuit over a frequency range from 100 kHz to 50 mHz. For the impedance measurements, the excitation voltage was constant at 10 mV. Gamry Echem Analyst software version 1.35 is used for fitting experimental EIS data. For the polarization measurements, linear scan voltammetry was utilized with a step size of 5 mV and with a scan rate of 5 mV/s. For all SOFC operations in this study, electrochemical measurements were performed at 785 ± 10 °C. SEM analyses were performed with an AMRAY 1820K Scanning Electron Microscope with an acceleration potential of 25kV.

4.3. Results

Four Au anodes with the thicknesses of 30, 60, 90, and 120 μm were fabricated on a YSZ disk as shown in Figure 4.1. The experiment of various thicknesses on porous Au anodes was designed to distinguish the effect of surface diffusion of H_2 adsorbed species on 3-D Au anode bulk, charge-transfer reactions and water desorption.

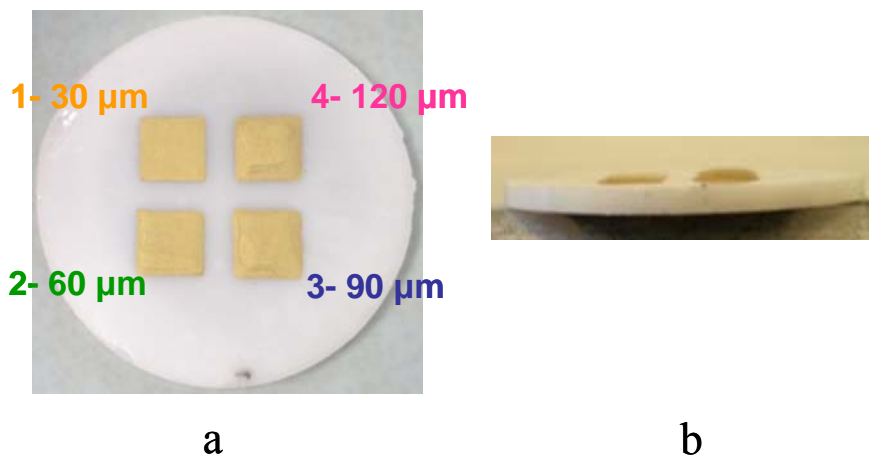


Figure 4.1: Experimental setup of porous Au anodes with four different thicknesses a) Top view, b) Cross-section of the SOFC assembly.

The sintering and operating processes are unlikely to create porosity and thickness divergence in porous Au anodes. Figure 4.2 shows the comparison of the scanning electron microscopy (SEM) images of Au anodes, which were obtained after *ca.* 72 hours operation in SOFC. Scanning electron microscopy was employed to evaluate thicknesses and porosities of porous Au anodes. Since the porous Au anodes were characterized by mounting the porous Au anodes after their removal from the electrolyte surface, the YSZ electrolyte does not appear in the SEM images. The SEM images of the top portion of the anode and the bottom portion of the anode that was attached to the YSZ electrolyte were used to illustrate the porosity differences for Au

anodes. The SEM images of the Au anode cross-sections are illustrated in the first column of Figure 4.2. The comparison of the top and bottom views of the entire set of Au anodes shows that the porosity of Au anodes with different thicknesses is identical. The pore sizes of Au anodes are in the range of 3-5 μm for top and bottom.

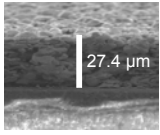
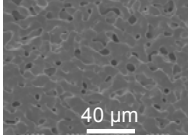
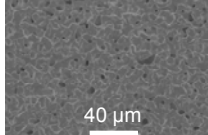
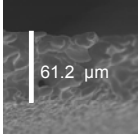
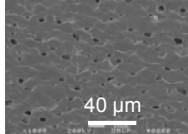
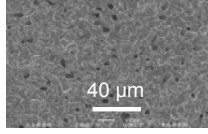
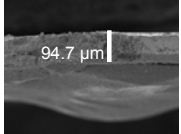
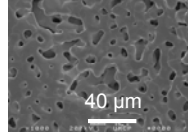
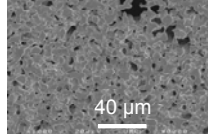
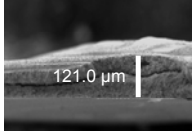
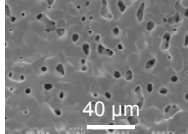
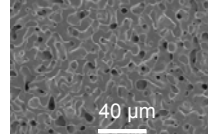
Electrode	Cross-section	Top view	Bottom view
30 μm			
60 μm			
90 μm			
120 μm			

Figure 4.2 SEM images of porous Au anodes with various thicknesses after 72 hours operation in SOFC.

4.3.1 The effect of dry H_2 partial pressures on porous Au anodes with different thicknesses in SOFC:

The experiments on porous Au anodes in Figure 4.1 with different H_2 partial pressures were designed to evaluate the effect of mass transport processes, such as gas phase, surface diffusion, and water desorption. Since the total gas pressure is 1 atm, the H_2 partial pressure was calculated from the ratio of the H_2 fuel flow to the total gas flow (210 sccm). Three different dry H_2 fuel fractions, which were at lower, 14 sccm, (0.067 atm), medium, 70 sccm, (0.333 atm), and higher, 140 sccm, (0.667

atm) fuel fractions of the total gas flow of 210 sccm (1 atm) balanced with Ar gas, were employed to examine the effect of the H₂ partial pressure on the polarization and impedance performances of porous Au anodes in operation of SOFC assembly. The polarization and impedance measurements were simultaneously recorded to avoid the potential and current gradients across the electrolyte and the cathode for four porous Au electrodes shown in Figure 4.1.

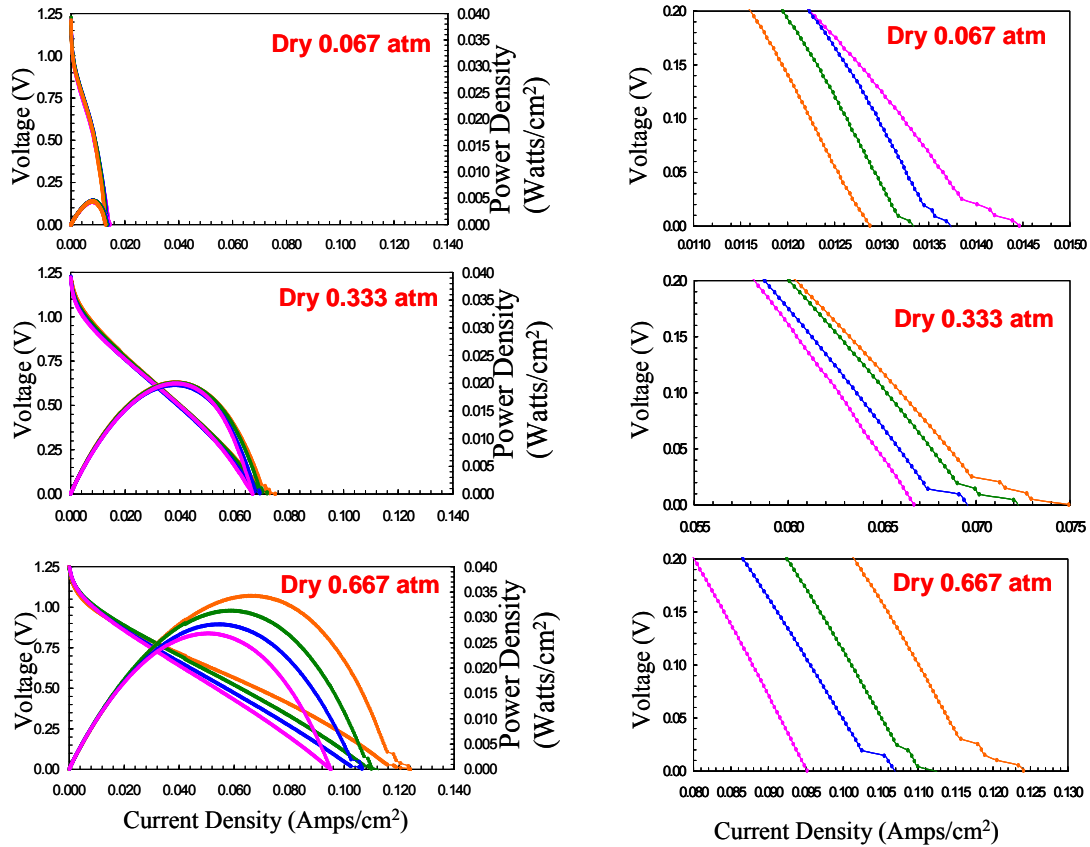


Figure 4.3 Polarization curves (normalized with respect to Au-YSZ interface area, 16 mm² for all four electrodes) of four different thicknesses porous Au anodes with various fuel fractions of **dry** H₂ **Left:** whole range of polarization curves, **Right:** details in maximum current density regions (**Orange:** 30 µm, **Green:** 60 µm, **Blue:** 90 µm, and **Magenta:** 120 µm).

The polarization curves of porous Au anodes with different dry H₂ fuel partial pressures are illustrated in Figure 4.3. The fuel conversion efficiencies are in the

range of 0.15-0.21 %. These are calculated by using the number of electrons from the experimental current values divided by the number of electrons from the H₂ input. These conversion values are extremely low as compared to the conventional SOFC anodes [36]. Since Au is known as a poor catalyst for H₂ oxidation under SOFC operating conditions, low fuel conversion is anticipated. Au anodes are preferred to differentiate the contribution of each H₂ oxidation step by changing one parameter on different Au anode geometries in the same SOFC assembly.

At low to medium fuel partial pressures, power densities are proportional to the Au anode and YSZ electrolytes interface areas, whereas this is not observed for the high fuel partial pressure. For low to medium fuel partial pressures (<0.333 atm), the change in thicknesses of porous Au anodes has virtually no effect on power densities, which are approximately 0.005 and 0.020 Watts/cm², respectively. At 0.667 atm high fuel partial pressure, power density values decrease with respect to increasing Au anode thickness, such as 0.034 Watts/cm² for the thinnest electrode and 0.027 Watts/cm² for the thickest electrode.

Table 4.1: Maximum current densities of porous Au anodes with dry H₂

Fuel Partial Pressure	30 μm	60 μm	90 μm	120 μm
0.067 atm Dry H ₂	13.0 mA/cm ²	13.5 mA/cm ²	14.0 mA/cm ²	14.5 mA/cm ²
0.333 atm Dry H ₂	75.0 mA/cm ²	72.0 mA/cm ²	69.0 mA/cm ²	66.5 mA/cm ²
0.667 atm Dry H ₂	124 mA/cm ²	112 mA/cm ²	107 mA/cm ²	95.0 mA/cm ²

For the medium and high fuel partial pressures, the thinnest electrode has the highest, and the thickest has the lowest maximum current densities given in Table 4.1. However, for the low fuel partial pressures the thickest has 14.5 mA/cm² and the thinnest has 13.0 mA/cm² current densities.

The overpotential applied between the anode and the cathode is the electrical driving force for the anodic processes. It is used to adjust the fuel cell to a specific operating condition on the polarization curve as explained in Chapter 1, Fig. 1.3. At certain overpotential values, different types of chemical and physical processes are dominant and described by changing parameters in the SOFC assembly. The electrochemical impedance curves at the range of high current regime overpotential of Au anodes with various H_2 partial pressures are shown in Figure 4.5. With respect to the polarization curves in Figure 4.3, the 1 V overpotential (at 0.2-0.25 V cell voltage), according to the open circuit voltage (OCV) range of 1.20 V for 0.067 atm to 1.25 V for 0.667 atm, is chosen to address the effect of mass transport processes on SOFC impedance curves.

The equivalent circuit in Figure 4.4 is employed to fit the EIS data of Au anodes. This circuit is a modified version of a common circuit model employed by Sukeshini *et al.* [175] and Bieberle *et al.* [110]. Two RQ elements for the anode processes are adopted to fit the experimental impedances and to evaluate the charge-transfer and mass transport processes, such as surface diffusion.

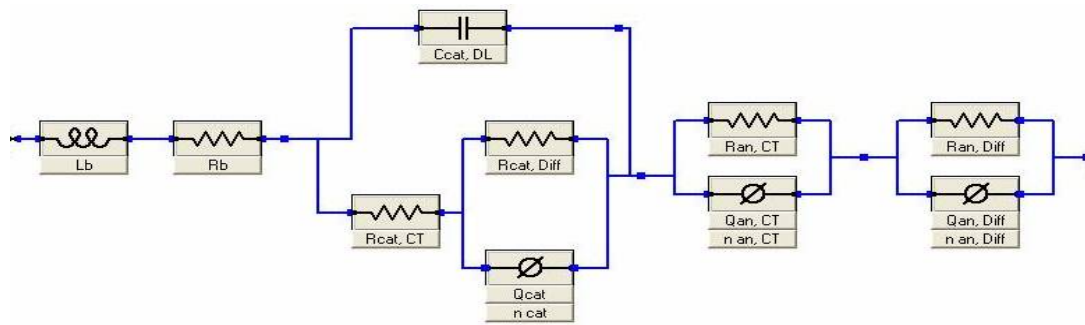


Figure 4.4 Equivalent circuit used to fit the electrochemical impedances.

The inductance, L_b , and the bulk resistance, R_b , are in series and related to processes on the connecting leads and electrolyte. The cathode associated circuit elements are the cathode double layer capacitance, $C_{cat, DL}$, the cathode charge-transfer resistance, $R_{cat, CT}$, which are connected in parallel; the cathode diffusion resistance, $R_{cat, Diff}$, and the constant phase element (CPE), $Q_{cat Diff}$, which are connected in parallel and in series to $R_{cat, CT}$. The impedance of CPE is given by $Z_{CPE} = 1/Q(i\omega)^n$, where i the imaginary unit, ω is the angular frequency, and n is the deviation of impedance of CPE from the ideal capacitive behavior ($n=1$ for the impedance of a capacitor, $n=0$ for the impedance of a resistor, and $n \approx 0.5$ for the impedance of a surface diffusion).

There are two parallel RQ elements for anode processes, which are connected in series. The first RQ is added to distinguish the charge-transfer and consists of the anode charge transfer resistance, $R_{an, CT}$, and the constant phase element, $Q_{an CT}$. The second parallel RQ is associated with diffusion processes on the anode surface, which are $R_{an, Diff}$, and the constant phase element, $Q_{an Diff}$. The bulk and cathode portion of EIS data are assumed to be constant for the entire polarization range. EIS parameters of the bulk and the cathode from Sukeshini *et al.* [175] are employed for fitting the EIS data to distinguish the anode related processes and these values and details of fits are given in the Appendix.

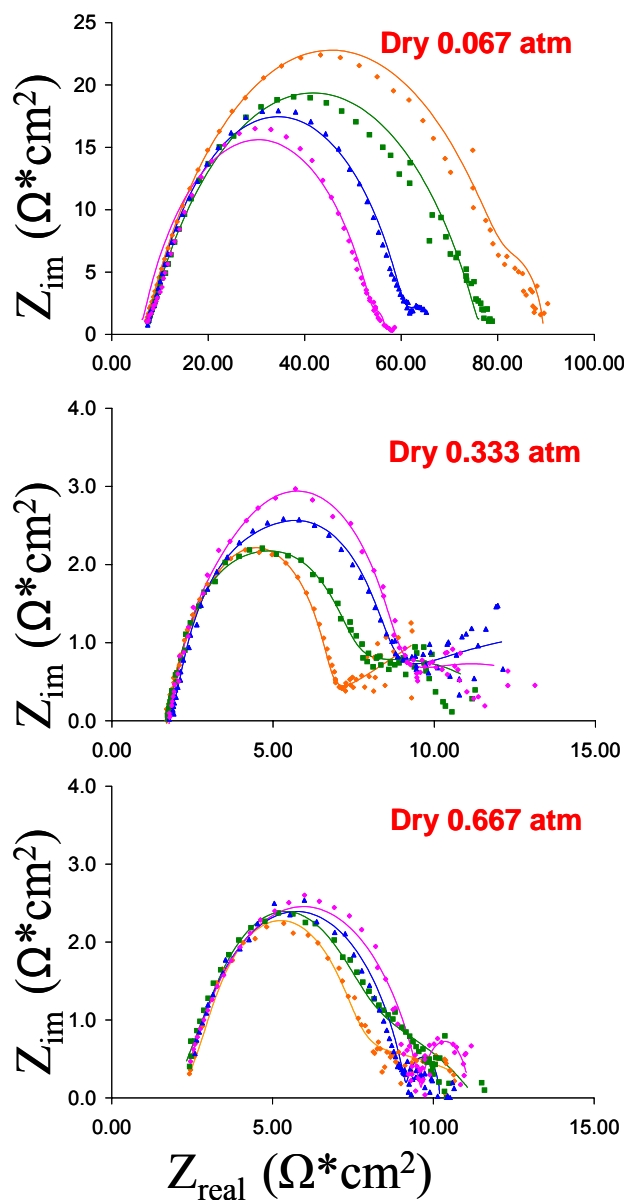


Figure 4.5 Impedance curves at 1V overpotential (normalized with respect to Au-YSZ interface area, 16 mm² for all four electrodes) of four different thicknesses porous Au anodes with various fuel fractions of dry H₂ (Orange: 30 μm , Green: 60 μm , Blue: 90 μm , and Magenta: 120 μm) Symbols are experimental data and lines are data from equivalent circuit fits.

The electrochemical impedance spectra of Au anodes at 1V overpotential and the equivalent circuit fits of Au anodes are illustrated in Figure 4.5. At 0.067 atm fuel partial pressure, the thinnest electrode has a larger total resistance, R_T , than other electrodes. Between the medium and high fuel partial pressures, the trends, values,

and shapes of electrochemical impedances of porous Au anodes are similar. The thinnest electrode has smaller total resistance, R_T , values at 0.333 and 0.667 atm than other electrodes. All anodes for medium and high fuel partial pressures have two arcs in EIS curves. These trend changes between low and medium dry fuel partial pressures are observed also in polarization curves in Figure 4.3.

Table 4.2: Summary of EIS spectra fitting parameters at high current region for various thickness porous Au anodes with different dry H_2 fuel partial pressures.

Fuel Partial Pressure	Parameters	30 μm	60 μm	90 μm	120 μm
0.067 atm Dry H_2	$R_{an, CT} (\Omega \cdot cm^2)$	6.8	6.5	6.4	6.1
	$R_{an, Diff} (\Omega \cdot cm^2)$	79.1	67.3	52.8	45.3
0.333 atm Dry H_2	$R_{an, CT} (\Omega \cdot cm^2)$	2.1	2.2	2.2	2.3
	$R_{an, Diff} (\Omega \cdot cm^2)$	5.1	6.6	7.5	7.5
0.667 atm Dry H_2	$R_{an, CT} (\Omega \cdot cm^2)$	2.1	2.3	2.4	2.2
	$R_{an, Diff} (\Omega \cdot cm^2)$	6.5	6.5	6.4	7.0

Table 4.2 gives the EIS fitting parameters for the charge-transfer and diffusion resistances of Au anodes under dry fuel partial pressures. For each fuel partial pressure, the charge-transfer resistances, $R_{an, CT}$, of Au anodes are in the same range within experimental error. The $R_{an, CT}$ values decrease with increasing H_2 partial pressures due to the enhancement in the amount of surface H_2 species at the interface. The range of $R_{an, CT}$ values are 6.8-6.1 $\Omega \cdot cm^2$ at dry 0.067 atm, 2.1-2.3 $\Omega \cdot cm^2$ at dry 0.333 atm, and 2.1-2.4 $\Omega \cdot cm^2$ at dry 0.667 atm. The $R_{an, CT}$ values are in the deviation ranges of 10 % between different thicknesses for each fuel partial pressure.

The diffusion resistances, $R_{an, Diff}$, follow the trends observed in the polarization curves in Figure 4.3. $R_{an, Diff}$ are composite resistances of surface diffusion of various adsorbed species on bulk Au and YSZ, such as hydrogen and water. For the low fuel partial pressure, $R_{an, Diff}$ values decrease with increasing electrode thickness, from

79.1 $\Omega \cdot \text{cm}^2$ to 45.3 $\Omega \cdot \text{cm}^2$. This trend in $R_{\text{an, Diff}}$ values dictates the trends in the maximum current densities for the low dry fuel partial pressure as observed in Figure 4.3. $R_{\text{an, Diff}}$ is the combined resistances of surface diffusion processes.

The dependence of $R_{\text{an, Diff}}$ on the thickness of Au anodes with various dry fuel partial pressures is illustrated in Figure 4.6. $R_{\text{an, Diff}}$ values from equivalent circuit fits are linear with respect to the thickness of porous Au anodes at each dry fuel partial pressure. For the medium to high dry fuel partial pressures, the changes in $R_{\text{an, Diff}}$ values with respect to the thickness of porous Au anodes are \sim zero according to the slopes of the curves in Figure 4.6. For the 0.333 and 0.667 atm dry fuel partial pressures.

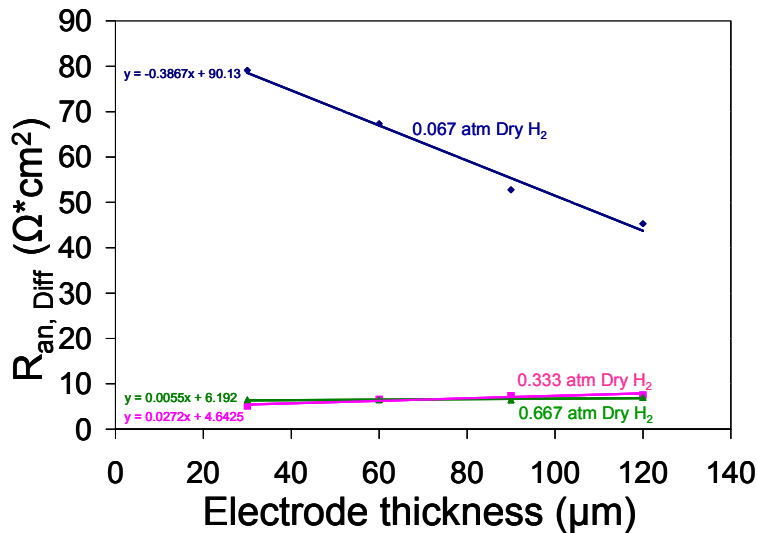


Figure 4.6 The plot of Au anode thicknesses vs. $R_{\text{an, Diff}}$ values at 1V overpotential from equivalent circuit fits with various dry H_2 fuel partial pressures.

Figure 4.7 shows an $R_{\text{an, Diff}}$ dependence on partial pressure of dry H_2 fuel, $p(\text{H}_2)$, for the four Au anodes. The fuel partial pressures are calculated by the ratio of H_2 flow (14-70-140 sccm) to the total gas flow (210 sccm). Since the total pressure is 1

atm, this ratio directly provides the H_2 partial pressures, $p(H_2)$, which are 0.067, 0.333, and 0.667 atm, respectively.

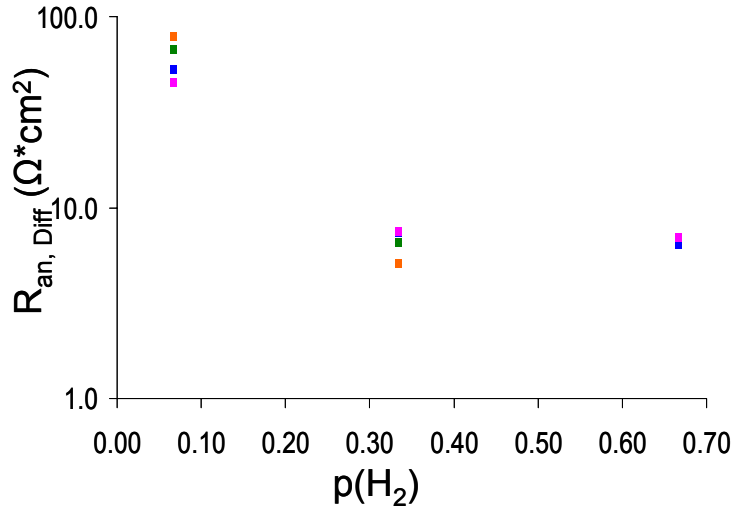


Figure 4.7 The plot of $p(H_2)$ vs. $R_{an, Diff}$, H_2 partial pressure dependence of $R_{an, Diff}$ at 1 V overpotential from equivalent circuit fits with various dry H_2 fuel fractions (**Orange**: 30 μm , **Green**: 60 μm , **Blue**: 90 μm , and **Magenta**: 120 μm).

4.3.2 The effect of water on Au anodes with varying partial pressures of H_2 :

The same SOFC assembly used for the dry fuel experiments was examined in order to distinguish the surface diffusion and desorption effects of water on the polarization and impedance of the four Au anodes by adding 3 % water to the total fuel flow. The fuel content was humidified by passing it through a water bubbler at room temperature. The amount of water is preferred due to its conventional use in SOFC operations with H_2 and hydrocarbon fuels.

The polarization curves of Au anodes with constant 3 % water are shown in Figure 4.8. For the low to medium wet H_2 fuel partial pressures, the power density values are not affected by water content as compared to dry H_2 experiments. For the low to medium fuel partial pressures (<0.333 atm) with 3 % water the power densities for

the low and medium fuel partial pressures are 0.005 Watts/cm² and 0.020 Watts/cm², respectively. These power density values are identical with dry H₂ experiments. For the high fuel partial pressure, the power density values are lower than for dry H₂ experiments for the high fuel partial pressure, 0.029 Watts/cm² for the thinnest and 0.020 Watts/cm² for the thickest. The maximum current density region for the low to medium fuel partial pressures is also shown in Figure 4.8, respectively.

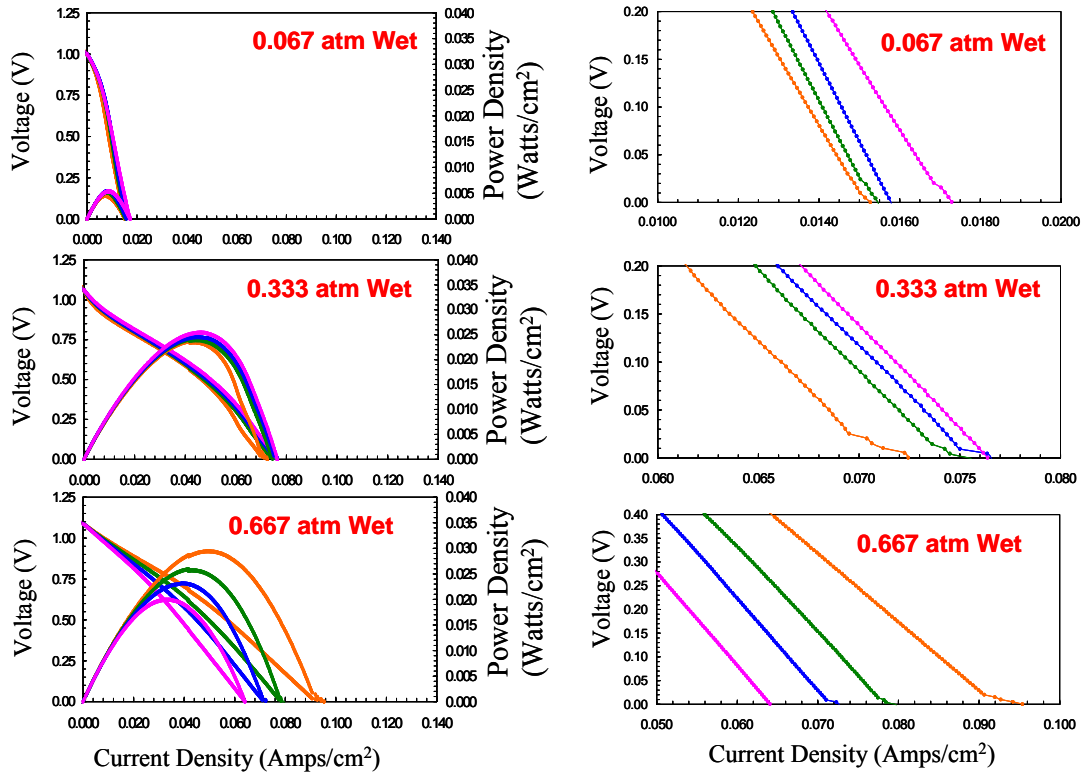


Figure 4.8 Polarization curves (normalized with respect to Au-YSZ interface area, 16 mm² for all four electrodes) of four Au anodes with various fuel fractions of **wet** H₂ **Left:** whole range of polarization curves, **Right:** details in maximum current density regions (**Orange:** 30 μm, **Green:** 60 μm, **Blue:** 90 μm, and **Magenta:** 120 μm).

For the low and medium fuel partial pressures with 3% water the thickest electrode has a higher maximum current density than the thin electrodes as was observed in the low flow dry H₂ case. However, for the high fuel partial pressure with 3% water this

trend is reversed and the thinnest electrode has a higher current density than the thickest electrode.

Table 4.3: Maximum current densities of porous Au anodes with wet H₂.

Fuel Partial Pressure	30 μm	60 μm	90 μm	120 μm
0.067 atm Wet H ₂	15.2 mA/cm ²	15.4 mA/cm ²	15.8 mA/cm ²	17.2mA/cm ²
0.333 atm Wet H ₂	72.4 mA/cm ²	75.0 mA/cm ²	76.0 mA/cm ²	76.2 mA/cm ²
0.667 atm Wet H ₂	95.1 mA/cm ²	79.2 mA/cm ²	72.2 mA/cm ²	64.0 mA/cm ²

The maximum current densities for the four Au anodes and wet H₂ fuel are given in Table 4.3. When the maximum current densities for the wet H₂ cases are compared with that of the dry H₂ cases, at 0.067 atm, the identical trend with respect to the dry case is observed. The maximum current density of the thickest electrode is higher than that of the thinnest electrode, 15.2 and 17.2 mA/cm², respectively. Interestingly, the maximum current densities of the 90 and 120 μm electrodes for the medium to high fuel partial pressures of wet H₂ decrease from 76.0 to 72.2 mA/cm² for 90 μm electrode and 76.2 to 64.0 mA/cm² for 120 μm electrode.

Figure 4.9 shows the electrochemical impedance spectra at 1 V overpotential and equivalent circuit fits of four Au anodes with various wet fuel partial pressures. For the low to medium wet fuel partial pressures, the thinnest Au anode has the highest R_T values, whereas for the high wet fuel partial pressure has the lowest R_T values. Only for the medium wet fuel partial pressure, two arcs in impedance are clearly observed, which can be assigned as the charge-transfer resistance for the high frequency side and the diffusion resistance for the low frequency side.

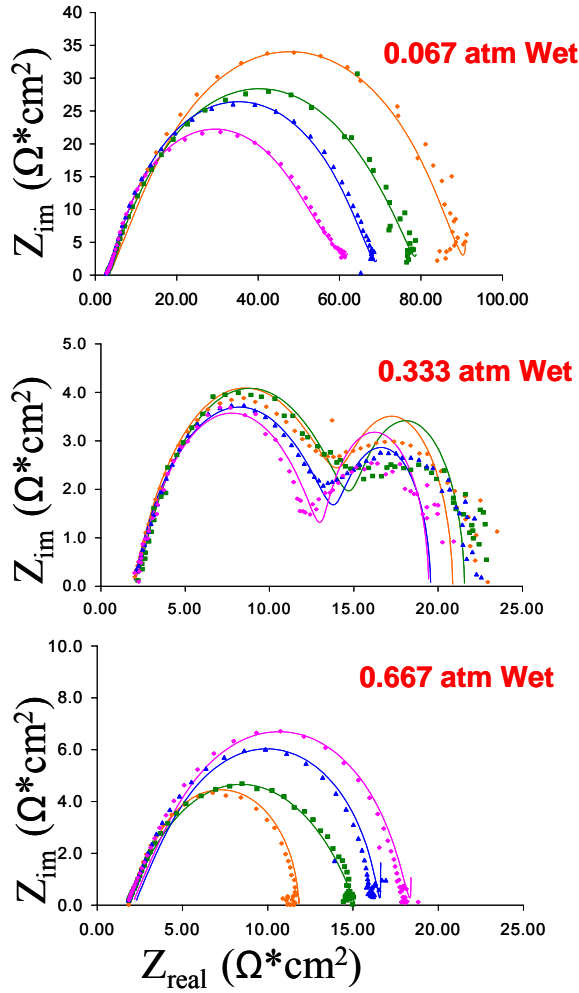


Figure 4.9 Impedance curves at the 1V overpotential (normalized with respect to Au-YSZ interface area, 16 mm² for all four electrodes) of four Au anodes with various fuel fractions of **wet** H₂ (**Orange**: 30 μm, **Green**: 60 μm, **Blue**: 90 μm, and **Magenta**: 120 μm) Symbols are experimental data and lines are data from equivalent circuit fits.

Table 4.4: Summary of EIS spectra fitting parameters at high current region for Au anodes with different wet H₂ fuel fractions.

Fuel Partial Pressure	Parameters	30 μm	60 μm	90 μm	120 μm
0.067 atm Wet H ₂	$R_{an, CT} (\Omega \cdot cm^2)$	1.4	1.4	1.1	0.9
	$R_{an, Diff} (\Omega \cdot cm^2)$	83.3	73.9	63.8	55.1
0.333 atm Wet H ₂	$R_{an, CT} (\Omega \cdot cm^2)$	3.6	3.8	3.9	3.7
	$R_{an, Diff} (\Omega \cdot cm^2)$	15.5	15.1	14.5	14.1
0.667 atm Wet H ₂	$R_{an, CT} (\Omega \cdot cm^2)$	0.7	0.8	0.7	0.8
	$R_{an, Diff} (\Omega \cdot cm^2)$	9.0	12.1	13.1	14.8

Equivalent circuit fitting parameters of $R_{an, CT}$ and $R_{an, Diff}$ in electrochemical impedance measurements of the four Au anodes with various wet fuel partial pressures are summarized in Table 4.4.

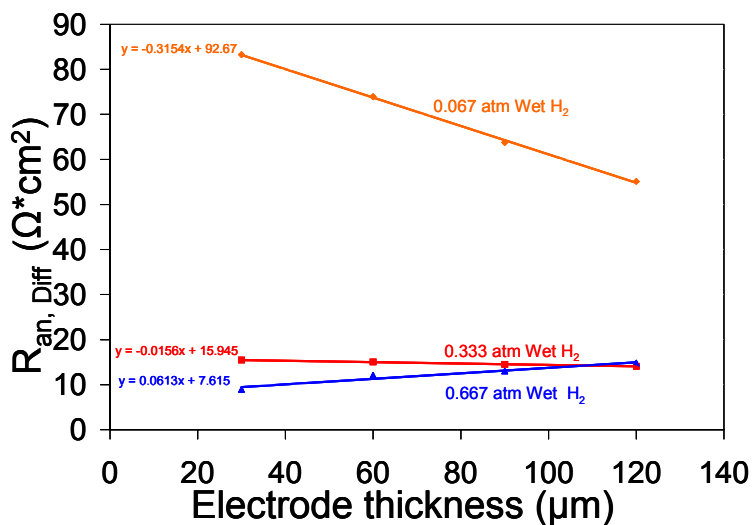


Figure 4.10 The plot of Au anode thicknesses vs. $R_{an, Diff}$ at 1V overpotential from equivalent circuit fits with various wet H_2 fuel fractions.

Figure 4.10 shows the dependence of $R_{an, Diff}$ on the thickness of porous Au anodes with various wet fuel partial pressures. The $R_{an, Diff}$ values from equivalent circuit fits are again linear with respect to the thickness of Au anodes for each wet fuel partial pressure. For the medium to high wet fuel partial pressures, the changes in $R_{an, Diff}$ values with respect to the thickness of porous Au anodes are relatively slight as observed from the slopes of the curves in Figure 4.10. For the high wet fuel partial pressures, $R_{an, Diff}$ values increase slightly with increasing the porous Au anode thicknesses. However, the $R_{an, Diff}$ values decrease with respect to anode thicknesses for the 0.067 and 0.333 atm wet H_2 partial pressures.

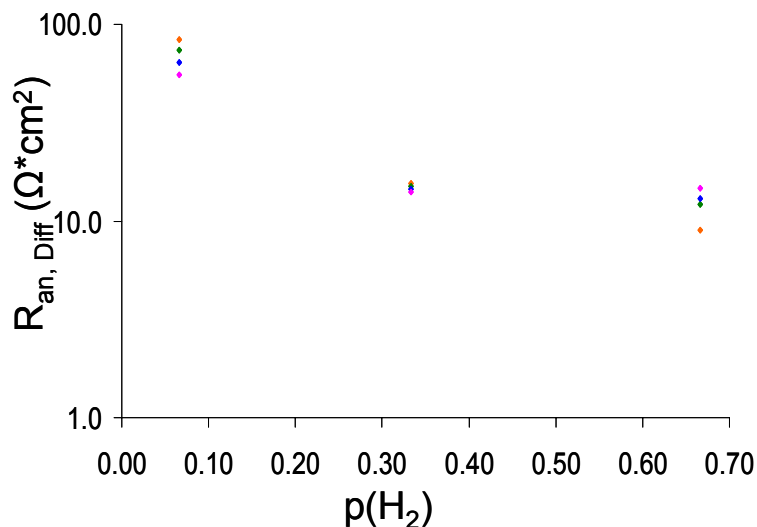


Figure 4.11 The plot of $p(\text{H}_2)$ vs. $R_{\text{an, Diff}}$, H_2 partial pressure dependence of $R_{\text{an, Diff}}$ at 1 V overpotential from equivalent circuit fits with various wet H_2 fuel fractions (**Orange**: 30 μm , **Green**: 60 μm , **Blue**: 90 μm , and **Magenta**: 120 μm).

The dependence of $R_{\text{an, Diff}}$ on partial pressure of dry H_2 fuel, $p(\text{H}_2)$, for four Au anodes is presented in Figure 4.11, which is discussed in Section 4.4.2.

4.3.3 The comparison of isotopically labeled D_2 fuels with H_2 fuel on porous Au anodes with different thicknesses:

The SOFC assembly as shown in Figure 4.1 was fabricated to differentiate the effect of the surface diffusion of adsorbed species of the isotopically labeled D_2 fuel on Au anodes with four different thicknesses.

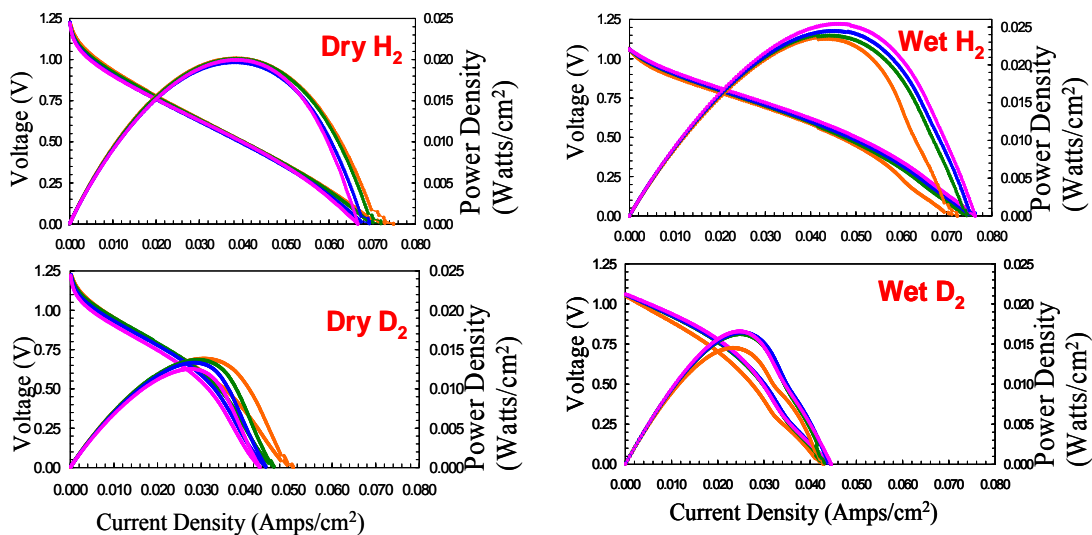


Figure 4.12 Polarization curves (normalized with respect to Au-YSZ interface area, 16 mm² for each) of four different thicknesses porous Au anodes with dry and wet H₂, isotopically labeled D₂ (Orange: 30 μm, Green: 60 μm, Blue: 90 μm, and Magenta: 120 μm).

Figure 4.12 illustrates the polarization curves of the four porous Au anodes with H₂, isotopically labeled D₂ fuel for the 70 sccm (0.333 atm) fuel partial pressures for each fuel.

Table 4.5: Maximum current densities of porous Au anodes with H₂ and D₂.

Fuel Partial Pressures	30 μm	60 μm	90 μm	120 μm
0.333 atm Dry H ₂	75.0 mA/cm ²	72.0 mA/cm ²	69.0 mA/cm ²	66.5 mA/cm ²
0.333 atm Dry D ₂	51.1 mA/cm ²	46.6 mA/cm ²	44.8 mA/cm ²	43.4 mA/cm ²
0.333 atm Wet H ₂	72.4 mA/cm ²	75.0 mA/cm ²	76.0 mA/cm ²	76.2 mA/cm ²
0.333 atm Wet D ₂	42.9 mA/cm ²	43.2 mA/cm ²	44.5 mA/cm ²	44.7 mA/cm ²

The maximum current densities of porous Au anodes with various thicknesses under dry and wet H₂ and D₂ fuel are presented in Table 4.5 to distinguish the isotope effect in the oxidation reaction of fuel on porous Au anodes. The range of maximum

current densities is 75.0-66.5 mA/cm² for 0.333 atm (70 sccm) dry H₂ fuel and 51.1-43.4 mA/cm² for dry D₂ fuel.

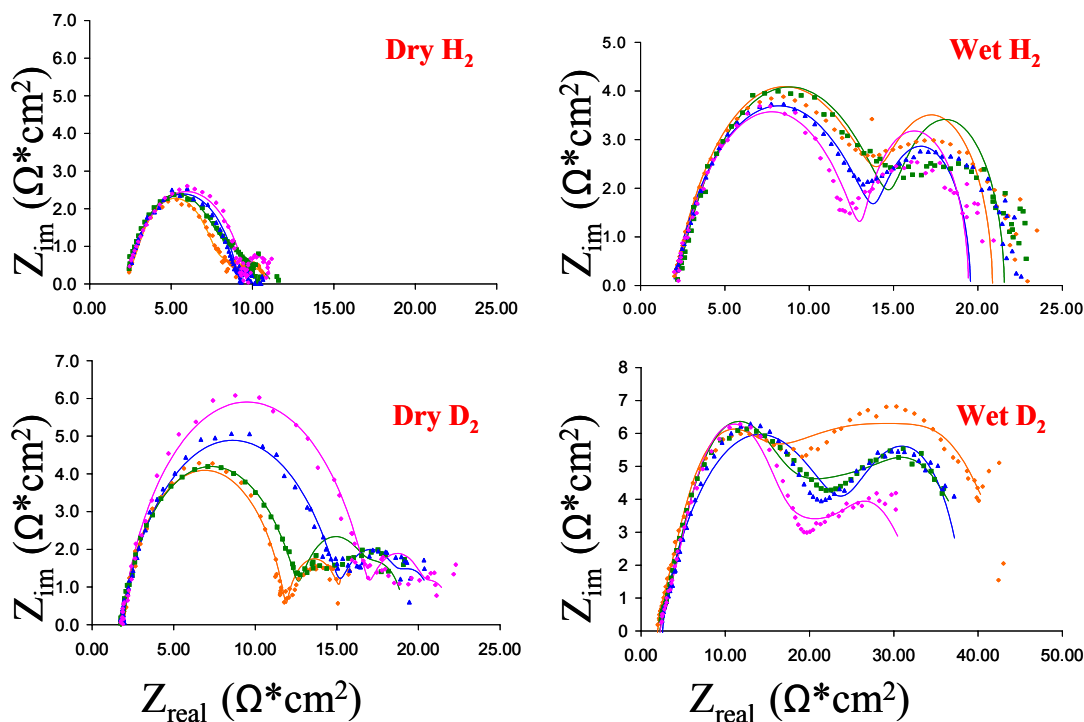


Figure 4.13 Impedance curves at 1V overpotential (normalized with respect to Au-YSZ interface area, 16 mm² for all four electrodes) of four different thicknesses porous Au anodes with dry/wet H₂ and D₂ at 70 sccm fuel fraction (Orange: 30 μm, Green: 60 μm, Blue: 90 μm, and Magenta: 120 μm) Symbols are experimental data and lines are data from equivalent circuit fits. (Note: the graph depicting the wet D₂ impedance is shown with different scales for aesthetic purposes)

The EIS data at the high current region and equivalent circuit fits of four different thickness porous Au anodes with dry/wet H₂ and D₂ fuels are displayed in Figure 4.13. Two separate arcs, which are the charge-transfer resistance at high frequency side and the diffusion resistance on the low frequency side in the electrochemical impedance curves, are clearly observed for every case of dry and wet H₂ and D₂ fuels on porous Au anodes with various thicknesses. The thickest anode has the lowest R_T values for the wet cases of H₂ and D₂ fuels, and the highest R_T values for the cases of dry H₂ and D₂ fuels.

Table 4.6 gives a quantitative summary of equivalent circuit fitting parameters of $R_{an, CT}$, and $R_{an, Diff}$, for the porous Au anodes with various thicknesses under both dry and wet H_2 and D_2 fuels in Figure 4.12.

Table 4.6: Summary of the equivalent circuit fitting parameters of EIS spectra at 1 V overpotential for Au anodes with dry and wet H_2 and D_2 fuels.

Fuel Partial Pressure	Parameters	30 μm	60 μm	90 μm	120 μm
0.333 atm Dry H_2	$R_{an, CT} (\Omega \cdot cm^2)$	2.1	2.2	2.2	2.3
	$R_{an, Diff} (\Omega \cdot cm^2)$	5.1	6.6	7.5	7.6
0.333 atm Dry D_2	$R_{an, CT} (\Omega \cdot cm^2)$	2.5	2.3	2.6	2.2
	$R_{an, Diff} (\Omega \cdot cm^2)$	9.7	12.2	14.2	15.5
0.333 atm Wet H_2	$R_{an, CT} (\Omega \cdot cm^2)$	3.6	3.7	3.8	3.7
	$R_{an, Diff} (\Omega \cdot cm^2)$	14.4	15.1	15.8	16.1
0.333 atm Wet D_2	$R_{an, CT} (\Omega \cdot cm^2)$	7.4	7.3	7.2	7.4
	$R_{an, Diff} (\Omega \cdot cm^2)$	37.6	33.7	29.8	25.5

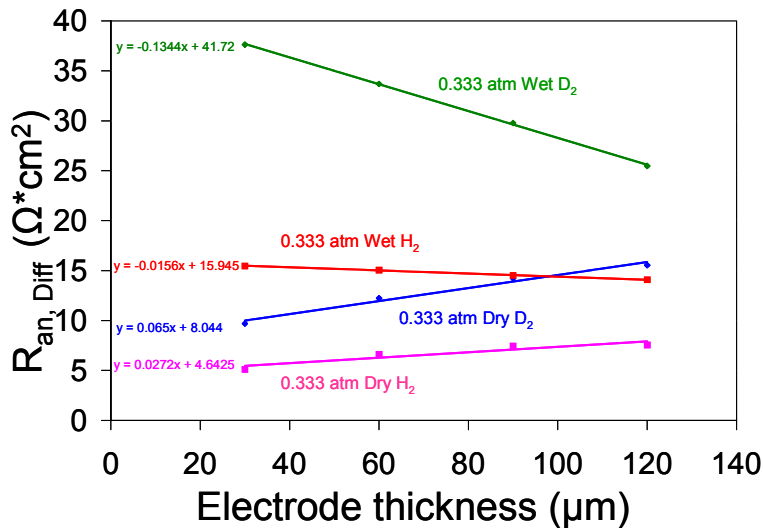


Figure 4.14 Porous Au anode thicknesses vs. $R_{an, Diff}$ values from equivalent circuit fits with 70 sccm dry/wet H_2 - D_2 flows.

The dependence of $R_{an, Diff}$ on the thickness of Au anodes is presented in Figure 4.14. The linearity of each set of $R_{an, Diff}$ values with respect to the thickness of porous Au anodes arises from each fuel flow composition. At 0.333 atm dry H_2 and D_2 fuel

partial pressures, the $R_{an, Diff}$ values with respect to the thickness of porous Au anodes increase slightly as can be observed from the slopes of the curves in Figure 4.14.

4.3.4 Modeling studies of four different thicknesses porous Au anodes with various fuel partial pressures of H_2 :

To glean a better understanding of the electrochemical behavior of porous Au anodes in SOFC, a new approach developed by Bessler *et al.* [104] was employed with the aim to correlate directly the experimental polarization data with the chemical and the electrochemical equations characterizing the system. Due to the geometrical complexity of the porous Au electrodes, simplified model electrode systems, such as Au metal, H_2 gas, and YSZ systems were studied at first. The simulations were based on the dependence of thermodynamic and kinetic properties of electrochemical reactions in porous Au anode systems. The details concerning the application to SOFC systems are addressed by comparing the experimental and simulated data.

The model employed in this study was a 1-D isothermal SOFC model developed in University of Maryland SOFC group. This model incorporates the effects of gas phase diffusion, surface diffusion, adsorption-desorption reactions, charge-transfer reactions, and ohmic processes. The gas phase diffusion rates are calculated using the dusty gas model, which was described elsewhere [105, 172]. The equation for this model is:

$$N_g(k) = -\sum_l (D_{DGM}(k, l) \nabla [X(l)]) - \sum_l \left(\frac{D_{DGM}(k, l) [X(l)]}{D_{Kn}^e(l)} \right) \frac{B_g}{\mu} \nabla P \quad 4.1$$

where $N_g(k)$ is the molar flux per unit area of species k ; $D_{DGM}(k, l)$ is the dusty gas model diffusion coefficient for species k and l ; $[X(l)]$ is the molar concentration of

species l ; $D_{Kn}^e(l)$ is the effective Knudsen diffusion coefficient of species l ; B_g is the permeability of the porous electrode; μ is the viscosity; P is the pressure. The surface diffusion rates of adsorbed species on anode surfaces are calculated according to the following equation:

$$N_{surf}(k) = \Gamma D_{surf}(k) \frac{\Delta\theta(k)}{\Delta x} \quad 4.2$$

where $N_{surf}(k)$ is the surface diffusion rate for species k ; Γ is the total surface site concentration of available surface sites on anode; $D_{surf}(k)$ is the surface diffusion coefficient of species k ; $\theta(k)$ is the surface site fraction of species k ; x is the surface diffusion distance to triple phase boundary (TPB). Adsorption and desorption reaction rates are calculated according to law of mass-action kinetics:

$$Reaction\ Rate = k_f \Pi[X_r] - k_b \Pi[X_p] \quad 4.3$$

where k_f is the rate constant for forward reaction; $[X_r]$ is the molar concentration of reactants; k_b is the rate constant for the reverse reaction; $[X_p]$ is the molar concentration of products. The charge-transfer reaction rates with respect to Faradaic current density, i_{Far} , are calculated according to the Butler-Volmer equation [76]:

$$i_{Far} = i_0 \left[\exp\left(\frac{\beta_f n F \eta}{RT}\right) - \exp\left(\frac{-\beta_b n F \eta}{RT}\right) \right] \quad 4.4$$

where i_0 is the exchange current density; n is the number of electrons transferred per mole of fuel; β_f and β_b are the forward and backward symmetry factors, respectively; and F is the Faraday constant. The ohmic processes are governed according to Ohm's law:

$$\Delta V = iR \quad 4.5$$

where ΔV is the potential; i is the current; R is the resistance. The model employed in this study is the transient model that integrates over a long time period to find the steady-state.

Figure 4.15 illustrates the model SOFC assembly used in this study. Since, the surface diffusion length scale is smaller than the anode thicknesses, the model in this study assumes that all the non-equilibrium chemistry occurs at the 2-D interface between porous Au and YSZ electrolyte, which is indicated by the red rectangular area in Figure 4.15.

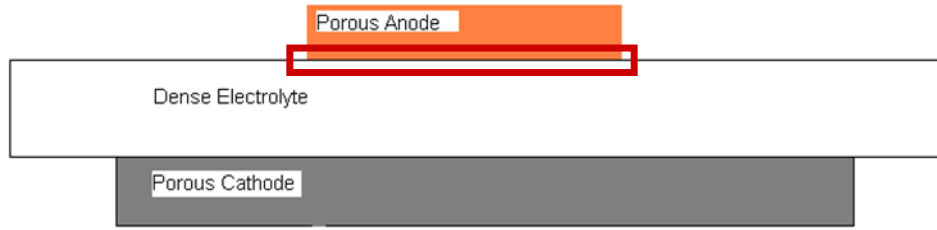


Figure 4.15 Schematic representation of SOFC assembly employed in modeling studies.

The set of parameters for anode modeling studies is given in Table 4.7. All the cathode parameters are taken from the modeling studies for the LSM-YSZ cathodes previously performed in the University of Maryland SOFC group.

SEM images in Figure 4.2 provide information about the porosity, Φ_g , the average pore radius, r_p , and the average particle diameter, d_p , of the porous Au anodes, which are directly extrapolated by measuring the sizes on SEM images. The tortuosity, τ_g , value is employed as a reasonable value taken from literature. The active catalyst area per unit geometric area, A_{cat} , and the active electrolyte area per unit geometric area, A_{elec} , values are fitted manually. The triple phase boundary length per unit geometric area, L_{tpb} , value is calculated from A_{cat} divided by r_p . Finally, both triple phase

boundary widths such as on the catalyst surface, $w_{tpb,cat}$, and on the electrolyte surface, $w_{tpb,elec}$, as well as all the surface diffusion coefficients are adjusted to give the best correspondence between the experimental data from the four Au anodes with various dry H_2 and D_2 fuels and model results.

Table 4.7: Summary of modeling parameters used in this study.

	Anode		Cathode
L_{tpb} per unit geometric area [1/m]	3e4		3e6
Total electrode thickness [μm]	As per experiment		30
Φ_g Porosity	0.25		0.35
τ_g Tortuosity	5		4
r_p Average pore radius [μm]	2		0.5
d_p Average particle diameter [μm]	4		2.5
A_{cat} Active catalyst area per unit geometric area	0.06		1
A_{elec} Active electrolyte area per unit geometric area	0.06		1
$w_{tpb,cat}$ the width of the three phase boundary on the catalyst surface [nm]	20		20
$w_{tpb,elec}$ the width of the three phase boundary on the electrolyte surface [nm]	20		20
$D_{surf,cat}$ surface diffusion coefficients on the catalyst surface [m^2/s]	14 sccm	70 and 140 sccm	O on LSM—6.02e-8
	H on Au—1.87e-7	H on Au—3.61e-7, D on Au—2.56e-7	
$D_{surf,elec}$ surface diffusion coefficients on the electrolyte surface [m^2/s]	O ²⁻ on YSZ—1e-8 OH ⁻ on YSZ—8e-9		O ²⁻ on YSZ—1e-8

Using the parameters given in Table 4.7, Figure 4.16 shows a comparison between the model simulations and the empirical polarization data from the porous Au anodes with various dry H_2 fuel partial pressures. To avoid confusion between the four different thicknesses, only the thinnest, 30 μm and the thickest, 120 μm , anodes are presented.

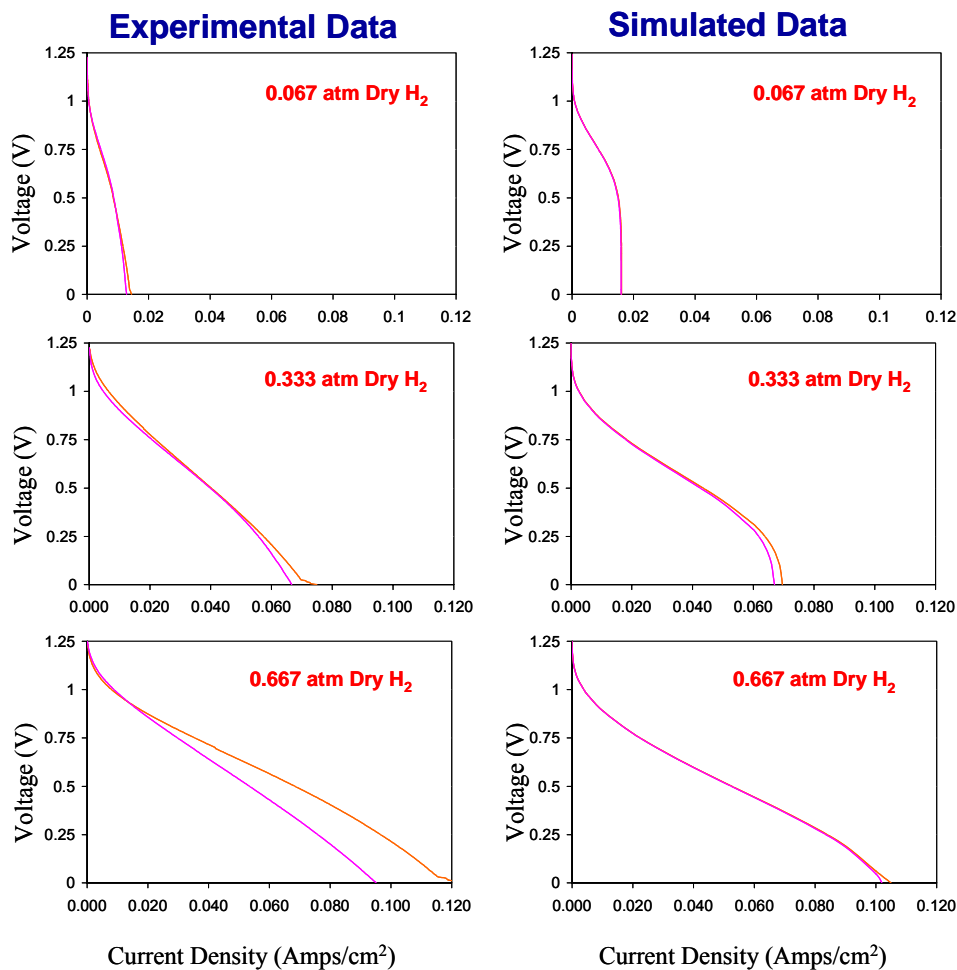


Figure 4.16 Comparison of experimental and simulated data from different thickness porous Au anodes with various dry H_2 fuel fractions (**Orange**: 30 μm and **Magenta**: 120 μm).

Figure 4.17 shows the comparison of experimental and simulated polarization data with dry 70 sccm (0.333 atm) H_2 and D_2 fuel flows. The simulated polarization curves in Figure 4.17 are obtained with dry D_2 fuel partial pressure by addition of the isotope effect to $D_{surf, cat}$ values in Table 4.7.

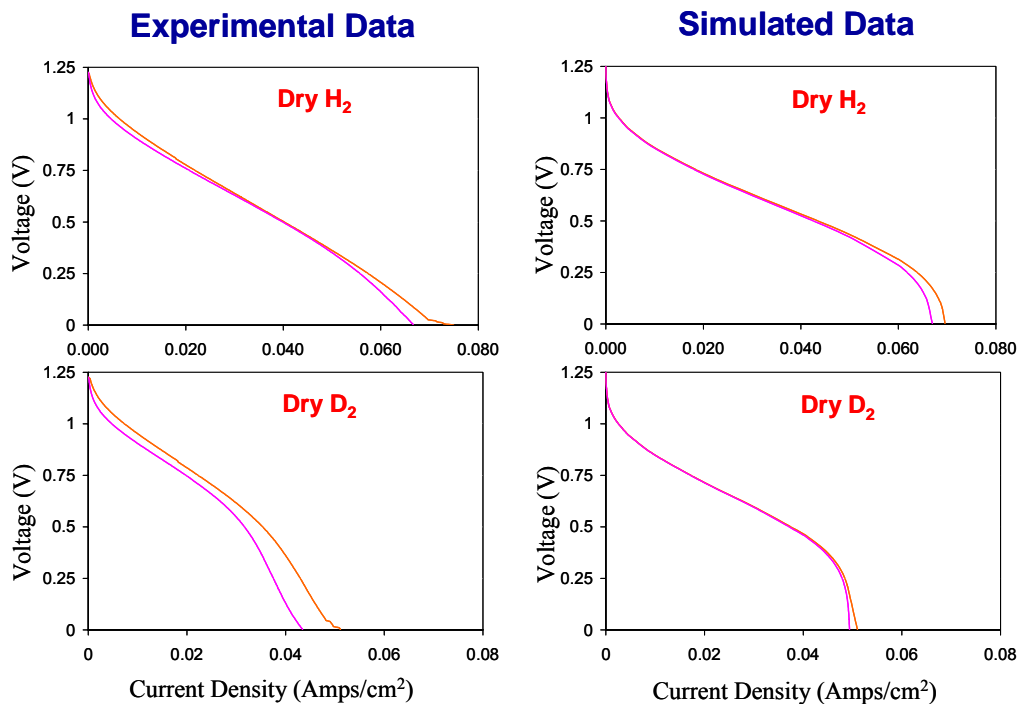


Figure 4.17 Comparison of experimental and simulated data from different thickness porous Au anodes at 70 sccm dry H₂ and D₂ fuel fractions (**Orange**: 30 µm and **Magenta**: 120 µm).

4.4. Discussions

4.4.1 The effect of dry H₂ partial pressures on porous Au anodes with different thicknesses in SOFC:

The power and current densities (Figure 4.3 and Table 4.1) are normalized with respect to the porous Au-YSZ interface area, which is 16 mm² for all four electrodes. The difference with respect to the thicknesses of Au anodes for the low to medium fuel partial pressures is observed in the higher current density region, which is explained in Chapter 1 as the mass transport limiting region. Thus, the detailed polarization curves showing maximum current densities of Au anodes are given next to the polarization curves of each fuel partial pressure case in Figure 4.3. For the medium to high fuel partial pressures, the thin electrodes have higher maximum

current densities than the thick electrodes, and this trend is more pronounced for the high fuel partial pressure. However, for the low fuel partial pressure, this observation is reversed and the thickest electrode has a higher maximum current density than the thinnest electrode.

The reason for the trend change by increasing H_2 partial pressure is the amount of water produced at the interface (Table 4.1). The water at the interface precludes the surface diffusion of adsorbed species and charge-transfer reactions. The fractions of water produced at the interface are in the range of 0.0140- 0.0152 % for 0.067 atm, 0.0706-0.0710 % for 0.333 atm, and, 0.101-0.134 % for 0.667 atm. These fractions are calculated by using the fuel conversion values times the fuel partial pressure divided by total gas flow. The water percentage rises with increasing fuel partial pressure due to the enhancement in the current and current densities.

For the low fuel partial pressure, the surface coverage of adsorbed H_2 species at the interface is low as compared to the amount of water produced at the interface. The higher current density of the thickest electrode is anticipated for the low fuel partial pressure. This is stemming from the higher active surface area of the thickest electrode available for the competition between adsorbed species and water at the interface.

For the medium to high H_2 partial pressures, the amount of water at the interface is much less than the adsorbed H_2 transporting to the interface. The surface diffusion of adsorbed species controls the current densities of the electrodes with respect to the thicknesses of electrodes at medium to high H_2 partial pressures. This is explained by the longer path on Au anode for adsorbed species of the thickest electrode surface

than that of the thinnest electrode. Consequently, the higher maximum current densities are expected for the thinnest electrode at medium to high H₂ partial pressures.

The water produced at the interface impedes the surface diffusion of H₂ species for the 0.067 atm H₂ fuel partial pressure (Figure 4.5 and Table 4.2). The amount of adsorbed H₂ species at the Au and YSZ interface is comparable with the amount of water produced; therefore, for the low fuel partial pressure, the water produced at the interface impacts the surface diffusion processes. The use of medium to high dry fuel partial pressures supplies a larger amount of surface H₂ species to the interface than the amount of water produced at the interface. For the medium to high fuel partial pressures, higher maximum current densities are observed for the thinnest electrodes. The $R_{an, Diff}$ values of porous Au anodes with various thicknesses for the medium to high dry fuel partial pressures reflect the trends in maximum current densities. The lower $R_{an, Diff}$ values of the thinnest electrodes ($5.1 \Omega \cdot \text{cm}^2$ for the medium fuel partial pressure and $6.5 \Omega \cdot \text{cm}^2$ for the high fuel partial pressure), as compared to those of the thickest electrodes ($7.6 \Omega \cdot \text{cm}^2$ for the medium fuel partial pressure and $7.0 \Omega \cdot \text{cm}^2$ at high fuel partial pressure) correlates with the higher maximum current densities of the thinnest electrodes.

The EIS results of Au anodes with various dry H₂ fuel partial pressures show that the surface diffusion of adsorbed species controls the maximum current densities for the medium to high fuel partial pressures. Moreover, for the low fuel partial pressures, the surface diffusion of adsorbed water species impedes the surface diffusion of H₂ species. The surface diffusion dominates the trends in the maximum

current densities of Au anodes. The effect of humidified H₂ fuel partial pressures on the polarization and impedance of Au anodes is further discussed in the following section.

There is a slight increase in the $R_{an, Diff}$ values with increasing thicknesses of the Au anodes (Figure 4.6), the trends of which are anticipated due to the decrease in the surface coverage of fuel species with the increase of the porous Au anode thickness. The $R_{an, Diff}$ values decrease significantly with respect to anode thicknesses at 0.067 atm dry H₂ flow. The possible explanation for this trend would be the effect of the water concentration gradient on $R_{an, Diff}$ values of Au anodes and the higher number of active surface sites of the thicker anodes. The increase in the Au anode thickness results in the low water concentration gradient through the Au anode, and then, $R_{an, Diff}$ values would be less in the thicker anodes than in the thinner anodes, and the number of active surface sites increases with increasing the Au anode thickness. The competition between water and the adsorbed species of H₂ fuel should be smaller in the thicker anodes than in the thinner anodes.

The fuel partial pressure dependence (Figure 4.7) of $R_{an, Diff}$ values may be explained by the trend between the low and medium fuel partial pressures in polarization curves in Figure 4.3. The thinnest porous Au anode has the highest $R_{an, Diff}$ value for the low dry H₂ partial pressure, whereas the lowest $R_{an, Diff}$ value is observed for the medium to high dry H₂ partial pressure, which explains the lowest current densities of the thinnest anodes for the low dry fuel partial pressures but the highest current densities for the medium to high dry fuel partial pressures. These trend changes between the low and medium dry fuel partial pressures for

performances of the four Au anodes is elucidated by the change in rate limiting diffusion steps between water and adsorbed fuel species.

4.4.2 The effect of water on Au anodes with varying partial pressures of H_2 :

The current and power densities (Figure 4.8 and Table 4.3) are normalized with respect to the porous Au-YSZ interface area. These values are higher as compared to dry H_2 cases. For the medium fuel partial pressures, again the thickest electrode has a higher maximum current density than the other thin electrodes. This trend for the medium fuel partial pressure case for wet H_2 is reversed as compared to dry H_2 . The reason of the reverse trend for the medium fuel partial pressure and wet H_2 is caused by the 3 % water in the fuel flow. Because, the humidified H_2 fuel has the higher water concentration than the amount of water produced (calculated as 0.0710 %) for each fuel partial pressure. Therefore, the maximum current densities for the low to medium fuel partial pressure are expected to be superior for the thickest electrode, due to the thickest electrode having a higher number of available active sites for H_2 and water species as compared to the thinnest electrode. However, for the high fuel partial pressure with 3 % water, the thinnest electrode has the highest maximum current density. This observed trend for the wet high fuel partial pressure is identical with the dry H_2 case. However, the maximum current densities for the high fuel partial pressure with 3% water are lower than the values for the high fuel partial pressure with dry H_2 case. The decrease in the maximum current density for wet H_2 for the high fuel partial pressure is due to the competition of water and adsorbed H_2 species for available active sites on porous Au anodes. The amount of H_2 species on

anodes increases with increasing the H_2 fuel partial pressure; hence, the water interference on surface diffusion of H_2 species decreases.

The amount of water calculated from current values is in the range of 0.0140-0.134 %. The combination of 3 % water added to the fuel flow and produced at the interface for 0.667 atm would be higher than for the 0.333 atm and 0.067 atm H_2 fuel partial pressures. Therefore, these reductions in the maximum current densities for the thicker electrodes are caused by the greater amount of water accumulated due to the greater anode surface area of the two thicker porous Au electrodes, because the longer the path for the water to diffuse through the Au anode, the more competition there is between water and H_2 adsorbed on porous Au anodes.

For each fuel partial pressure (Figure 4.9 and Table 4.4), $R_{an, CT}$ values of Au anodes are in the same range within experimental error. These trends in $R_{an, CT}$ values (increasing from low to medium and decreasing from medium to high wet fuel partial pressures) can be explained by the effect of H_2 surface coverage and diffusion of fuel species on $R_{an, CT}$ values. For the low wet fuel partial pressures the fuel surface coverage is low and the $R_{an, Diff}$ is high. Therefore, the $R_{an, CT}$ values are not affected by $R_{an, Diff}$, because of the fast charge-transfer reaction and low maximum current densities. However, for the medium wet fuel partial pressures the fuel surface coverage and the value of $R_{an, Diff}$ for the H_2 species are comparable; thus, these have the greatest affect on the $R_{an, CT}$ values. When the wet fuel partial pressure is increased to 0.667 atm, the surface coverage of fuel species is high enough to compensate for the surface diffusion. Therefore, the $R_{an, CT}$ values are expected to decrease from medium to high wet fuel partial pressures.

The $R_{an, Diff}$ values (Table 4.4) for the each wet fuel partial pressure vary with the thickness of the porous Au anode. The thickest anode for the low to medium wet fuel partial pressures has the lowest $R_{an, Diff}$ values of $55.1 \Omega \cdot \text{cm}^2$ and $14.1 \Omega \cdot \text{cm}^2$, respectively and for the high wet fuel partial pressure the highest $R_{an, Diff}$ value is $14.8 \Omega \cdot \text{cm}^2$. Since water content added to the fuel flow is constant ($3 \pm 0.134 \%$ as calculated) for every wet fuel partial pressure the percentage of water in the humidified fuel flow for every fuel partial pressure is assumed to be 3% . Therefore, both the water desorption and diffusion effects are assumed to be identical for every wet fuel partial pressure. As a result of these data and assumptions, the trends in the $R_{an, Diff}$ values dominate the trends in the maximum current densities for the low dry fuel partial pressure as observed in Figure 4.8. For the low to medium wet fuel partial pressures, higher maximum current densities are observed for the thickest electrodes. The $R_{an, Diff}$ values of the Au anodes for the low to medium wet fuel partial pressures also exhibit the same trends observed for the maximum current densities. The lower $R_{an, Diff}$ values of the thickest electrodes ($55.1 \Omega \cdot \text{cm}^2$ for the low wet fuel partial pressure and $14.1 \Omega \cdot \text{cm}^2$ for the medium wet fuel partial pressure) when compared to those of the thinnest electrodes ($83.3 \Omega \cdot \text{cm}^2$ for the low wet fuel partial pressure and $15.5 \Omega \cdot \text{cm}^2$ for the medium wet fuel partial pressure) correlate with the higher maximum current densities of the thickest anodes. Therefore, the electrochemical impedance measurements of the four Au anodes with various wet H_2 fuel partial pressures illustrate that at 3% water the water species on the Au anodes decrease the maximum current densities of porous Au anodes for the low to medium wet fuel partial pressures. Moreover, for the high fuel partial pressures, the surface diffusion

of adsorbed fuel species produces the same trends as observed for the maximum current densities of the four Au anodes.

The changes in the $R_{an, Diff}$ values (Figure 4.10) for the low to medium wet fuel partial pressures can be explained by the constant water concentration in the wet fuel flows. At 3 % humidity, the water produced at the interface has a competition with the surface diffusion of adsorbed fuel species for the low to medium wet fuel partial pressures. Since, the thickest anode has the highest number of active sites for water, the competition between water and adsorbed species of H_2 fuel for the active sites would be smaller for the thickest anodes than for the thinner anodes.

The fuel partial pressure dependence of $R_{an, Diff}$ (Figure 4.11) clarifies the trend shifts between medium and high wet fuel partial pressures in polarization curves in Figure 4.8. The thickest Au anode has the highest $R_{an, Diff}$ for the high wet H_2 partial pressure, whereas the lowest $R_{an, Diff}$ is observed for the low to medium wet H_2 partial pressures, which corresponds to the lowest current densities of the thickest anodes for the high wet fuel partial pressures but the highest current densities for the low to medium wet fuel partial pressures. The change in the rate limiting diffusion steps between water and the adsorbed fuel species may explain the trend changes for the maximum current densities of the Au anodes between the medium and high wet fuel partial pressures.

4.4.3 The comparison of isotopically labeled D_2 fuels with H_2 fuel on porous Au anodes with different thicknesses:

Primdahl [176] and Matsumoto [177] have proposed that the increase in D_2 surface diffusion resistance relative to H_2 can be attributed to the classical isotope effect. In

this study, dry H₂ and D₂ fuels perform the isotope effect (~1.5) within the experimental error. However, in wet fuel cases the isotope effect is amplified to ~1.7. The reason of this enhancement in the isotope effect is not fully understood and the classical isotope effect from harmonic oscillation model would not be efficient to explain this phenomenon. Further study is needed to address the question about the effect of water on the isotope effect and the surface diffusion.

The classical isotope effect [1] predicts the surface diffusion resistance difference between H₂ and D₂ species on the Au surface. The isotope effect is considered based on the classical harmonic oscillator, $\nu = \frac{1}{2\pi} \sqrt{\frac{k}{\mu}}$, where ν is the vibrational frequency on the surface, k is the force constant, and μ is the reduced mass. There is slight difference in the bond activation energies of H₂ and D₂, 432.0 and 439.6 kJ/mol respectively [1]. In changing from H₂ to D₂, k remains unchanged, but the reduced mass μ is different. A good approximation for changing from H to D is an increase in the reduced mass by a factor of $\sqrt{2}$ or 1.414. The frequency for D should be $1/\sqrt{2}$ times that of H. The surface diffusion coefficients of D would be $\sqrt{2}$, or 1.414 times that of H. Consequently, an isotope effect is expected between H₂ and D₂ in the surface diffusion resistance. The mass difference between H₂ and D₂ affects the surface diffusion limited region of polarization curves of SOFC anodes; the higher the mass, the slower the surface diffusion, and thus the higher surface diffusion resistance.

The same exact polarization data of dry H₂ for the medium fuel partial pressure are used to compare with isotopic labeling studies of D₂ for the medium fuel partial

pressures (Figure 4.12). The current and power densities of D_2 are also normalized with respect to the porous Au interface with YSZ. In general, the maximum power densities of SOFC anodes are reached at approximately 0.55 V (0.65 V overpotential according to OCV) in polarization curves. Since the surface diffusion in porous Au is affected by the mass of adsorbed species from isotopically labeled fuels, the separation in the mass transport limited region starts at lower overpotentials range of 0.60-0.70 V in the polarization curves. Consequently, the maximum power densities of D_2 are varied with respect to the thicknesses of porous Au anodes. As discussed in Section 4.4.1, in the case of dry H_2 for the medium fuel partial pressure, the thinnest electrode has higher maximum current densities than thicker electrodes. In the isotopic labeling studies the same trend is observed for the maximum power densities, because the surface diffusion of fuel species becomes the rate limiting step at lower overpotentials. Isotopic labeling studies also show that maximum current and power densities on Au anodes decrease by approximately 30 % for each thickness when D_2 is substituted for H_2 at identical SOFC operation conditions. When 3 % water is added to the D_2 fuel flow for the 70 sccm fraction, the maximum current densities of porous Au anodes decrease. The Au anode with the highest maximum current density changes from the thinnest (the highest in dry fuel flow) to the thickest (the higher in wet fuel flow) anodes. As observed for H_2 fuel from dry to wet 70 sccm H_2 flow, the trend shift from the thin to thick anode is also observed for 70 sccm dry to wet D_2 cases. The effect of the addition of 3 % water to the H_2 fuel flow for the medium fuel partial pressure is discussed in Section 4.4.2.

The differences in maximum power and current densities (Figure 4.12 and Table 4.5) with respect to isotopically labeled fuel used are attributed to the isotope effect on surface diffusion difference between H_2 and D_2 fuels due to their harmonic oscillation frequency difference based on reduced mass as explained previously in this section. Therefore, the classical isotope effect predicts that the shift in surface diffusion resistance should be proportional to the change in the square root of the mass, which is a factor of 1.414 for D_2/H_2 or D/H . The ratio of maximum current densities of dry H_2 to D_2 is in the range of 1.46-1.53, which is close to the range of the kinetic isotope effect of 1.41. The addition of 3 % water to fuel flow of both H_2 and D_2 gives the closer range of maximum current densities between the thinnest and the thickest porous Au electrodes. In the wet cases of H_2 and D_2 fuel flows, the ranges of maximum current densities are 72.4-76.2 mA/cm² (best for the thickest electrode) for wet H_2 fuel and 42.9-44.7 mA/cm² (best for the thickest electrode) for wet D_2 fuel. The mass transport or diffusion limited processes, such as surface diffusion, are increased by substituting H_2 to isotopically labeled D_2 fuel. This results in the high current or mass transport limited region on the polarization curves. The ratio of maximum current densities of wet H_2 and D_2 fuels is in the range of 1.69-1.74 for Au anodes. The reason for the increase in the isotope effect is explained by the fact that the water content reduces the surface diffusion rates of adsorbed species of H_2 and D_2 . The addition of 3 % water to H_2 and D_2 fuel flows improves the maximum current and power densities of H_2 fuel with respect to dry case, while reducing the maximum current and power densities of D_2 fuel with respect to the dry case. As a result of these data, the isotope effect on the surface diffusion clarifies that the maximum

current density decreases when dry D₂ is substituted for dry H₂ under identical conditions. However, the addition of 3 % water to the H₂ and D₂ fuel flows affect the surface diffusion rates of adsorbed species due to the competition between water and the adsorbed species at the active sites of porous Au.

The $R_{an, CT}$ values are in the range of 2.1-2.6 $\Omega \cdot \text{cm}^2$ for the dry fuel cases of both H₂ and D₂ fuels (Table 4.6). The range for the $R_{an, CT}$ values of wet H₂ fuel, 3.6-3.8 $\Omega \cdot \text{cm}^2$, is approximately half that of wet D₂ fuel, 7.2-7.4 $\Omega \cdot \text{cm}^2$, the trend for which can be explained by the effects of water on both wet H₂ and D₂ fuel performances. Since the water content in the fuel flow affects the surface coverage of the fuel species on the anode surface, the $R_{an, CT}$ values of wet D₂ fuel would be influenced more by the water content due to the isotope effect. The ratio in $R_{an, CT}$ values between wet H₂ and D₂ fuels is in the range of 1.8-2.1, the range of which is very similar observed in polarization curves in Figure 4.11.

In Figure 4.13 and Table 4.6, the surface diffusion resistances, $R_{an, Diff}$, for dry H₂ and D₂ fuel flows increase with respect to the thickness of porous Au anodes. The increase in $R_{an, Diff}$, from 5.1 to 7.6 $\Omega \cdot \text{cm}^2$ with dry H₂ fuel is slight when compared to the increase in $R_{an, Diff}$, from 9.7 to 15.5 $\Omega \cdot \text{cm}^2$ with dry D₂ fuel. When 3 % water is added to 70 sccm H₂ and D₂ fuel flows, $R_{an, Diff}$ values increase to the ranges of 14.4-16.1 $\Omega \cdot \text{cm}^2$ and 25.5-37.6 $\Omega \cdot \text{cm}^2$, respectively. In both wet fuel cases, the thickest anodes have the lowest $R_{an, Diff}$ values. The trend in $R_{an, Diff}$ values with respect to the thickness of porous Au anodes for wet H₂ fuel is an increase as explained in Section 4.3.3. Unlike for the wet H₂ fuel case, the $R_{an, Diff}$ values of wet D₂ fuel case decrease with respect to the thickness of porous Au anodes. This trend in

$R_{an, Diff}$ values explains the changes in maximum current densities from dry to wet case of D_2 fuel.

The $R_{an, Diff}$ dependence of dry D_2 fuel on the porous Au anode thicknesses is approximately 2.5 times higher than that of dry H_2 fuel with respect to the ratio of dry case slopes (Figure 4.14). Since the $R_{an, Diff}$ reflects both surface diffusion processes of both water and fuel species, then not only the isotope effect between H_2 and D_2 but also the water content affects this dependence. The water produced (in the range of 0.0437-0.0452 %) at the interface would influence the $R_{an, Diff}$ dependences of isotopically labeled D_2 fuel on the porous Au anode thicknesses.

In wet cases of H_2 and D_2 fuels, the $R_{an, Diff}$ values of H_2 and D_2 fuels decrease with respect to the porous Au anode thicknesses. These trends of the dependence $R_{an, Diff}$ on the thickness of the anodes for the wet H_2 cases at lower to medium fuel partial pressures are also observed and explained in Section 4.4.2. The decrease in $R_{an, Diff}$ values dependence on the thickness for the wet D_2 case is more pronounced than that of wet H_2 case. The ratio of the slopes of the dependence curves of the wet H_2 and D_2 fuels in Figure 4.14 is approximately 9. A possible explanation for this high ratio of dependences of wet H_2 and D_2 fuels would be the effect of 3 % water on the $R_{an, Diff}$ values of H_2 and D_2 fuel flows. The $R_{an, Diff}$ values of wet D_2 fuel case would possibly be influenced more than that of wet H_2 fuel case because the surface diffusion of adsorbed species of D_2 fuel is slower than that of H_2 fuel due to the isotope effect as explained earlier. Therefore, the higher $R_{an, Diff}$ dependence on the thickness of porous Au anodes for the wet D_2 fuel case would be anticipated.

4.4.4 Modeling studies of four different thicknesses porous Au anodes with various fuel partial pressures of H₂:

Addition of surface diffusion effects to the model provides a good agreement between experimental and simulated data. Since the effect of the water concentration on surface diffusion on porous Au anodes is not considered in these simulated data, the shapes of the simulated polarization curves deviate from the experimental polarization curves. As the model used in this study employs the processes happening at 30 μm above the interface, the separation between the thinnest and thickest anode in the high current density region of the polarization curve disappears in the simulated data. As a result of the comparison of experimental and simulated polarization data in Figure 4.16, the model would clearly explain the partial pressure effect in surface diffusion on a qualitative level, whereas, it could not explain the anode thickness effect and the water concentration effect on surface diffusion, $D_{surf, cat}$.

Two different surface diffusion coefficients, $D_{surf, cat}$, with respect to dry H₂ fuel partial pressures on the porous Au anodes are employed to fit the experimental data (Table 4.7 and Figure 4.16). The values of $D_{surf, cat}$ are $1.87 \times 10^{-7} \text{ m}^2/\text{s}$ for 0.067 atm and $3.61 \times 10^{-7} \text{ m}^2/\text{s}$ for 0.333 atm and 0.667 atm dry H₂ flows. These $D_{surf, cat}$ values are consistent with the range of $D_{surf, cat}$ values between 1×10^{-4} and $1 \times 10^{-7} \text{ m}^2/\text{s}$ reported in the literature for Ni and Ni/YSZ systems [105, 158, 172, 174]. These two different $D_{surf, cat}$ values in this model used to generate the experimental data confirm the trend changes in maximum current densities with respect to the anode thicknesses from 0.067 to 0.333 atm dry H₂ fuel partial pressures.

The isotope effect (Figure 4.17) on maximum current densities of Au anodes with dry H₂ and D₂ fuels is predicted by using this model. The model is based on the chemical and physical nature of the surface species on porous Au anodes by using different $D_{surf, cat}$ values. The mass difference between H₂ and D₂ suggests that the factor of 1.41 should be applied to add the isotope effect to $D_{surf, cat}$ values between H₂ and D₂. The value of $D_{surf, cat}$ of 2.56×10^{-7} m²/s is employed in this model. Good agreement between experimental and simulated polarization data confirms that $D_{surf, cat}$ dominates the maximum current densities of dry H₂ and D₂ fuels. Addition of water concentration effect on $D_{surf, cat}$ may provide better fit with respect to experimental data. Since the model is not capable of manipulating the $D_{surf, cat}$ with respect to all ranges of anode thickness, the separation between the thinnest and the thickest anodes in the high current region is not clearly observed.

4.5. Conclusions

The present work illustrates that the mass transport related processes of the H₂ oxidation reactions on SOFC anodes are of critical importance. The effect of surface diffusion of adsorbed H₂ and H₂O species on porous Au anode performances is examined by using various anode thicknesses and different H₂ partial pressures with and without 3 % water in this study. Further investigations of surface diffusion are conducted by utilizing isotopically labeled D₂ fuel instead of H₂ fuel under identical SOFC conditions. Modeling studies of porous Au anodes aim to integrate the effect of the parameters mentioned above by manipulating the coefficients of processes based on the chemical and physical characteristics of porous Au anodes.

The effect of various thicknesses of porous Au anodes emerges in the high current region of the polarization curves. The electrochemical impedance results, at the overpotential in the high current region, and their equivalent circuit fits of various thickness porous Au anodes corroborate the polarization measurements. The separation in the high current region of the polarization curves of the Au anodes is attributed to two different sources of surface speciation; namely, the dissociatively adsorbed H_2 fuel species diffusing toward the Au-YSZ interface and water species diffusing out of the Au-YSZ interface. These two different sources, which competitively affect the surface diffusion processes, are evaluated using electrochemical impedance in the high current region overpotentials.

The polarization and electrochemical impedance measurements of four different thickness porous Au anodes under various H_2 partial pressures from 0.0333 to 0.667 atm with and without humidification reveal two different trend changes in the maximum current densities as well as the diffusion resistances, $R_{an, Diff}$, depending on dry or wet fuel conditions. These two trend changes mainly point the critical partial pressures of H_2 , for dry approximately 0.2 atm (~42 sccm fuel fraction) and for wet, approximately 0.4 atm (~84 sccm fuel fraction) conditions. At these H_2 partial pressures, it is proposed that the diffusion of H_2 fuel species and water species would have a comparable effect on both polarization and impedance curves (performance on porous Au anodes). At H_2 partial pressure lower than the critical partial pressure, the water species become the dominant factor controlling the anode performances. At H_2 partial pressure higher than the critical partial pressure, the surface diffusion of H_2 fuel species controls the anode performance.

The diffusion resistances, $R_{an, Diff}$, are linear with respect to the anode thicknesses for every dry/wet fuel partial pressure. Moreover, the slope of linearity defines the increase or decrease in $R_{an, Diff}$ with respect to the anode thickness. Below the critical partial pressure, $R_{an, Diff}$ values increase with respect to anode thickness, while they decrease above the critical partial pressure. As expected, the charge-transfer resistances, $R_{an, CT}$, distinguished by equivalent circuit fits are in the same range for the four Au anodes under a certain fuel composition. This is because the charge-transfer reactions depend on the Au-YSZ interface area and every porous Au anode used in this study has an identical interface area. The $R_{an, CT}$ values decrease with respect to H_2 partial pressures, but also increase with water concentrations.

Isotopic labeling studies show that maximum current and power densities on various thickness porous Au anodes decreases by approximately 30 % upon substitution of D_2 for H_2 under identical conditions. As expected, the mass of H_2 vs. D_2 fuel species, most probably related to surface diffusion on porous Au anodes, is recognized as the source of this decrease in SOFC performances.

Preliminary modeling studies on porous Au anodes corroborate the interpretation of polarization and impedance records. The polarization curves simulated by the model for various fuels and various partial pressures correlate well with the experimentally observed dependence of porous Au anode performances on surface diffusion of fuel species under different H_2 partial pressures. Also, the model used in this study confirms that the isotope effect is able to be described qualitatively by the mass effect on the gas and surface diffusion coefficients. However, the addition of the effects of the water species to this model is necessary to manipulate the critical fuel partial

pressure values. Since in the present study only the polarization curves are simulated, in the future, a model with the ability to predict the electrochemical impedance spectra is needed for a more complete understanding the chemical and physical processes on SOFC assembly.

Chapter 5:

Conclusions

5.1. Introduction

The body of the thesis is organized in three chapters dealing with experiments on different types of SOFC anodes to characterize the carbon deposits from hydrocarbon fuels (Chapter 2), experiments on different types of Au/YSZ anodes with different geometries and combinations to distinguish their contribution on SOFC performance (Chapter 3), and on isotope dependence and modeling of the Au/YSZ systems (Chapter 4). The last two chapters aim to evaluate the H₂ oxidation kinetics on SOFC anodes and to determine the rate limiting steps for these processes. In this chapter, the results and the derived scientific analyses are briefly summarized. Recommendations for future work are given based on the findings and literature review.

5.2. Evaluation of the results:

In this study, the power and current densities of SOFC systems are 10-20 times lower than the contemporary SOFC systems, because the electrolyte support design of SOFC is utilized to examine the fuel oxidation mechanisms. The thickness of the YSZ electrolytes employed in this study varies between 1.00 to 1.20 mm, as compared to 0.020 to 0.030 mm in conventional SOFC systems in which mostly Ni/YSZ cermet anode systems are used as the anode materials. The series of anode systems, such as Ni/YSZ and Cu/CeO₂/YSZ, are evaluated for the characterization of

carbon deposits from hydrocarbons. The Au/YSZ systems are chosen to examine the rate limiting step of the H_2 oxidation reaction on the SOFC anodes

Combining a number of the structural characterization techniques of the carbon deposits on the Ni/YSZ and Cu/CeO₂/YSZ anode systems in the SOFC feeding with butane fuel show that graphitic carbon with an average grain size of 4 to 12 nm is formed, which is defined as nanocrystalline graphite in Chapter 2. The spherical morphology is observed in both anode systems. However, the filamentous carbon morphology is only formed on Ni/YSZ anode surfaces due to Ni particles providing nucleation sites for the formation of filamentous morphology. The combinations of three parameters, namely the disorder in the crystal structure, sp^3 carbon atoms, and morphology of carbon deposits, are three significant factors that affect the carbon deposit characteristic. The nanocrystalline graphite formation gives short term enhancement in poorly conductive anodes such as the Cu/CeO₂/YSZ anode systems but not in the Ni/YSZ anode systems. These findings suggest that the nanocrystalline graphite formation likely increases the anode conductivity, thus, the performance of SOFC anodes enhances.

From the experimental results presented in Chapter 3, it is concluded that the possible rate limiting steps in anodic H_2 oxidation are the surface diffusion of dissociatively adsorbed H_2 species, the charge-transfer reactions of these adsorbed species at the interface, and the desorption of H_2O from anode-electrolyte interface. The correlations, observed on the polarization and EIS curves of the Au anodes with respect to Au anode-electrolyte interface area, clarify the charge-transfer reactions taking place only at the interface, despite of the different porosities of the Au anodes

and the geometries of the porous YSZ coatings on the porous Au anodes. These correlations reveal that the TPB of the Au anodes are distributed across the entire interface between Au electrode and YSZ electrolyte. The porous YSZ experiments on Au anodes illustrate that YSZ prohibits the dissociative adsorption of H_2 on the Au surface. However, YSZ layer carrying O^{2-} ions enhances the charge-transfer reactions on the Au surface. The $\alpha-Al_2O_3$ blocking experiments confirm that the electrochemical oxidation of H_2 is directly dependent upon the interface area between the Au anode and YSZ electrolyte.

The studies presented in Chapter 4 combine the experimental and computational data and illustrate that the mass transport related processes of the H_2 oxidation reactions on SOFC anodes are of the critical importance to Au anode polarization and impedance. The surface diffusions of adsorbed H_2 and H_2O species on Au anodes are the two competitive phenomena, which directly affect the Au anode performance.

The investigations of the isotope effect by utilizing isotopically labeled D_2 fuel, instead of H_2 fuel under identical SOFC conditions, suggest that the surface diffusion of adsorbed fuel species is of vital significance for Au anode current and power densities. It is shown that the surface diffusion resistance of D_2 is higher than that of H_2 , which explains the higher current and power densities for H_2 .

Preliminary modeling studies of Au anodes support the polarization and impedance data analysis. The polarization curves simulated by the model suggest that the surface diffusion of fuel species on Au anode surfaces varies with different H_2 partial pressures. The isotope effect on Au anode performance is corroborated by the model

used in this study. The surface diffusions of both H_2 and D_2 species are qualitatively described by the mass effect on the surface diffusion coefficients.

5.2. Future works and recommendations:

The direct electrochemical oxidation of hydrocarbons on a SOFC anode is not well-understood. The results from structural analysis of carbon deposits may help to address the questions about the oxidation mechanism of longer hydrocarbons under SOFC operating conditions. Future studies on carbon deposit formation from hydrocarbons in a SOFC anode require the examination of humidified hydrocarbon fuels on these anode systems. These findings about carbon deposit formation on various SOFC anode surfaces give a basis for understanding the mechanism of direct electrochemical oxidation of hydrocarbons in a SOFC anode.

The series of the systematic experiments on other anode systems such as Ni/YSZ and CeO_2 /YSZ anode systems by using Au as a current collector would address the questions regarding to anode material effect on the fuel oxidation mechanism because the experimental and computational data from the Au/YSZ anode systems provides the basis for SOFC anodes before beginning to evaluate the more complicated anode systems with different fuels.

The addition of the effects of water species to the computational model is necessary to evaluate the performance dependence on the fuel partial pressure and the concentration of the water at the interface. Simulations of electrochemical impedance would help the understanding of the chemical and physical processes on the SOFC assembly. The combination of polarization and impedance simulations of anode systems with different fuels would provide the complete analysis.

Appendix

Gamry EIS Fitting Data (taken directly from Echem Analyst software)

14 sccm Dry H₂

	30 μm	60 μm	90 μm	120 μm
R _b	4.866 Ω	3.390 Ω	4.238 Ω	2.325 Ω
R _{cat, CT}	145.0 m Ω	145.0 m Ω	145.0 m Ω	145.0 m Ω
R _{cat, Diff}	2.210 Ω	2.210 Ω	2.210 Ω	2.210 Ω
C _{cat, CL}	72.65 mF	72.65 mF	72.65 mF	72.65 mF
R _{an, CT}	79.11 Ω	67.33 Ω	52.78 Ω	45.29 Ω
Q _{an, CT}	88.38e-6 S*s^a	114.3e-6 S*s^a	53.14e-6 S*s^a	59.34e-6 S*s^a
n _{an, CT}	673.3 m	668.3 m	755.0 m	800.2 m
L _b	1.120 μ H	1.120 μ H	1.120 μ H	1.120 μ H
Q _{cat, diff}	18.50e-3 S*s ^a	18.50e-3 S*s ^a	18.50e-3 S*s ^a	18.50e-3 S*s ^a
n _{an, CT}	715.0 m	715.0 m	715.0 m	715.0 m
R _{an, Diff}	6.763 Ω	6.477 Ω	6.416 Ω	6.135 Ω
Q _{an, Diff}	40.34e-6 S*s^a	45.11e-6 S*s^a	191.9e-6 S*s^a	228.5e-6 S*s^a
n _{an, Diff}	469.0 m	481.0 m	492.0 m	487.0 m
Goodness of Fit	0.0003706	0.0004202	0.0001702	0.0003634

70 sccm Dry H₂

	30 μm	60 μm	90 μm	120 μm
R _b	1.022 Ω	552.0 m Ω	599.9 m Ω	1.047 Ω
R _{cat, CT}	145.0 m Ω	145.0 m Ω	145.0 m Ω	145.0 m Ω
R _{cat, Diff}	2.210 Ω	2.210 Ω	2.210 Ω	2.210 Ω
C _{cat, CL}	72.65 mF	72.65 mF	72.65 mF	72.65 mF
R _{an, CT}	5.112 Ω	6.612 Ω	7.450 Ω	7.551 Ω
Q _{an, CT}	150.0e-6 S*s^a	404.3e-6 S*s^a	295.6e-6 S*s^a	207.6e-6 S*s^a
n _{an, CT}	876.1 m	752.6 m	771.3 m	818.2 m
L _b	1.120 μ H	1.120 μ H	1.120 μ H	1.120 μ H
Q _{cat, diff}	18.50e-3 S*s ^a	18.50e-3 S*s ^a	18.50e-3 S*s ^a	18.50e-3 S*s ^a
n _{an, CT}	715.0 m	715.0 m	715.0 m	715.0 m
R _{an, Diff}	2.120 Ω	2.204 Ω	2.215 Ω	2.256 Ω
Q _{an, Diff}	314.1e-9 S*s^a	27.77e-9 S*s^a	56.81e-9 S*s^a	83.86e-9 S*s^a
n _{an, Diff}	935.7 m	1.15E+00	1.084	1.025
Goodness of Fit	2.90E-03	1.17E-03	0.001383	0.001232

140 sccm Dry H₂

	30 μm	60 μm	90 μm	120 μm
R _b	906.3 m Ω	879.1 m Ω	831.02 m Ω	837.1 m Ω
R _{cat, CT}	145.0 m Ω	145.0 m Ω	145.0 m Ω	145.0 m Ω
R _{cat, Diff}	2.210 Ω	2.210 Ω	2.560 Ω	2.560 Ω
C _{cat, CL}	72.65 mF	72.65 mF	72.65 mF	72.65 mF
R_{an, CT}	6.461 Ω	6.493 Ω	6.443 Ω	7.031 Ω
Q_{an, CT}	121.7e-6 S*s^a	161.4e-6 S*s^a	33.97e-6 S*s^a	73.13e-6 S*s^a
n_{an, CT}	743.6 m	679.7 m	815.5 m	767.3 m
L _b	1.120 μH	1.120 μH	1.120 μH	1.120 μH
Q _{cat, diff}	18.50e-3 S*s ^a	18.50e-3 S*s ^a	18.50e-3 S*s ^a	18.50e-3 S*s ^a
n _{an, CT}	715.0 m	715.0 m	715.0 m	715.0 m
R_{an, Diff}	2.097 Ω	2.262 Ω	2.351 Ω	2.224 Ω
Q_{an, Diff}	2.731e-9 S*s^a	837.8e-12 S*s^a	23.17e-9 S*s^a	9.385e-9 S*s^a
n_{an, Diff}	1.277	1.381	1.176	1.236
Goodness of Fit	1.64E-03	0.002491	0.004084	0.003732

14 sccm Wet H₂

	30 μm	60 μm	90 μm	120 μm
R _b	2.980 Ω	2.930 Ω	2.720 Ω	2.830 Ω
R _{cat, CT}	145.0 m Ω	145.0 m Ω	145.0 m Ω	145.0 m Ω
R _{cat, Diff}	2.560 Ω	2.560 Ω	2.560 Ω	2.560 Ω
C _{cat, CL}	72.65 mF	72.65 mF	72.65 mF	72.65 mF
R_{an, CT}	83.26 Ω	73.93 Ω	63.75 Ω	55.11 Ω
Q_{an, CT}	60.82e-6 S*s^a	127.7e-6 S*s^a	84.85e-6 S*s^a	97.92e-6 S*s^a
n_{an, CT}	839.7 m	798.6 m	850.2 m	847.6 m
L _b	1.120 μH	1.120 μH	1.120 μH	1.120 μH
Q _{cat, diff}	18.50e-3 S*s ^a	18.50e-3 S*s ^a	18.50e-3 S*s ^a	18.50e-3 S*s ^a
n _{an, CT}	715.0 m	715.0 m	715.0 m	715.0 m
R_{an, Diff}	1.401 Ω	1.442 Ω	1.091 Ω	0.810 Ω
Q_{an, Diff}	51.8e-6 S*s^a	8.040e-6 S*s^a	25.84e-6 S*s^a	5.918e-6 S*s^a
n_{an, Diff}	974.8 m	1.008	915.5 m	1.031
Goodness of Fit	0.001755	0.003467	0.003532	0.003352

70 sccm Wet H₂

	30 μm	60 μm	90 μm	120 μm
R _b	1.323 Ω	1.123 Ω	787.1 m Ω	1.347 Ω
R _{cat, CT}	145.0 m Ω	145.0 m Ω	145.0 m Ω	145.0 m Ω
R _{cat, Diff}	2.560 Ω	2.560 Ω	2.560 Ω	2.560 Ω
C _{cat, CL}	17.27 mF	17.27 mF	17.27 mF	72.65 mF
R_{an, CT}	15.46 Ω	15.05 Ω	14.51 Ω	14.08 Ω
Q_{an, CT}	3.416e-3 S*s^a	4.196e-3 S*s^a	9.976e-3 S*s^a	24.10e-3 S*s^a
n_{an, CT}	442.4 m	391.3 m	322.4 m	222.1 m
L _b	1.120 μH	1.120 μH	1.120 μH	1.120 μH
Q _{cat, diff}	18.50e-3 S*s ^a	18.50e-3 S*s ^a	18.50e-3 S*s ^a	18.50e-3 S*s ^a
n _{an, CT}	715.0 m	715.0 m	715.0 m	715.0 m
R_{an, Diff}	3.573 Ω	3.709 Ω	3.969 Ω	3.678 Ω
Q_{an, Diff}	46.97e-6 S*s^a	19.46e-6 S*s^a	48.79e-6 S*s^a	44.98e-6 S*s^a
n_{an, Diff}	0.976	1.067	952.7 m	982.4 m
Goodness of Fit	0.007909	0.007807	0.001136	0.001453

140 sccm Wet H₂

	30 μm	60 μm	90 μm	120 μm
R _b	1.840 Ω	1.940 Ω	2.320 Ω	2.180 Ω
R _{cat, CT}	145.0 m Ω	145.0 m Ω	145.0 m Ω	145.0 m Ω
R _{cat, Diff}	2.560 Ω	2.560 Ω	2.560 Ω	2.560 Ω
C _{cat, CL}	72.65 mF	72.65 mF	72.65 mF	72.65 mF
R_{an, CT}	721.1 mΩ	792.4 mΩ	702.0 mΩ	779.4 mΩ
Q_{an, CT}	2.374e-6 S*s^a	68.75e-9 S*s^a	5.792e-6 S*s^a	6.908e-6 S*s^a
n_{an, CT}	1.107	1.395	1.044	1.021
L _b	1.120 μH	1.120 μH	1.120 μH	1.120 μH
Q _{cat, diff}	18.50e-3 S*s ^a	18.50e-3 S*s ^a	18.50e-3 S*s ^a	18.50e-3 S*s ^a
n _{an, CT}	715.0 m	715.0 m	715.0 m	715.0 m
R_{an, Diff}	8.955 Ω	12.09 Ω	13.02 Ω	14.77 Ω
Q_{an, Diff}	47.19e-6 S*s^a	117.1e-6 S*s^a	47.44e-6 S*s^a	46.26e-6 S*s^a
n_{an, Diff}	951.5 m	822.7 m	919.2 m	911.5 m
Goodness of Fit	0.009535	0.007242	0.006019	0.005766

70 sccm Dry D₂

	30 μm	60 μm	90 μm	120 μm
R _b	650.5 m Ω	611.1 m Ω	-1.104 Ω	-329.8 m Ω
R _{cat, CT}	145.0 m Ω	145.0 m Ω	145.0 m Ω	145.0 m Ω
R _{cat, Diff}	2.560 Ω	2.560 Ω	2.560 Ω	2.560 Ω
C _{cat, CL}	72.65 mF	72.65 mF	72.65 mF	72.65 mF
R_{an, CT}	2.540 Ω	2.308 Ω	2.606 Ω	2.180 Ω
Q_{an, CT}	249.1e-6 S*s^a	42.78e-9 S*s^a	5.789e-9 S*s^a	329.0e-9 S*s^a
n_{an, CT}	558.1 m	1.107	1.239	961.3 m
L _b	1.120 μH	1.120 μH	1.120 μH	1.120 μH
Q _{cat, diff}	18.50e-3 S*s ^a	18.50e-3 S*s ^a	18.50e-3 S*s ^a	18.50e-3 S*s ^a
n _{an, CT}	715.0 m	715.0 m	715.0 m	715.0 m
R_{an, Diff}	9.689 Ω	12.24 Ω	14.22 Ω	15.53 Ω
Q_{an, Diff}	120.0e-6 S*s^a	362.9e-6 S*s^a	322.0e-6 S*s^a	198.0e-6 S*s^a
n_{an, Diff}	905.0 m	764.3 m	766.2 m	832.7 m
Goodness of Fit	0.002299	0.003144	0.001827	0.001735

70 sccm Wet D₂

	30 μm	60 μm	90 μm	120 μm
R _b	1.132 Ω	1.035 Ω	778.0 m Ω	895.8 m Ω
R _{cat, CT}	145.0 m Ω	145.0 m Ω	145.0 m Ω	145.0 m Ω
R _{cat, Diff}	2.560 Ω	2.560 Ω	2.560 Ω	2.560 Ω
C _{cat, CL}	72.65 mF	72.65 mF	72.65 mF	72.65 mF
R_{an, CT}	37.62 Ω	33.68 Ω	29.78 Ω	25.48 Ω
Q_{an, CT}	5.511e-3 S*s^a	9.205e-3 S*s^a	9.034e-3 S*s^a	11.43e-3 S*s^a
n_{an, CT}	389.9 m	325.4 m	309.9 m	299.9 m
L _b	1.120 μH	1.120 μH	1.120 μH	1.120 μH
Q _{cat, diff}	18.50e-3 S*s ^a	18.50e-3 S*s ^a	18.50e-3 S*s ^a	18.50e-3 S*s ^a
n _{an, CT}	715.0 m	715.0 m	715.0 m	715.0 m
R_{an, Diff}	7.356 Ω	7.335 Ω	7.179 Ω	7.421 Ω
Q_{an, Diff}	44.84e-6 S*s^a	48.26e-6 S*s^a	49.81e-6 S*s^a	35.75e-6 S*s^a
n_{an, Diff}	1.03E+00	995.4 m	978.7 m	1.052
Goodness of Fit	1.63E-03	0.001162	0.002547	0.001049

References

1. Atkins, P., and Paula, J., *Physical Chemistry*. Seventh edition ed. 2002: Oxford University Press.
2. Reif, F., *Fundamentals of Statistical and Thermal Physics*. McGraw-Hill Series in Fundamentals of Physics. 1985: McGraw-Hill Book Company.
3. Lundberg, W.L., S.E. Veyo, and M.D. Moeckel, *A high-efficiency solid oxide fuel cell hybrid power system using the mercury 50 advanced turbine systems gas turbine*. Journal Of Engineering For Gas Turbines And Power-Transactions Of The Asme, 2003. **125**(1): p. 51-58.
4. Autissier, N., et al., *Thermo-economic optimization of a solid oxide fuel cell, gas turbine hybrid system*. Journal Of Fuel Cell Science And Technology, 2007. **4**(2): p. 123-129.
5. Grove, W.R., Phil. Mag., 1839. **14**: p. 127.
6. Nernst, W., Z Electrochem., 1899. **6**: p. 41.
7. Brandon, N.P., S. Skinner, and B.C.H. Steele, *Recent advances in materials for fuel cells*. Annual Review Of Materials Research, 2003. **33**: p. 183-213.
8. Ormerod, R.M., *Solid oxide fuel cells*. Chemical Society Reviews, 2003. **32**(1): p. 17-28.
9. Blomen, L.J.M.J.a.M., M.N., *Fuel Cell Systems*. 1993, New York: Plenum Press.
10. Kim, H., et al., *Direct oxidation of liquid fuels in a solid oxide fuel cell*. Journal Of The Electrochemical Society, 2001. **148**(7): p. A693-A695.
11. Costa-Nunes, O., R.J. Gorte, and J.M. Vohs, *Comparison of the performance of Cu-CeO₂-YSZ and Ni-YSZ composite SOFC anodes with H₂, CO, and syngas*. Journal Of Power Sources, 2005. **141**(2): p. 241-249.
12. Baur, E.a.P., H., Zeitschrift fur electrochemie, 1937. **43**(9): p. 727.
13. Yokokawa, H., Sakai, N., Horita, T., and Yamaji, K., *Fuel Cells*. 2001. **1**(2): p. 117.
14. Fergus, J.W., *Electrolytes for solid oxide fuel cells*. Journal Of Power Sources, 2006. **162**(1): p. 30-40.
15. Holtappels, P., U. Vogt, and T. Graule, *Ceramic materials for advanced solid oxide fuel cells*. Advanced Engineering Materials, 2005. **7**(5): p. 292-302.
16. Minh, N.Q., *Solid oxide fuel cell technology-features and applications*. Solid State Ionics, 2004. **174**(1-4): p. 271-277.
17. Goodenough, J.B., *Oxide-ion electrolytes*. Annual Review Of Materials Research, 2003. **33**: p. 91-128.
18. Feinberg, A. and C.H. Perry, *Structural Disorder And Phase-Transitions In ZrO₂-Y₂O₃ System*. Journal Of Physics And Chemistry Of Solids, 1981. **42**(6): p. 513-518.
19. Hattori, M., et al., *Effect of aging on conductivity of yttria stabilized zirconia*. Journal Of Power Sources, 2004. **126**(1-2): p. 23-27.

20. Pinol, S., M. Morales, and F. Espiell, *Low temperature anode-supported solid oxide fuel cells based on gadolinium doped ceria electrolytes*. Journal Of Power Sources, 2007. **169**(1): p. 2-8.
21. Huang, H., et al., *High-performance ultrathin solid oxide fuel cells for low-temperature operation*. Journal Of The Electrochemical Society, 2007. **154**(1): p. B20-B24.
22. Luo, J., R.J. Ball, and R. Stevens, *Gadolinia doped ceria/yttria stabilised zirconia electrolytes for solid oxide fuel cell applications*. Journal Of Materials Science, 2004. **39**(1): p. 235-240.
23. Enoki, M., et al., *High oxide ion conductivity in Fe and Mg doped LaGaO₃ as the electrolyte of solid oxide fuel cells*. Solid State Ionics, 2006. **177**(19-25): p. 2053-2057.
24. Gong, W.Q., S. Gopalan, and U.B. Pal, *Performance of intermediate temperature (600-800 degrees C) solid oxide fuel cell based on Sr and Mg doped lanthanum-gallate electrolyte*. Journal Of Power Sources, 2006. **160**(1): p. 305-315.
25. Lin, Y.B. and S.A. Barnett, *Co-firing of anode-supported SOFCs with thin La_{0.9}Sr_{0.1}Ga_{0.8}Mg_{0.2}O_{3-δ} electrolytes*. Electrochemical And Solid State Letters, 2006. **9**(6): p. A285-A288.
26. Fleig, J., *Solid oxide fuel cell cathodes: Polarization mechanisms and modeling of the electrochemical performance*. Annual Review Of Materials Research, 2003. **33**: p. 361-382.
27. Ostergard, M.J.L., et al., *Manganite-Zirconia Composite Cathodes For Sofc - Influence Of Structure And Composition*. Electrochimica Acta, 1995. **40**(12): p. 1971-1981.
28. Jorgensen, M.J., et al., *Effect of sintering temperature on microstructure and performance of LSM-YSZ composite cathodes*. Solid State Ionics, 2001. **139**(1-2): p. 1-11.
29. Hwang, H.J., et al., *Electrochemical performance of LSCF-based composite cathodes for intermediate temperature SOFCs*. Journal Of Power Sources, 2005. **145**(2): p. 243-248.
30. Wang, W.G. and M. Mogensen, *High-performance lanthanum-ferrite-based cathode for SOFC*. Solid State Ionics, 2005. **176**(5-6): p. 457-462.
31. Wang, S.Z. and X. Liu, *Preparation and characterization of high performance Sm_{0.5}Sr_{0.5}CoO₃ cathodes*. Acta Physico-Chimica Sinica, 2004. **20**(4): p. 391-395.
32. Fukunaga, H., et al., *Reaction model of dense Sm_{0.5}Sr_{0.5}CoO₃ as SOFC cathode*. Solid State Ionics, 2000. **132**(3-4): p. 279-285.
33. Bieberle-Hutter, A.B. and H.L. Tuller, *Fabrication and structural characterization of interdigitated thin film La(1-x)SrCoO(3)(LSCO) electrodes*. Journal Of Electroceramics, 2006. **16**(2): p. 151-157.
34. Inagaki, T., et al., *High-performance electrodes for reduced temperature solid oxide fuel cells with doped lanthanum gallate electrolyte II. La(Sr)CoO₃ cathode*. Journal Of Power Sources, 2000. **86**(1-2): p. 347-351.

35. Jiang, S.P. and S.H. Chan, *Development of Ni/Y₂O₃-ZrO₂ cermet anodes for solid oxide fuel cells*. Materials Science And Technology, 2004. **20**(9): p. 1109-1118.
36. Jiang, S.P. and S.H. Chan, *A review of anode materials development in solid oxide fuel cells*. Journal Of Materials Science, 2004. **39**(14): p. 4405-4439.
37. Atkinson, A., et al., *Advanced anodes for high-temperature fuel cells*. Nature Materials, 2004. **3**(1): p. 17-27.
38. Sarantaridis, D. and A. Atkinson, *Redox cycling of Ni-based solid oxide fuel cell anodes: A review*. Fuel Cells, 2007. **7**(3): p. 246-258.
39. McIntosh, S., J.M. Vohs, and R.J. Gorte, *Role of hydrocarbon deposits in the enhanced performance of direct-oxidation SOFCs*. Journal Of The Electrochemical Society, 2003. **150**(4): p. A470-A476.
40. Lu, J.B., Z.T. Zhang, and Z.L. Tang, *Review on the development of solid oxide fuel cells*. Rare Metal Materials And Engineering, 2005. **34**(8): p. 1177-1180.
41. Gauckler, L.J., et al., *Solid oxide fuel cells: Systems and materials*. Chimia, 2004. **58**(12): p. 837-850.
42. Mogensen, M., N.M. Sammes, and G.A. Tompsett, *Physical, chemical and electrochemical properties of pure and doped ceria*. Solid State Ionics, 2000. **129**(1-4): p. 63-94.
43. Kee, R.J., H.Y. Zhu, and D.G. Goodwin, *Solid-oxide fuel cells with hydrocarbon fuels*. Proceedings Of The Combustion Institute, 2005. **30**: p. 2379-2404.
44. Ramirez-Cabrera, E., A. Atkinson, and D. Chadwick, *Catalytic steam reforming of methane over Ce_{0.9}Gd_{0.1}O_{2-x}*. Applied Catalysis B-Environmental, 2004. **47**(2): p. 127-131.
45. Sauvet, A.L. and J. Fouletier, *Catalytic properties of new anode materials for solid oxide fuel cells operated under methane at intermediary temperature*. Journal Of Power Sources, 2001. **101**(2): p. 259-266.
46. Murray, E.P., T. Tsai, and S.A. Barnett, *A direct-methane fuel cell with a ceria-based anode*. Nature, 1999. **400**(6745): p. 649-651.
47. Putna, E.S., et al., *Ceria-based anodes for the direct oxidation of methane in solid oxide fuel cells*. Langmuir, 1995. **11**(12): p. 4832-4837.
48. Ahn, K.Y., et al., *Enhanced thermal stability of SOFC anodes made with CeO₂-ZrO₂ solutions*. Electrochemical And Solid State Letters, 2005. **8**(8): p. A414-A417.
49. Kim, D.K., et al., *Mechanistic study of the unusual catalytic properties of a new Ni-Ce mixed oxide for the CO₂ reforming of methane*. Journal Of Catalysis, 2007. **247**(1): p. 101-111.
50. Zhu, W., et al., *Ceria coated Ni as anodes for direct utilization of methane in low-temperature solid oxide fuel cells*. Journal Of Power Sources, 2006. **160**(2): p. 897-902.
51. Xu, S., X.B. Yan, and X.L. Wang, *Catalytic performances of NiO-CeO₂ for the reforming of methane with CO₂ and O₂*. Fuel, 2006. **85**(14-15): p. 2243-2247.
52. Zhang, B.C., et al., *Steam reforming of ethanol over Ni-Cu/CeO₂ catalyst*. Chinese Journal Of Catalysis, 2006. **27**(7): p. 567-572.

53. Yue, B.H., et al., *Influence of transition metals (Cr, Mn, Fe, Co and Ni) on the methane combustion over Pd/Ce-Zr/Al₂O₃ catalyst*. Applied Surface Science, 2006. **252**(16): p. 5820-5828.
54. He, H.P. and J.M. Hill, *Carbon deposition on Ni/YSZ composites exposed to humidified methane*. Applied Catalysis A-General, 2007. **317**(2): p. 284-292.
55. Sin, A., et al., *Performance and life-time behaviour of NiCu-CGO anodes for the direct electro-oxidation of methane in IT-SOFCs*. Journal Of Power Sources, 2007. **164**(1): p. 300-305.
56. Li, Y., et al., *Hydrogen production from methane decomposition over Ni/CeO₂ catalysts*. Catalysis Communications, 2006. **7**(6): p. 380-386.
57. Lu, C., et al., *A comparison of Cu-ceria-SDC and Au-ceria-SDC composites for SOFC anodes*. Journal Of The Electrochemical Society, 2003. **150**(10): p. A1357-A1359.
58. Gorte, R.J., H. Kim, and J.M. Vohs, *Novel SOFC anodes for the direct electrochemical oxidation of hydrocarbon*. Journal Of Power Sources, 2002. **106**(1-2): p. 10-15.
59. Gorte, R.J., et al., *Anodes for direct oxidation of dry hydrocarbons in a solid-oxide fuel cell*. Advanced Materials, 2000. **12**(19): p. 1465-1469.
60. Park, S., et al., *Direct oxidation of hydrocarbons in a solid oxide fuel cell I. Methane oxidation*. Journal Of The Electrochemical Society, 1999. **146**(10): p. 3603-3605.
61. Hornes, A., et al., *Catalytic properties of monometallic copper and bimetallic copper-nickel systems combined with ceria and Ce-X (X = Gd, Tb) mixed oxides applicable as SOFC anodes for direct oxidation of methane*. Journal Of Power Sources, 2007. **169**(1): p. 9-16.
62. Liu, J., et al., *A fuel-flexible ceramic-based anode for solid oxide fuel cells*. Electrochemical And Solid State Letters, 2002. **5**(6): p. A122-A124.
63. Liu, J.A. and S.A. Barnett, *Operation of anode-supported solid oxide fuel cells on methane and natural gas*. Solid State Ionics, 2003. **158**(1-2): p. 11-16.
64. Holtappels, P., et al., *Electrochemical characterization of ceramic SOFC anodes*. Journal Of The Electrochemical Society, 2001. **148**(8): p. A923-A929.
65. Pudmich, G., et al., *Chromite/titanate based perovskites for application as anodes in solid oxide fuel cells*. Solid State Ionics, 2000. **135**(1-4): p. 433-438.
66. Kobayashi, K., et al., *Electronic transport properties and electronic structure of TiO₂-doped YSZ*. Solid State Ionics, 2000. **135**(1-4): p. 643-651.
67. Minh, N.Q., *Ceramic Fuel-Cells*. Journal Of The American Ceramic Society, 1993. **76**(3): p. 563-588.
68. Larminie, J.a.D., A., *Fuel Cell Systems Explained*. 2001, New York: Wiley.
69. Stambouli, A.B. and E. Traversa, *Solid oxide fuel cells (SOFCs): a review of an environmentally clean and efficient source of energy*. Renewable & Sustainable Energy Reviews, 2002. **6**(5): p. 433-455.
70. Lu, Z.G., et al., *Effect of complex additives on sinterability and conductivity of YSZ electrolytes*. Rare Metal Materials And Engineering, 2005. **34**(12): p. 1961-1964.

71. Zhu, Q.S. and B. Fan, *Low temperature sintering of 8YSZ electrolyte film for intermediate temperature solid oxide fuel cells*. Solid State Ionics, 2005. **176**(9-10): p. 889-894.
72. Primdahl, S. and M. Mogensen, *Durability and thermal cycling of Ni/YSZ cermet anodes for solid oxide fuel cells*. Journal Of Applied Electrochemistry, 2000. **30**(2): p. 247-257.
73. Perednis, D., Honegger, K., and Gauckler, L. J., *Fourth European Solid Oxide Fuel Cell Forum*. 2000: A. Mc Evoy.
74. Craciun, R., et al., *A novel method for preparing anode cermets for solid oxide fuel cells*. Journal Of The Electrochemical Society, 1999. **146**(11): p. 4019-4022.
75. Lu, C., et al., *Development of solid oxide fuel cells for the direct oxidation of hydrocarbon fuels*. Solid State Ionics, 2002. **152**: p. 393-397.
76. Bard, A.J. and L.R. Faulkner, *Electrochemical Methods: Fundamentals and Applications*. 2nd ed. 2001: John Wiley.
77. Barsoukov, E.a.M., R. J., *Impedance Spectroscopy: Theory, Experiment, and Applications*. 2nd ed. 2005: John Wiley.
78. McIntosh, S., et al., *An examination of carbonaceous deposits in direct-utilization SOFC anodes*. Journal Of The Electrochemical Society, 2004. **151**(4): p. A604-A608.
79. Hauch, A., et al., *Performance and durability of solid oxide electrolysis cells*. Journal Of The Electrochemical Society, 2006. **153**(9): p. A1741-A1747.
80. Koch, S., et al., *Solid oxide fuel cell performance under severe operating conditions*. Fuel Cells, 2006. **6**(2): p. 130-136.
81. Mogensen, M., et al., *Composite electrodes in solid oxide fuel cells and similar solid state devices*. Journal Of Electroceramics, 2000. **5**(2): p. 141-152.
82. Sheng, C.Y. and A.M. Dean, *Importance of gas-phase kinetics within the anode channel of a solid-oxide fuel cell*. Journal Of Physical Chemistry A, 2004. **108**(17): p. 3772-3783.
83. Hibino, T., et al., *Ru-catalyzed anode materials for direct hydrocarbon SOFCs*. Electrochimica Acta, 2003. **48**(17): p. 2531-2537.
84. Hibino, T., et al., *High performance anodes for SOFCs operating in methane-air mixture at reduced temperatures*. Journal Of The Electrochemical Society, 2002. **149**(2): p. A133-A136.
85. Hashimoto, A., et al., *Intermediate-temperature SOFCs with ru-catalyzed Ni-cermet anodes*, in *Electroceramics In Japan Vii*. 2004. p. 151-154.
86. Murray, E.P., et al., *Direct solid oxide fuel cell operation using isooctane*. Electrochemical And Solid State Letters, 2006. **9**(6): p. A292-A294.
87. Zhan, Z.L. and S.A. Barnett, *An octane-fueled solid oxide fuel cell*. Science, 2005. **308**(5723): p. 844-847.
88. Zhan, Z.L. and S.A. Barnett, *Use of a catalyst layer for propane partial oxidation in solid oxide fuel cells*. Solid State Ionics, 2005. **176**(9-10): p. 871-879.

89. Tikekar, N.M., T.J. Armstrong, and A.V. Virkar, *Reduction and reoxidation kinetics of nickel-based SOFC anodes*. Journal Of The Electrochemical Society, 2006. **153**(4): p. A654-A663.
90. Zhao, F. and A.V. Virkar, *Dependence of polarization in anode-supported solid oxide fuel cells on various cell parameters*. Journal Of Power Sources, 2005. **141**(1): p. 79-95.
91. Fleig, J. and J. Maier, *The polarization of mixed conducting SOFC cathodes: Effects of surface reaction coefficient, ionic conductivity and geometry*. Journal Of The European Ceramic Society, 2004. **24**(6): p. 1343-1347.
92. Brichzin, V., et al., *The geometry dependence of the polarization resistance of Sr-doped LaMnO₃ microelectrodes on yttria-stabilized zirconia*. Solid State Ionics, 2002. **152**: p. 499-507.
93. Fleig, J., *On the width of the electrochemically active region in mixed conducting solid oxide fuel cell cathodes*. Journal Of Power Sources, 2002. **105**(2): p. 228-238.
94. Brichzin, V., et al., *Geometry dependence of cathode polarization in solid oxide fuel cells investigated by defined Sr-doped LaMnO₃ microelectrodes*. Electrochemical And Solid State Letters, 2000. **3**(9): p. 403-406.
95. Jiang, S.P., J.G. Love, and L. Apateanu, *Effect of contact between electrode and current collector on the performance of solid oxide fuel cells*. Solid State Ionics, 2003. **160**(1-2): p. 15-26.
96. Li, P.W., S.P. Chen, and M.K. Chyu, *To achieve the best performance through optimization of gas delivery and current collection in solid oxide fuel cells*. Journal Of Fuel Cell Science And Technology, 2006. **3**(2): p. 188-194.
97. Koch, S., et al., *Electrode activation and passivation of solid oxide fuel cell electrodes*. Fuel Cells, 2006. **6**(2): p. 117-122.
98. Chervin, C., R.S. Glass, and S.M. Kauzlarich, *Chemical degradation of La_{1-x}SrMnO₃/Y₂O₃-stabilized ZrO₂ composite cathodes in the presence of current collector pastes*. Solid State Ionics, 2005. **176**(1-2): p. 17-23.
99. Jiang, S.R., *Resistance measurement in solid oxide fuel cells*. Journal Of The Electrochemical Society, 2001. **148**(8): p. A887-A897.
100. Guillodo, M., P. Vernoux, and J. Fouletier, *Electrochemical properties of Ni-YSZ cermet in solid oxide fuel cells - Effect of current collecting*. Solid State Ionics, 2000. **127**(1-2): p. 99-107.
101. Wanzenberg, E., et al., *Influence of electrode contacts on conductivity measurements of thin YSZ electrolyte films and the impact on solid oxide fuel cells*. Solid State Ionics, 2003. **164**(3-4): p. 121-129.
102. Kek, D. and N. Bonanos, *Electrochemical H-D isotope effect at metal-perovskite proton conductor interfaces*. Solid State Ionics, 1999. **125**(1-4): p. 345-353.
103. Kek, D., M. Mogensen, and S. Pejovnik, *A study of metal (Ni, Pt, Au)/yttria-stabilized zirconia interface in hydrogen atmosphere at elevated temperature*. Journal Of The Electrochemical Society, 2001. **148**(8): p. A878-A886.
104. Bessler, W.G., J. Warnatz, and D.G. Goodwin, *The influence of equilibrium potential on the hydrogen oxidation kinetics of SOFC anodes*. Solid State Ionics, 2007. **177**(39-40): p. 3371-3383.

105. Zhu, H.Y. and R.J. Kee, *Modeling electrochemical impedance spectra in SOFC button cells with internal methane reforming*. Journal Of The Electrochemical Society, 2006. **153**(9): p. A1765-A1772.
106. Will, J., et al., *Fabrication of thin electrolytes for second-generation solid oxide fuel cells*. Solid State Ionics, 2000. **131**(1-2): p. 79-96.
107. Yamamoto, O., et al., *Perovskite-Type Oxides As Oxygen Electrodes For High-Temperature Oxide Fuel-Cells*. Solid State Ionics, 1987. **22**(2-3): p. 241-246.
108. Primdahl, S. and M. Mogensen, *Oxidation of hydrogen on Ni/yttria-stabilized zirconia cermet anodes*. Journal Of The Electrochemical Society, 1997. **144**(10): p. 3409-3419.
109. Finnerty, C.M. and R.M. Ormerod, *Internal reforming over nickel/zirconia anodes in SOFCs operating on methane: influence of anode formulation, pre-treatment and operating conditions*. Journal Of Power Sources, 2000. **86**(1-2): p. 390-394.
110. Bieberle, A., L.P. Meier, and L.J. Gauckler, *The electrochemistry of Ni pattern anodes used as solid oxide fuel cell model electrodes*. Journal Of The Electrochemical Society, 2001. **148**(6): p. A646-A656.
111. Brown, M., S. Primdahl, and M. Mogensen, *Structure/performance relations for Ni/yttria-stabilized zirconia anodes for solid oxide fuel cells*. Journal Of The Electrochemical Society, 2000. **147**(2): p. 475-485.
112. Jiang, Y. and A.V. Virkar, *A high performance, anode-supported solid oxide fuel cell operating on direct alcohol*. Journal Of The Electrochemical Society, 2001. **148**(7): p. A706-A709.
113. Gorte, R.J. and J.M. Vohs, *Novel SOFC anodes for the direct electrochemical oxidation of hydrocarbons*. Journal Of Catalysis, 2003. **216**(1-2): p. 477-486.
114. Zha, S.W., et al., *GDC-based low-temperature SOFCs powered by hydrocarbon fuels*. Journal Of The Electrochemical Society, 2004. **151**(8): p. A1128-A1133.
115. Kim, T., et al., *A study of carbon formation and prevention in hydrocarbon-fueled SOFC*. Journal Of Power Sources, 2006. **155**(2): p. 231-238.
116. Mogensen, M., et al., *Progress in understanding SOFC electrodes*. Solid State Ionics, 2002. **150**(1-2): p. 123-129.
117. Mogensen, M. and K. Kammer, *Conversion of hydrocarbons in solid oxide fuel cells*. Annual Review of Materials Research, 2003. **33**: p. 321-331.
118. Bera, P. and M.S. Hegde, *Characterization and catalytic properties of combustion synthesized Au/CeO₂ catalyst*. Catalysis Letters, 2002. **79**(1-4): p. 75-81.
119. Laosiripojana, N. and S. Assabumrungrat, *Catalytic dry reforming of methane over high surface area ceria*. Applied Catalysis B-Environmental, 2005. **60**(1-2): p. 107-116.
120. Metcalfe, I.S., et al., *Hydrocarbon Activation In Solid-State Electrochemical-Cells*. Solid State Ionics, 1992. **57**(3-4): p. 259-264.
121. Yokokawa, H., et al., *Protons in ceria and their roles in SOFC electrode reactions from thermodynamic and SIMS analyses*. Solid State Ionics, 2004. **174**(1-4): p. 205-221.

122. Toebe, M.L., et al., *Impact of the structure and reactivity of nickel particles on the catalytic growth of carbon nanofibers*. Catalysis Today, 2002. **76**(1): p. 33-42.
123. Dai, H.J., *Carbon nanotubes: opportunities and challenges*. Surface Science, 2002. **500**(1-3): p. 218-241.
124. Pomfret, M.B., J.C. Owrutsky, and R.A. Walker, *In situ studies of fuel oxidation in solid oxide fuel cells*. Analytical Chemistry, 2007. **79**(6): p. 2367-2372.
125. Basu, R.N., et al., *Pyrolytic carbon deposition on porous cathode tubes and its use as an interlayer for solid oxide fuel cell zirconia electrolyte fabrication*. Journal Of The Electrochemical Society, 2001. **148**(5): p. A506-A512.
126. Rodriguez-Mirasol, J., et al., *Structural and textural properties of pyrolytic carbon formed within a microporous zeolite template*. Chemistry Of Materials, 1998. **10**(2): p. 550-558.
127. Franklin, R.E., *Crystallite Growth In Graphitizing And Non-Graphitizing Carbons*. Proceedings Of The Royal Society Of London Series A-Mathematical And Physical Sciences, 1951. **209**(1097): p. 196-&.
128. Dresselhaus, M.S., et al., *New Characterization Techniques For Activated Carbon-Fibers*. Carbon, 1992. **30**(7): p. 1065-1073.
129. Ergun, S., *Determination Of Layer Sizes In Carbons*. Carbon, 1968. **6**(1): p. 7-&.
130. Ergun, S. and T.J. Gifford, *Analysis Of 00l Reflections Of Carbons*. Journal Of Applied Crystallography, 1968. **1**: p. 313-&.
131. Tsai, H.C. and D.B. Bogy, *Characterization Of Diamond-Like Carbon-Films And Their Application As Overcoats On Thin-Film Media For Magnetic Recording*. Journal Of Vacuum Science & Technology A-Vacuum Surfaces And Films, 1987. **5**(6): p. 3287-3312.
132. Xie, Y.M. and P.M.A. Sherwood, *X-Ray Photoelectron Spectroscopic Studies Of Carbon-Fiber Surfaces. II. Differences In The Surface-Chemistry And Bulk Structure Of Different Carbon-Fibers Based On Poly(Acrylonitrile) And Pitch And Comparison With Various Graphite Samples*. Chemistry Of Materials, 1990. **2**(3): p. 293-299.
133. Yasuda, E.-i., et al., *Carbon alloys: novel concepts to develop carbon science and technology*. 2003. 569 pp.
134. Dresselhaus, M.S., *Future directions in carbon science*. Annual Review Of Materials Science, 1997. **27**: p. 1-34.
135. Ferrari, A.C. and J. Robertson, *Interpretation of Raman spectra of disordered and amorphous carbon*. Physical Review B, 2000. **61**(20): p. 14095-14107.
136. Gogotsi, Y., et al., *Graphite polyhedral crystals*. Science, 2000. **290**(5490): p. 317-320.
137. Matthews, M.J., et al., *Origin of dispersive effects of the Raman D band in carbon materials*. Physical Review B, 1999. **59**(10): p. R6585-R6588.
138. Vasilets, V.N., et al., *Characterization of doped diamond-like carbon films deposited by hot wire plasma sputtering of graphite*. Applied Physics A-Materials Science & Processing, 2004. **79**(8): p. 2079-2084.

139. Wagner, J., et al., *Resonant Raman-Scattering Of Amorphous-Carbon And Polycrystalline Diamond Films*. Physical Review B, 1989. **40**(3): p. 1817-1824.
140. Tuinstra, F. and J.L. Koenig, *Characterization Of Graphite Fiber Surfaces With Raman Spectroscopy*. Journal Of Composite Materials, 1970. **4**: p. 492-&.
141. Tuinstra, F. and J.L. Koenig, *Raman Spectrum Of Graphite*. Journal Of Chemical Physics, 1970. **53**(3): p. 1126-&.
142. Knight, D.S. and W.B. White, *Characterization Of Diamond Films By Raman-Spectroscopy*. Journal Of Materials Research, 1989. **4**(2): p. 385-393.
143. Cancado, L.G., et al., *General equation for the determination of the crystallite size L-a of nanographite by Raman spectroscopy*. Applied Physics Letters, 2006. **88**(16).
144. Desimoni, E., G.I. Casella, and A.M. Salvi, *Xps Xaes Study Of Carbon-Fibers During Thermal Annealing Under Uhv Conditions*. Carbon, 1992. **30**(4): p. 521-526.
145. Patsalas, P., et al., *A complementary study of bonding and electronic structure of amorphous carbon films by electron spectroscopy and optical techniques*. Diamond And Related Materials, 2001. **10**(3-7): p. 960-964.
146. Sherwood, P.M.A., *Surface analysis of carbon and carbon fibers for composites*. Journal Of Electron Spectroscopy And Related Phenomena, 1996. **81**(3): p. 319-342.
147. Blyth, R.I.R., et al., *XPS studies of graphite electrode materials for lithium ion batteries*. Applied Surface Science, 2000. **167**(1-2): p. 99-106.
148. Rodriguez, N.M., et al., *XPS, EM, and catalytic studies of the accumulation of carbon on Pt black*. Journal Of Catalysis, 2001. **197**(2): p. 365-377.
149. Speranza, G. and N. Laidani, *Measurement of the relative abundance of sp(2) and sp(3) hybridised atoms in carbon based materials by XPS: a critical approach. Part I*. Diamond And Related Materials, 2004. **13**(3): p. 445-450.
150. Speranza, G. and N. Laidani, *Measurement of the relative abundance of sp(2) and sp(3) hybridised atoms in carbon based materials by XPS: a critical approach. Part II*. Diamond And Related Materials, 2004. **13**(3): p. 451-458.
151. Briggs, D. and Editor, *Handbook of X-Ray and Ultraviolet Photoelectron Spectroscopy*. 1977. 399 pp.
152. Moulder, J.F., Stickle, W. F., Sobol, P. E., and Bomben, K. D., *Handbook of X-Ray Photoelectron Spectroscopy*. 1995, Eden Prairie, MN: Physical Electronics.
153. Bond, G.C. and D.T. Thompson, *Catalysis by gold*. Catalysis Reviews-Science And Engineering, 1999. **41**(3-4): p. 319-388.
154. Baker, R., J. Guindet, and M. Kleitz, *Classification criteria for solid oxide fuel cell electrode materials*. Journal Of The Electrochemical Society, 1997. **144**(7): p. 2427-2432.
155. Hirabayashi, D., et al., *Solid oxide fuel cells operating without using an anode material*. Solid State Ionics, 2004. **168**(1-2): p. 23-29.

156. Pomfret, M.B., et al., *Structural and compositional characterization of yttria-stabilized zirconia: Evidence of surface-stabilized, low-valence metal species*. Analytical Chemistry, 2005. **77**(6): p. 1791-1795.
157. Goodenough, J.B., *Electronic and ionic transport properties and other physical aspects of perovskites*. Reports On Progress In Physics, 2004. **67**(11): p. 1915-1993.
158. Williford, R.E., et al., *Diffusion limitations in the porous anodes of SOFCs*. Journal Of The Electrochemical Society, 2003. **150**(8): p. A1067-A1072.
159. Recknagle, K.P., et al., *Three-dimensional thermo-fluid electrochemical modeling of planar SOFC stacks*. Journal Of Power Sources, 2003. **113**(1): p. 109-114.
160. Gellings, P.J. and H.J.M. Bouwmeester, *Solid state aspects of oxidation catalysis*. Catalysis Today, 2000. **58**(1): p. 1-53.
161. Mitterdorfer, A. and L.J. Gauckler, *Reaction kinetics of the Pt, O-2(g)/vertical bar c-ZrO₂ system: precursor-mediated adsorption*. Solid State Ionics, 1999. **120**(1-4): p. 211-225.
162. Bieberle, A. and L.J. Gauckler, *State-space modeling of the anodic SOFC system Ni, H-2-H₂O vertical bar YSZ*. Solid State Ionics, 2002. **146**(1-2): p. 23-41.
163. Bieberle, A. and L.J. Gauckler, *Reaction mechanism of Ni pattern anodes for solid oxide fuel cells*. Solid State Ionics, 2000. **135**(1-4): p. 337-345.
164. Maestas, S. and T.B. Flanagan, *Diffusion Of Hydrogen In Gold-Palladium Alloys*. Journal Of Physical Chemistry, 1973. **77**(6): p. 850-854.
165. Pyun, S.I., W.J. Lee, and T.H. Yang, *Hydrogen diffusion through palladium-gold alloy coatings electrodeposited on palladium substrate under permeable boundary condition*. Thin Solid Films, 1997. **311**(1-2): p. 183-189.
166. Jiang, S.P. and Y. Ramprakash, *H-2 oxidation on Ni/Y-TZP cermet electrodes - a comparison of electrode behaviour by GCI and EIS techniques*. Solid State Ionics, 1999. **122**(1-4): p. 211-222.
167. Mizusaki, J., et al., *Preparation Of Nickel Pattern Electrodes On Ysz And Their Electrochemical Properties In H₂-H₂O Atmospheres*. Journal Of The Electrochemical Society, 1994. **141**(8): p. 2129-2134.
168. Jiang, S.P. and S.P.S. Badwal, *An electrode kinetics study of H-2 oxidation on Ni/Y₂O₃-ZrO₂ cermet electrode of the solid oxide fuel cell*. Solid State Ionics, 1999. **123**(1-4): p. 209-224.
169. Jiang, S.P. and Y. Ramprakash, *H-2 oxidation on Ni/Y-TZP cermet electrodes - polarisation behaviour*. Solid State Ionics, 1999. **116**(1-2): p. 145-156.
170. Jiang, S.P. and S.P.S. Badwal, *Hydrogen oxidation at the nickel and platinum electrodes on yttria-tetragonal zirconia electrolyte*. Journal Of The Electrochemical Society, 1997. **144**(11): p. 3777-3784.
171. Horita, T., et al., *Imaging of labeled gas movements at the SOFC electrode/electrolyte interfaces*. Solid State Ionics, 2004. **169**(1-4): p. 105-113.
172. Zhu, H.Y., et al., *Modeling elementary heterogeneous chemistry and electrochemistry in solid-oxide fuel cells*. Journal Of The Electrochemical Society, 2005. **152**(12): p. A2427-A2440.

173. Norby, T. and P. Kofstad, *High Temperature Electrochemistry: Ceramics and Metals*. 17th Risø International Symposium on Materials Science, ed. F.W. Poulsen, et al. 1996, Roskilde.
174. Williford, R.E. and L.A. Chick, *Surface diffusion and concentration polarization on oxide-supported metal electrocatalyst particles*. Surface Science, 2003. **547**(3): p. 421-437.
175. Sukesini, A.M., et al., *Electrochemical oxidation of H_2 , CO, and CO/ H_2 mixtures on patterned Ni anodes on YSZ electrolytes*. Journal Of The Electrochemical Society, 2006. **153**(4): p. A705-A715.
176. Primdahl, S., *Nickel/Yttria-Stabilised Zirconia cermet anodes for SOFC anodes*. Ph.D thesis, University of Twente, 1999.
177. Matsumoto, H., et al., *Electromotive Force of Hydrogen Isotope Cell with a High Temperature Proton-Conducting Solid Electrolyte $CaZr_{0.90}In_{0.10}O_{3-\alpha}$* . Journal Of The Electrochemical Society, 2006. **153**(4): p. A705-A715.

